Pergamon

0301-9322(94)E0013-9

Int. J. Multiphase Flow Vol. 20, Suppl., pp. 91–168, 1994

0301-9322/94 $26.00 + 0.00

TWO-PHASE CRITICAL FLOW

E. ELIAS[1] and G. S. LELLOUCHE[2]

[1]Faculty of Mechanical Engineering, Technion—Israel Institute of Technology, Haifa 32000, Israel

[2]S. Levy Inc., 3425 S. Bascom Ave, Campbell, CA 95008, U.S.A.

(Received 14 February 1994)

Abstract—Understanding the heat and mass transfer phenomena occurring during critical flow of two-phase mixtures is of primary importance in the safety analyses of pressurized water, boiling water and liquid-metal-cooled nuclear reactors. It has been shown that during a blowdown incident, the critical flow rate of the two-phase mixture may be affected by a variety of parameters such as the fluid stagnation conditions, the configuration of the blowdown vessel, the length and diameter of the exhaust duct, the purity of the liquid and the local and frictional pressure losses in the flow channel. The complexity of the thermodynamic phenomena taking place during the blowdown process resulted in many studies which compare a particular theory with selected sets of experimental data. However, in the absence of an adequate theory which is applicable over the entire range of the parameters encountered in the nuclear industry, there is a tendency to rely on semi-empirical correlation of the existing data.

The main objective of this paper is to provide a general review of two-phase critical flow from the viewpoint of the needs of thermal-hydraulic systems codes and to conduct a systematic evaluation of the existing data and theoretical models in order to quantify the validity, under various conditions, of several of the more widely used critical flow models. Ten different critical flow models have been formulated and tested in this study against an extensive set of data from critical flow experiments with water as the test fluid. Results of the present study are expected to enhance the understanding of the predictive capabilities and limitations of the critical flow models currently used in the power industry.

Key Words: two-phase flow, critical flow, sound velocity, shock wave, choked flow

1. INTRODUCTION

The two-phase critical flow of one-component mixtures has been the subject of many analytical and experimental investigations, mainly because of its importance in the safety analyses of pressurized water, boiling water and liquid-metal-cooled nuclear reactors. The phenomenon is also pertinent to fossil-fuel fired power plants, steam–water boilers and railway transportation of saturated and subcooled liquids.

Critical flow of singe-phase compressible fluids has been extensively studied and may be considered as well understood. However, a complete theory describing the critical flow of two-phase steam–water mixtures is not available. The main aspects of the problem are discussed in several review articles (Bouré 1977; Jones & Saha 1977; Ardron & Furness 1976; Wallis 1980; Isbin 1980; Giot 1981). A comprehensive review and discussion of the analytical models and key experimental results has been compiled by D'Auria & Vigni (1980) and by Abdollahian *et al.* (1980, 1982), with about 250 references cited. It is shown that the critical flow rate of a two-phase mixture flowing out of a pressurized vessel is affected by a variety of parameters such as the fluid stagnation conditions, the configuration of the blowdown vessel, the length and diameter of the exhaust duct, the purity of the liquid and the local and frictional pressure losses in the flow channel. The complexity of the thermodynamic phenomena taking place during the blowdown process resulted in many studies which show comparisons between a particular theory and selected sets of experimental data. Moreover, it became quite easy to select a comparison plot to justify the choice of a particular theory (Wallis 1980). The main objective of this paper is to conduct a systematic evaluation of a wide range of data and theoretical models in order to quantify the validity, under various conditions, of several of the more widely used critical flow models. As such, this paper should not be viewed as providing an in-depth analysis of the physics and mathematics of critical flow; its purpose is to provide a view of model validity for a very broad range of data.

Ten different critical flow models have been formulated, programmed and tested in this study against an extensive set of data from critical flow experiments with water as the test fluid. Results

of the present study are expected to enhance the understanding of the predictive capabilities and limitations of the critical flow models used in the power industry.

2. THEORETICAL FOUNDATIONS

In order to develop the basis for understanding critical flow, it is useful to first consider the flow of a single-phase vapor in a pipe of constant cross section. This approach is required because the usual verbal constructs used to explain critical flow can be somewhat misleading. Thus, the concept that critical flow is that flow which no longer depends on small changes in downstream conditions is correct for single-phase as well as for two-phase flow. However, while in single-phase flow the critical velocity equals the local isentropic sound velocity, the critical velocity in two-phase flow is far more complicated to predict, since the rapid expansion of the fluid may induce mechanical and thermal non-equilibrium between the two phases.

This and the following section contain a simple discussion of some important features of single-phase and two-phase critical flow. Further discussion of the subject of single-phase critical flow may be found in many classical texts on gas dynamics (e.g. Lee & Sears 1964; Shapiro 1953; Oswatitsch 1956) where fairly detailed analysis of critical flow of gases is included (usually under the titles of sonic velocity and in the sections on flow in converging–diverging nozzles or supersonic diffusers).

Consider the steady one-dimensional flow of a single-phase vapor, which for simplicity (but not necessarily accurately) is assumed to be at a constant temperature. In such a situation, only the momentum equation is of importance and can be written at steady state using a convenient notation:

$$\frac{\mathrm{d}(\rho V^2)}{\mathrm{d}z} + \frac{\mathrm{d}p}{\mathrm{d}z} + \rho g + f\frac{\rho V^2}{2D} = 0 \qquad [1]$$

where ρ is density, V velocity, p pressure, z and D are the axial coordinate along the flow channel and the channel diameter respectively, g is acceleration due to gravity and f is the D'Arcy friction factor.

In steady state, the mass flux, $\rho V = G_\mathrm{o}$, is spatially constant and [1] may be rewritten as:

$$G_\mathrm{o}^2\frac{\mathrm{d}v}{\mathrm{d}z} + \frac{\mathrm{d}p}{\mathrm{d}z} + \rho g + f\frac{G_\mathrm{o}^2}{2\rho D} = 0 \qquad [2]$$

where v is specific volume.

If the temperature is constant, $\rho = \rho(p)$ only, and if this function and f are specified along with the inlet conditions, then [2] may be solved for $\rho(z)$ and $p(z)$. It is not, however, necessary to do this in order to predict the conditions for critical flow. Instead, [2] can be reduced to the following:

$$\frac{\mathrm{d}p}{\mathrm{d}z} = -\frac{\rho g + fG_\mathrm{o}^2/2\rho D}{1 - \dfrac{G_\mathrm{o}^2}{\rho^2}\dfrac{\mathrm{d}\rho}{\mathrm{d}p}} \qquad [3]$$

And, as shall be seen later, this generalized form is the fundamental equation of importance for critical flow. The important thing is to understand what happens to the pressure as flow moves along the pipe:

(1) because of friction and head loss (in upwards flow) the pressure drops;†
(2) as the pressure decreases, the density decreases ($\mathrm{d}\rho/\mathrm{d}p > 0$);
(3) because G_o is constant, V increases.

At some critical location $\mathrm{d}p/\mathrm{d}z \to -\infty$ when:

$$\frac{G_\mathrm{o}^2}{\rho^2(z)}\frac{\mathrm{d}\rho}{\mathrm{d}p} = 1 \qquad [4]$$

†The pressure will always increase for adiabatic down flow in a constant area unless $fG^2/\rho > \rho g$ at $z = 0$.

In a system with specified stagnation and sink pressures the mass flux is a consequence of the flow process and will adjust so that the critical value occurs at the exit of the pipe† (after which no further frictional pressure drop can take place). Thus, the maximum flow rate that can be forced through a pipe of length L is limited by [4] being satisfied at $z = L$. One can always achieve this flow rate by using a larger pump, independently of the pressure beyond L.

Although a "straw model" was established (single-phase vapor, constant temperature), the resulting equation is essentially correct for the two-phase mixture momentum equation which can be stated as:

$$\frac{dp}{dz}\left[1+\frac{\partial \overline{GV}}{\partial p}\right] = -(F+\bar{\rho}g) - \frac{\partial \overline{GV}}{\partial T}\frac{dT}{dz} \qquad [5]$$

where $\overline{GV} \equiv G_G V_G + G_L V_L$, F is the wall friction and $\bar{\rho} = \rho_L(1-\epsilon) + \rho_G \epsilon$ is the mixture density. In the expansion of $d\overline{GV}/dz$ in [5], it is assumed that $\overline{GV}$ is a function of both temperature and pressure.‡ The continuity equation implies that, in steady state, the mass flux is constant. Hence,

$$\frac{d\overline{GV}}{dz} = G_o^2 \frac{d(1/\rho')}{dz} \qquad [6]$$

where the correct definition for the momentum density, ρ', as a function of the flow quality, x, is

$$1/\rho' \equiv \frac{x^2}{\epsilon \rho_G} + \frac{(1-x)^2}{(1-\epsilon)\rho_L} \qquad [7]$$

Thus the condition for critical flow or maximum flow of the mixture is:

$$\frac{\partial \overline{GV}}{\partial \rho} = -1 \qquad [8]$$

2.1. Sonic Velocity

The sonic velocity, a, is the velocity at which information (pressure disturbances) travels in a fluid.§ If an object in the fluid or a portion of the fluid attempts to travel more rapidly than this velocity, a shock wave will be established. In a single-phase fluid, this critical velocity is defined by [4] which can be written as:

$$V^2(L) = \frac{dp}{d\rho} = a^2 \qquad [9]$$

In single-phase flow, the momentum equation, which transmits information at both the fluid velocity (mass motion) and the sonic velocity can, therefore, not "see" ahead when the local flow velocity reaches a because information concerning the upstream geometry and conditions can itself only travel at the same velocity. At that velocity the flow is said to be choked.

In equilibrium, two-phase flow the choking condition stated in [8] can be restated as:

$$\overline{V}^2 = \frac{dp}{d\rho'} \qquad [10]$$

The term $(dp/d\rho')$ has the same significance as the square of the sound-speed in [9], but it is not at all clear that it is the same sort of velocity. To demonstrate the difference between the two cases, consider, for example, flow of a two-phase mixture in a horizontal deep duct. If the duct is long, the flow will, in all likelihood, separate even at high velocities. In this situation there is an all-vapor region which is above a mixed phase region which is, in turn, above an all-liquid region. In each single-phase region, information can propagate at the single-phase sonic velocity but each is different from the other. It may be that for horizontal flows, the basic equations (assuming a one-dimensional continuous phase) are not valid and that two sets of equations must be established (one for the gas and one for the liquid phase) in order to analyze such a situation fully.

†That is, the behavior of the fluid will not permit G_o to exceed some maximum value which depends on the geometry.
‡If it depends on both T_G and T_L then the temperature term is really a sum of two terms. If vaporization is accounted for, a quality term will appear on the right-hand side of the equation as well.
§An object can travel faster than that but the fluid itself cannot transmit information within itself faster than this velocity.

A generalized criterion for choked two-phase flow can be obtained, in analogy with single-phase flow, by applying the theory of characteristics to a one-dimensional transient two-phase model. Thus, if the model is presented as a system of quasi-linear first-order partial differential equations of the form:

$$A(\mathbf{U})\frac{\partial \mathbf{U}}{\partial t} + B(\mathbf{U})\frac{\partial \mathbf{U}}{\partial z} + C(\mathbf{U}) = 0 \qquad [11]$$

where $\mathbf{U}$ is a vector of the primary dependent variables, then the velocity of signal propagation along the corresponding characteristic path in the space–time plane are defined as the real part of the roots, λ_i ($i \leqslant n$, the number of differential equations comprising the model), of the characteristic equation

$$\det(A\lambda - B) = 0 \qquad [12]$$

In a hyperbolic system of equation (obtained when the two-phase problem is "well-posed") all the roots of [12] are real. Choking will occur when the acoustic signal which propagates with the largest velocity relative to the fluid, is just stationary. In this condition no information can propagate into the solution region from the exterior. Thus, the choking criteria may be stated as:

$$\lambda_i \geqslant 0 \quad \text{for all} \quad i \leqslant n \qquad [13]$$

If the constitutive relations for mass and momentum transfer at the interface are known, [12] and [13] can be readily solved to determine the propagation velocity in the two-phase mixture. Analytical expressions for the two-phase speed of sound were derived by Trapp & Ransom (1982) using a six-equation two-fluid model and by Kroeger (1978) and Kaizerman *et al.* (1983) using a four-equation drift flux model. In all cases, the predicted mixture sound-speed depends on the assumptions used to derive the constitutive relations and the flow pattern.

To summarize the subject of two-phase critical flow it is of interest to quote the NEA state-of-the-art report (Brittain *et al.* 1982) where the following (still valid) paragraphs are found:

> "In adiabatic, frictionless, single-phase, compressible, steady flow through a De Laval nozzle the critical conditions arising in the minimum cross-section are well-understood and can be described analytically. Three equivalent statements are generally adopted to define criticality from a physical point of view: (a) upstream of the critical section the fluid state does not depend upon "small" changes of the thermodynamic variables existing downstream; (b) at the minimum critical cross-section there is at least one wave whose propagation velocity is zero with respect to the duct wall; and (c) (in the critical section) the flow velocity is equal to the local isentropic speed of sound.
>
> Only the first of the above definitions directly characterizes two-phase critical flow; the other two definitions require precautions when applied to two-phase flow. In fact, sonic speed is related to one phase and it is generally quite different in liquid and vapor; moreover, any perturbation wave induces variations in flow structure which may affect critical conditions. Neither of the last two points has been completely investigated."

In the sections that follow, a fairly detailed set of analyses of various well-known critical flow models will be provided. In the analyses of nuclear reactor transients, these models are used *in addition* to the system model (whether three, four, five or six equations). Yet, as has been seen in [5], critical flow is a direct consequence of the use of the momentum equation. There is a general inconsistency in most system codes: either the *ad hoc* model predicts critical flow too quickly or too late compared to what is implied by the remainder of the model.

3. NUMERICAL CONSIDERATIONS

The location of the critical plane in a choked flow is characterized by a so-called "pressure-knee" which describes the relatively sudden rapid negative increase in the pressure spatial derivative (cf. figure 1). This increase indicates that the critical flow location is near and is often used to assist

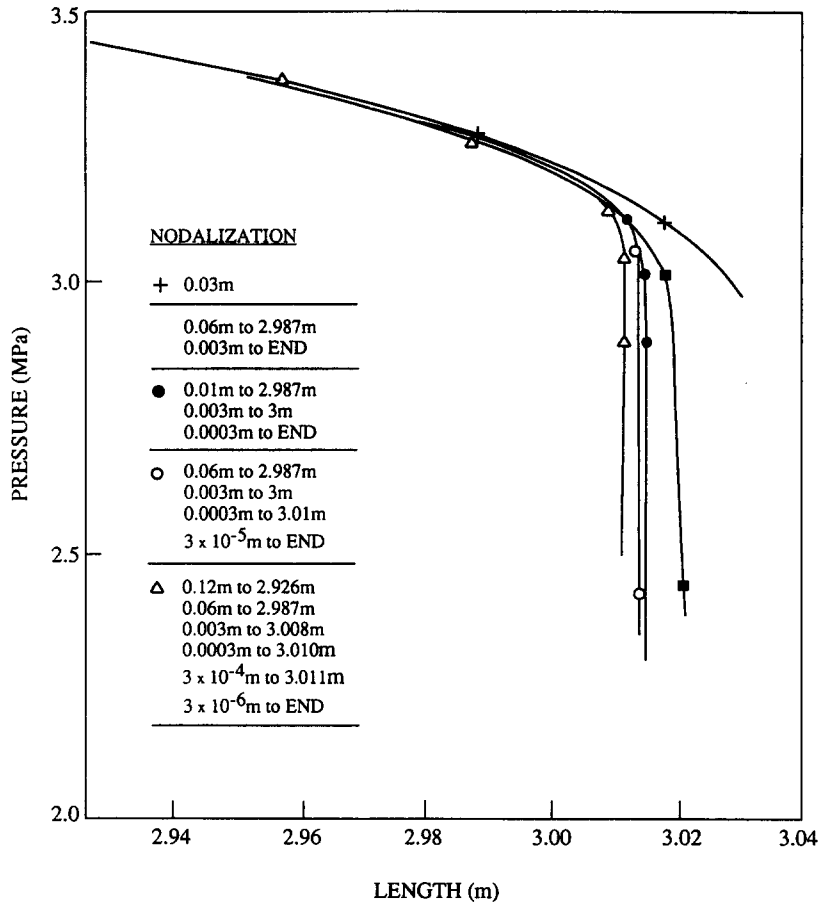

Figure 1. Effect of nodalization on the pressure spatial derivative near the choking plane.

in locating the critical pressure. Mathematically the critical pressure is more correctly located where $dp/dz \to -\infty$. In fact, for flow in a constant area duct, the one-dimensional continuous phase equations cannot be continued across a critical flow location. The spatial derivatives have a significant impact on numerical solutions because they change markedly in the neighborhood of critical flow. In this section, some of the difficulties in resolving the pressure spatial distribution and locating the onset of critical flow will be analyzed. The mathematical aspects of the critical flow condition are further discussed by Bouré *et al.* (1975).

When one is dealing with a steady one-dimensional flow of an ideal gas in a converging–diverging nozzle, the following equations can be established (assuming reversible adiabatic process) for the changes in Mach number, M, and pressure with changing area, in terms of the initial value of the Mach number (Lee & Sears 1964):

$$\frac{dM}{M} = -\frac{2+(\gamma-1)M^2}{2(1-M^2)}\frac{dA}{A} \qquad [14a]$$

$$\frac{dp}{p} = \frac{\gamma M^2}{1-M^2}\frac{dA}{A} \qquad [14b]$$

where γ is the ratio of specific heats and A is the flow area.

Because the Mach number reaches unity at the throat, the term $dA/(1-M^2)$ appears indeterminant but, in fact, is finite; otherwise there would be a jump in the variables M and p across the minimum area if M reaches unity at the throat and this event does not happen. Simple analytical

solutions are possible to demonstrate the flow behavior in the nozzle. Assuming that the specific heat ratio γ is constant, [14a] and [14b] may be integrated from point 1 to 2 to yield:

$$\frac{A_1}{A_2} = \frac{M_2}{M_1}\left[\frac{2+(\gamma-1)M_1^2}{2+(\gamma-1)M_2^2}\right]^{(\gamma+1)/(2(\gamma-1))} \quad [15a]$$

$$\frac{p_1}{p_2} = \left[\frac{2+(\gamma-1)M_2^2}{2+(\gamma-1)M_1^2}\right]^{\gamma/(\gamma-1)} \quad [15b]$$

Thus,† in a converging nozzle, while M is a continuous function of A, dM/dA diverges as $M \to 1$ and [14a] cannot be used beyond $M = 1$ (the solution does continue in the complex plane). In the diverging section, however, the solution can be continued for values $M > 1$. Since $A(z)$ is double-valued, [15a] has two solutions for $A = \text{const}$. However, it is observed that unless the sink pressure (the "back" pressure) is set at or below a specific value (the design pressure of the nozzle) the increase in M will limit itself with the formation of a shock wave followed by an increase in pressure and decrease of M to values less than unity.

When a fluid flows through a long duct, frictional effects at the wall and within the fluid become an important factor. In a pipe of constant cross section (adiabatic gas flow with friction), the fundamental equations of steady one-dimensional flow are:

$$\frac{dM}{M} = \frac{\gamma M^2[2+(\gamma-1)M^2]}{4(1-M^2)}\frac{f}{D}\,dz \quad [16a]$$

$$\frac{dp}{p} = -\frac{\gamma M^2[1+(\gamma-1)M^2]}{2(1-M^2)}\frac{f}{D}\,dz \quad [16b]$$

For an ideal gas with constant γ it is convenient to integrate [16a] and [16b] between the limits $M = M$ and $M = 1$, the corresponding limits on z being $z = 0$ and $z = L^*$. Thus:

$$\frac{\bar{f}L^*}{D} = \frac{1-M^2}{\gamma M^2} + \frac{\gamma+1}{2\gamma}\ln\left[\frac{(\gamma+1)M^2}{2+(\gamma-1)M^2}\right] \quad [17a]$$

$$\frac{p}{p^*} = \frac{1}{M}\left[\frac{2+(\gamma-1)M^2}{\gamma+1}\right]^{(\gamma+1)/(2(\gamma-1))} \quad [17b]$$

These results cannot be continued beyond $M = 1$ by going to a larger length. Furthermore, although there are two solutions for [17a] with $L^* = \text{const.}$, if the flow reaches $M = 1$ at $z = L^*$ (the end of the section) all spatial derivates of M and p diverge at L^*.

Two results of importance are found in both isentropic flow in a converging–diverging nozzle and in frictional flow in a constant area duct:

- the spatial derivatives of all variables have singularities at $M = 1$;
- the variables are finite and non-zero at $M = 1$.

Finally we consider the case of a steady flow in converging–diverging nozzle with friction. We again assume adiabatic one-dimensional flow for an ideal gas with an energy equation given by:

$$H + \tfrac{1}{2}V^2 = H_0 \quad [18]$$

†If $\gamma = 1$ the solution becomes:

$$\frac{A_1}{A_2} = \frac{M_2}{M_1}e^{-(M_2^2 - M_1^2)/2}$$

$$\frac{p_1}{p_2} = e^{(M_2^2 - M_1^2)/2}$$

where H is enthalpy in the flow channel and H_0 is the stagnation enthalpy. It is not difficult to show that the solutions of [18] are a combination of the previous solutions:

$$\frac{dM}{M} = \frac{2 + M^2(\gamma - 1)}{2(1 - M^2)} \left(\frac{\gamma M^2 f\, dz}{2\ D} - \frac{dA}{A} \right) \quad [19a]$$

$$\frac{dp}{p} = -\frac{\gamma M^2}{1 - M^2} \left(\frac{1 + (\gamma - 1)M^2 f\, dz}{2\ D} - \frac{dA}{A} \right) \quad [19b]$$

While in the frictionless nozzle case the critical condition ($M = 1$) occurs at the throat (and the solution can be continued in the diverging section with $M > 1$) and in the constant cross-section case the critical condition must occur at the end of the channel, when friction is allowed in a convergent–divergent nozzle the critical condition can occur in the divergent section. At the critical plane $A\gamma f/2D = dA/dz$. Since M would decrease after the throat if the nozzle were critical (with constant dA/dz) then this would require $A(z_t)\gamma f M^2(z_t)/2D > dA/dz$ (z_t is the location of the throat). At the critical location ($z^* > z_t$) where $M^2 = 1$ both dM/M and dp/p are indeterminant, but if the above critical conditions hold then the first derivatives (at least) are continuous across $M = 1$. These results are of significance in calculating the occurrences of critical flow.

A classification of singularities is usually done in terms of the independent variable [e.g. $f(z)$ may be singular at z^*]. In the previous discussion we have noticed that the derivatives of the dependent variables appear singular (or at least indeterminant) as a function of the dependent variable M. It may be mathematically improper to refer to the derivative of M with respect to z as having a "pole" at $M = 1$. But in fact, for these simple cases where explicit integrals can be found, expressions show that if $M = 1$ at $z = z^*$ then the classification of the point z^* (as regular, etc.) is the same as if we classified it from the viewpoint of M. Thus if [16a] reaches $M = 1$ at z^* then z^* is a pole of order 1 which is exactly the conclusion to be drawn if we classified it in terms of M. In the following we refer, therefore, to $M = 1$ as a singular point.

On a numerical grid, the downstream value is always a projection of the upstream values (even if they are all calculated simultaneously by matrix inversion) and the value follows the underlying shape function that is implicit in the spatial difference operators applied to the first order derivatives, i.e. nth order difference operators can only reproduce finite polynomial behavior up to order n. Thus, first-order difference operators follow linear behavior exactly, second-order difference operators follow second order behavior, etc. But, as a singularity is reached in the numerical solution, no difference operator can be "accurate". Depending on the structure of the singularity, refinement of the mesh may not be capable of producing a converging solution in the neighborhood of this singularity. Of greater importance, the existence of a spatial singularity cannot, realistically speaking, be resolved on a discrete mesh; one can expect that the projected variable is not finite and non-zero at the critical flow point but is out of range. The numerical schemes continue blind calculation across the critical flow location and can drive the pressure negative ($p_{n+1} = p_n + \Delta z\ dp/dz|_n$). Even if the location is established or a logic scheme is on hand to save the calculation, the so-called throat pressure or pressure-knee value may not be clearly resolved. For example, in considering the flow of single phase steam through a pipe of constant cross section, a strong dependence is found between the pressure at the mesh point before the singularity occurs and the structure of the mesh sizes well upstream of the critical flow location. In a typical full non-equilibrium analysis using a constant flow rate (cf. figure 1), the location of critical flow was found to be constant within ± 20 mm, varying only as the spatial mesh size varies. In all cases, a critical flow occurs after $z = 3$ m and is less than 3.05 m. If a change is made to an equilibrium analysis, the location moves farther out, but the observations do not depend on which model is used.

In figure 1, five nodalizations are shown, using a constant inlet flow rate and integrating the pressure derivative ([5]) up to the location $d\overline{GV}/dp = -1$. A logic cutoff is used to limit $p > 0$ as the deciding element and the various nodalizations are examined. The existence of a pressure-knee is clear; refining its value is difficult. Thus 30 mm nodalizations produce critical flow at 3.046 m; progressive refinements, down to 3×10^{-5} m, reduce the location to < 3.02 and make the knee more visible as somewhere between 3 and 3.15 MPa, from 5.4 MPa inlet pressure. However, such nodalizations, except conceivably for $\Delta z = 30$ mm, are unrealistic because in a real simulation fine

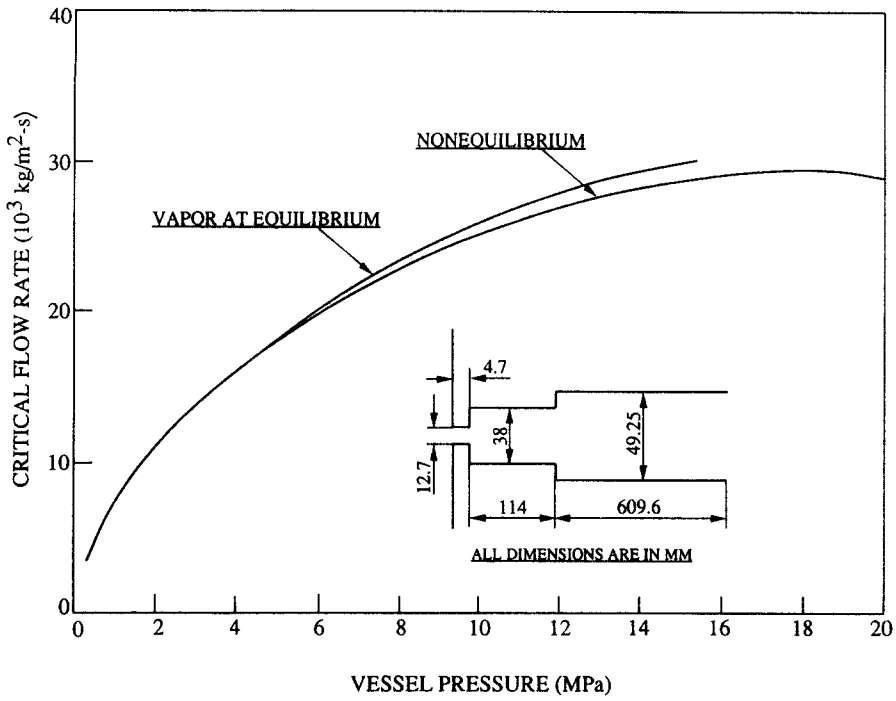

Figure 2. Simulation of the geometry of the Sozzi & Sutherland (1975) nozzle 3 experiment.

nodalization is required before each expansion, which is not economically feasible. In addition, it is not clear that the use of a first- or second-order differencing of the first spatial derivative is valid in the neighborhood of the singularity. Nevertheless, in the calculations to follow when spatially dependent models are used, increments consistent with the need to resolve the calculated critical flow rates to less than 1% (usually Δz of approx 3 mm) are used.

3.1. Contraction Losses

Critical flow occurs at an expansion, at least as far as the experiments are concerned. If a real jet is formed with a *vena contracta*, the minimum pressure occurs at that point. Whether the knee occurs at the expansion location or not is of no interest at this time,† as long as the critical flow is found at the location of the expansion, before the vena contracta (if any). Generally the knee also occurs before that condition because the structure of the equations does not contain a model for analyzing the formation of a jet.‡

The inlet to the pipe, crack, break, or other means of connecting a high pressure vessel to a low pressure environment involves a contraction. Figure 2 shows the simulation of the geometry of the Sozzi & Sutherland (1975) nozzle 3 experiment. After a series of calculations the geometry was reduced to the contraction and the nozzle (excluding the last two sections) without changing the results. The major question is accounting for the inlet pressure drop. It is clear from numerous studies that a jet should form at the contraction, and the vena contracta may be in the nozzle or in one of the larger sections. This question cannot be handled accurately within the available calculational tools, and the total contraction pressure drop is taken in the first increment following the contraction. This approach will be followed independently of the increment size.

4. CRITICAL FLOW MODELS

Two-phase critical flow models are generally divided into three categories:

- analytic;
- fitted functions;
- numerical solution of the conservation equations.

†It is very important to multidimensional calculations but not in the present context.
‡The formation of a jet is fundamentally a three-dimensional problem. No major systems code contains a jet model.

Analytical models are based on straightforward extensions of the single-phase flow formulations. In these models the compressible density and enthalpy are essentially replaced by their two-phase mixture counterparts. Early models assumed thermal and mechanical equilibrium between the two phases (Henry & Fauske 1971). Analytical solution can also be derived when the requirement for mechanical equilibrium is relaxed (Moody 1965), and when friction is assumed at the wall (Moody 1966).

More recent works account for interface mass and momentum transfer by employing a two-fluid formulation of the flow (Ardron 1978; Richter 1981; Dobran 1987; Lee & Schrock 1988). Solutions of the pressure and temperature distributions along the flow channel are, typically, accomplished by a numerical integration of the model's equations. Departures from thermal and mechanical (slip) equilibrium upstream of the critical location can also be taken into consideration by using the drift flux formulation (Elias & Chambré 1984; Chexal & Lellouche 1986).

Considering use within systems codes, the conservation equations themselves, as long as a momentum equation is present, clearly contain the critical flow condition; but perhaps because fine nodalization was recognized to be needed,† that the equations being solved were inadequate for the purpose, or for other reasons, an adjunct critical flow model was added to accommodate the flow out of a break. These critical flow models then became exit boundary conditions to the calculation. However, most of these analytic models require significant computer time; therefore, algebraic fits to the solutions of some of these models were created to reduce number crunching time. These fitted equations then replaced the original models in some of the more generally used systems codes (RETRAN); TRAC and RELAP5/MOD2 use even simpler explicit models. As simulation models became more realistic, the use of the built-in capabilities of the systems code could be expected to replace these adjunct models. In fact, that does not appear to have happened, probably because the cost of fine nodalization in the break or nozzle is still large.

In the following sections the capabilities and limitations of the existing two-phase critical flow models are discussed. The formulations that are presented are those used in the texts and original publications. Several of the more widely used models were programmed and extensively tested against existing experimental data.

4.1. Analytical Models

Analytical models of two-phase critical flow range from the homogeneous equilibrium model (HEM), which is essentially a single-phase flow model to methods that attempt to account for mechanical and thermal non-equilibrium phenomena. This section reviews the most widely used analytical models in roughly ascending order of complexity and evaluates their basic assumptions and limitations.

4.1.1. The homogeneous equilibrium model

This model, Henry & Fauske (1971) (subsequently referred to as HEM), is based on the assumption of isentropic, equilibrium flow. In such a case, the steady state‡ energy equation without heat input becomes, for flow between a still vessel and an ambient environment:

$$\frac{V^2}{2} + H(z) = H_o \qquad [20]$$

which yields

$$G = [2\bar{\rho}_t^2(H_o - H_t)]^{1/2} \qquad [21]$$

Here, G is constant (steady state), H_o refers to the enthalpy in the vessel§ and H_t and $\bar{\rho}_t$ are the enthalpy and density at the throat.¶ The throat conditions are determined by the following definitions, based on the assumption that the flow is isentropic:

$$x_t = \frac{s_o - s_L}{s_{LG}} \qquad [22a]$$

†In some codes fine nodalization solutions at abrupt area changes produce spurious choking.
‡All of the analytic models are developed from the steady-state equations.
§This is usually referred to as the "stagnation enthalpy".
¶If a converging–diverging nozzle is not in use, this refers to the vena contracta.

$$H_t = H_L + x_t H_{LG} \quad [22b]$$

$$\frac{1}{\bar{\rho}_t} = v_t = v_L + x_t v_{LG} \quad [22c]$$

$$\frac{1}{a_{HE}^2} = \frac{d\bar{\rho}_t}{dp} = \bar{\rho}_t^2 \left\{ \frac{dv_L}{dp} - \left(\frac{v_{LG}}{s_{LG}}\right)\frac{ds_L}{dp} + x\left[\frac{dv_{LG}}{dp}\left(\frac{v_{LG}}{s_{LG}}\right)\frac{ds_{LG}}{dp}\right]\right\} \quad [22d]$$

where s and s_o are the entropy and stagnation entropy respectively, a_{HE} is the homogeneous equilibrium speed of sound, and all liquid and vapor properties are calculated at the throat pressure assuming saturation conditions. It is now desired to maximize G with respect to pressure ($dG/dp = 0$); this is accomplished most easily by numerical means yielding p_t and G_c.

4.1.2. Non-homogeneous equilibrium model

This model, originally derived by Moody (1965), is an extension of the HEM model in that it permits different vapor and liquid velocities. A velocity ratio, S, defined as the ratio between the vapor and liquid velocities, is considered and treated as a variable which is determined by the conditions of maximum mass flux at the exit. Assuming that the phases exist at equal temperatures along the flow channel, [20] becomes

$$H + \frac{xV_G^2}{2} + \frac{(1-x)V_L^2}{2} = H_o \quad [23]$$

For a two-phase flow at thermal equilibrium the liquid and vapor velocities are:

$$V_L = \frac{G(1-x)}{\rho_L(1-\epsilon)} \quad [24a]$$

$$V_G = \frac{Gx}{\rho_G \epsilon} \quad [24b]$$

If the flow is approximated by an isentropic process, [22b] and [23] through [24b] yield:

$$G = (\rho''')_t \sqrt{2[H_o - H(p_t, s_0)]} \quad [25]$$

where the so-called energy density, ρ''', is defined by

$$\frac{1}{\rho'''} \equiv \left[\frac{x}{\rho_G} + \frac{S(1-x)}{\rho_L}\right]\left[x + \frac{1-x}{S^2}\right]^{1/2} \quad [26]$$

Considering equations [25] and [26] it is noted that for given stagnation conditions, the mass flux depends on both the local static pressure and the slip ratio, S. The choice of S is not unique but follows from the presumption that G should not only be maximized with respect to pressure but also with respect to the slip ratio.† Thus, the additional constrain $\partial G/\partial S|_p = 0$ (with a negative second derivative) leads [25] to yield at maximum flow conditions

$$S = \left(\frac{\rho_L}{\rho_G}\right)^{1/3} \quad [27]$$

Substituting [26] and [27] into [25], the critical mass flux can be solved again by searching for a pressure p_t which maximizes G. Note that [25], [26] reduce to the HEM relation [21] for $S = 1$.

The slip ratio described by [27] minimizes the specific kinetic energy of the two-phase mixture. A theoretical formulation for a slip ratio which minimizes the specific two-phase momentum was derived by Fauske (1962) who obtained

$$S = \left(\frac{\rho_L}{\rho_G}\right)^{1/2} \quad [28]$$

†That is satisfactory, but there is no *a priori* reason why the underlying physics should require this result. In fact, it does not do so.

4.1.3. Isenthalpic model

The approach is to solve all three conservation equations without recourse to considerations of entropy. A condition of isenthalpic expansion is assumed, which numerically appears to be reasonably well borne out when the equations are solved, and the following defining equations are considered:

Constant flow rate

$$GA = W_o \tag{29}$$

Constant enthalpy

$$H + \frac{1}{2}\frac{G^2}{\bar{\rho}^2} = H_o \tag{30}$$

Frictionless horizontal flow†

$$p + \frac{1}{2}\frac{G^2}{\bar{\rho}} = M'_o \tag{31}$$

where W is mass flow, M' is total momentum and the subscript o refers to the inlet conditions.

For homogeneous flow in thermal equilibrium, these equations can be readily solved for the throat quality‡ as:

$$x_t = 1 + \frac{H_o - H_G - (M'_o - p_t)v_G}{H_{LG} + (M'_o - p_t)v_{LG}} \tag{32}$$

The procedure for solving [29] through [32] for the critical flow is the same as for [21] and [24a]. First, a throat pressure, p_t, is selected (given H_o, M'_o etc.) and $G^2/\bar{\rho}_t$ is calculated from [31], then [32] is used to define x_t and [22c] to define $\bar{\rho}_t$ and then G; different values of p_t are searched until a maximum G is found. Note that H_t and $G^2/\bar{\rho}_t$ were algebraically eliminated between [30] and [31] to yield [32].

To use the isenthalpic model for the more general case with slip one needs to substitute $\bar{\rho}$ in [30] and [31] by ρ''' from [26]. This yields a quadratic equation for the throat quality as follows:

$$x_t H_{LG} + (M'_o - p_t)\left(\frac{x_t}{S\rho_G} + \frac{1 - x_t}{\rho_L}\right)\left[\frac{S^2 x_t + 1 - x_t}{S x_t + 1 - x_t}\right] = H_o - H_L \tag{33}$$

For homogeneous flows ($S = 1$) the isenthalpic model becomes identical to the HEM model, while for $S = (\rho_L/\rho_G)^{1/3}$ it becomes identical to the non-homogeneous equilibrium model.

4.1.4. Homogeneous non-equilibrium model

The analytical models just discussed, have been based on a thermodynamic derivation which does not use the two-phase speed of sound of Mach number as a critical condition. Consequently, when using, for instance, the assumption of homogeneous equilibrium flow, the predicted throat Mach number ($M \equiv G_c/a_{HE}\bar{\rho}_t$) may be greater than unity. This is true mainly for subcooled stagnation conditions and is a direct result of the discontinuous change in the homogeneous equilibrium speed of sound (cf. [22d]) at the transition from single- to two-phase flow. For saturated or two-phase stagnation conditions, the HEM yields $M = 1$ at the critical plane.

As stated in [12] and [13], the critical conditions can be derived by a mechanical approach directly from the conservation equations of two-phase flow. In this approach, however, the critical mass flux is not necessarily at its maximum value. A model which combines both the thermodynamic and the mechanical approaches was developed by Dickman *et al.* (1990). The model employs the isenthalpic equations, [29]–[31], assuming that the flow is homogeneous and that at the choking plane the liquid phase becomes metastable (superheated). The vapor phase is assumed to be at equilibrium with respect to the throat pressure.

†If G in the vessel is very small, then $M'_o \approx p_o$.

‡Remember that in homogeneous equilibrium flow $\bar{v} \equiv v_L + xv_{LG}$.

For a homogeneous non-equilibrium flow [29]–[31] yield†

$$x_t = \frac{H_o - H_L - (p_o - p_t)v_L}{H_{LG} + (p_o - p_t)v_{LG}} \quad [34]$$

Equations [29]–[31] and [34] are solved simultaneously, using a double iterative procedure, for G_c and for the liquid degree of superheat. In this method a throat pressure, p_t, and a liquid superheat, $\Delta T = T_L - T_s$, are searched for such that the criteria of G = maximum and M = 1 are met simultaneously at the throat. A homogeneous non-equilibrium speed of sound is defined as:

$$\frac{1}{a^2_{HNE}} = \frac{d\bar{\rho}_t}{dp} = \frac{d}{dp}\left\{\frac{1}{v_L + x_t v_{LG}}\right\} \quad [35]$$

The calculated degree of liquid superheat is shown to depend on the stagnation conditions. For subcooled conditions, the model predicts a non-zero degree of liquid superheat at the throat. However, since in this case, the throat quality is generally small, the flow could be approximated as an isentropic process. For saturated or two-phase stagnation conditions the predicted liquid superheat is vanishingly small and the model becomes equivalent to the HEM. This model has not been included in our comparative study.

4.1.5. Moody $\bar{f}L/D$ model

In long pipes, the effect of wall friction may become important in determining critical flow. This section is, therefore, included to show how friction effects can be included in critical two-phase flow calculations although it is not used in our comparative studies. A critical flow model with slip was developed by Moody (1966) to account for frictional effects in terms of a parameter $\bar{f}L/D$ where $\bar{f}$ is an average friction factor and L/D is the length-to-effective-diameter ratio.

Referring back to [3] or [5], we note that the frictional effects appear in the numerator and the critical condition refers to the denominator where $\partial \overline{GV}/\partial p = -1$. As one moves toward single-phase conditions, the critical condition depends on local pressure. Therefore, friction, by reducing pressure, will cause the pressure to reach the critical value earlier in space than if it were not taken into account. Note, however, that the values of the critical pressure and critical flow are not affected if friction is included in the analysis. One further important aspect of accounting for friction losses is that it is one way of taking into consideration the inlet contraction loss and accommodating subcooling. That is, the vessel pressure undergoes a sharp decrease on entering the pipe (crack, break, etc.) and this decrease—as shall be seen later—is usually the dominant cause for early vapor formation because it usually overrides any subcooling of the vessel liquid [i.e. after entering the crack (break, pipe, etc.) from the vessel, the liquid will be superheated]. In the usual LOCA scenario (double-ended discharging to the atmosphere), this effect may not be important; there is no contraction effect except, perhaps, well upstream.

This model is established for a pipe of constant flow area with no contraction and for steady-state so-called isenthalpic conditions. The basic equations are:

Mass

$$G = G_o \quad [36]$$

Momentum

$$G^2 \frac{d(1/\rho')}{dz} = -\left(\frac{dp}{dz} + \tau_w\right) \quad [37]$$

Energy

$$H_o = H_L + xH_{LG} + \frac{1}{2}\left(\frac{G}{\rho'''}\right)^2 \quad [38]$$

In [37] and [38], ρ' and ρ''' are the momentum and energy densities defined in [7] and [26], respectively. Subcooling can be taken into consideration by determination of the subcooling pressure decrement—the pressure at which liquid of a given temperature would be saturated. Equation [37] is solved for the length needed to reach this pressure after which vaporization starts.

†For subcooled stagnation conditions the vapor quality at the throat is small and [34] could be approximated by its isentropic counterpart $x_t = (s_o - s_L)/s_{LG}$.

To complete the model, τ_w is defined as:

$$\tau_w \equiv \phi_{lo}^2 f G^2 / 2\rho_L D \qquad [39]$$

with the two-phase multiplier given by:

$$\phi_{lo}^2 \equiv \left(\frac{1-x}{1-\epsilon}\right)^2 \qquad [40]$$

Solving [36] through [40] for the critical flow rate calls for an explicit numerical integration. This model is, therefore, the first to be considered, which does not lead to an algebraic, albeit transcendental, equation but only to recursive quadratures. Effectively, one integrates spatially many times until a maximum is found numerically.

The usual approach at this point is to define a series of special functions made up of partial derivatives of the various quantities (Moody 1966) and then write a single integral of [37]. Thus the momentum equation is expanded to yield:

$$\frac{dp}{dz}\left[-1 + G^2 \left.\frac{\partial v'}{\partial p}\right|_x\right] + G^2 \left.\frac{\partial v'}{\partial x}\right|_p \frac{dx}{dz} = -\tau_w \qquad [41]$$

where $v' \equiv 1/\rho'$.

The next step is to note that H_o is a function of (x, p) and is assumed to be constant, thus:

$$\left.\frac{\partial H_o}{\partial x}\right|_p dx + \left.\frac{\partial H_o}{\partial p}\right|_p dp = 0 \qquad [42]$$

from which:

$$\frac{dx}{dz} = -\frac{\left.\dfrac{\partial H_o}{\partial p}\right|_x}{\left.\dfrac{\partial H_o}{\partial x}\right|_p} \frac{dp}{dz} \qquad [43]$$

and [41] becomes:

$$\left\{1 + G^2 \left.\frac{\partial v'}{\partial p}\right|_x - G^2 \left.\frac{\partial v'}{\partial x}\right|_p \frac{\left.\dfrac{\partial H_o}{\partial p}\right|_x}{\left.\dfrac{\partial H_o}{\partial x}\right|_p}\right\} \frac{dp}{dz} = -\tau_w \qquad [44]$$

or using [39]:

$$\frac{2\rho_L F(p, G)\, dp}{G^2\left[1 + \left(\dfrac{\rho_L}{S\rho_G} - 1\right)x\right]^2} = -\frac{f}{D} dz \qquad [45]$$

The function F is given by:

$$F(p, G) \equiv G^2 \left\{ \left.\frac{\partial v'}{\partial x}\right|_p \frac{\left.\dfrac{\partial H_o}{\partial p}\right|_x + \dfrac{G^2}{2}\left.\dfrac{\partial (v''')^2}{\partial p}\right|_x}{\left.\dfrac{\partial H_o}{\partial x}\right|_p + \dfrac{G^2}{2}\left.\dfrac{\partial (v''')^2}{\partial x}\right|_p} - \left.\frac{\partial v'}{\partial p}\right|_x \right\} - 1 \qquad [46]$$

If $\bar{f}$ is the average value of f over the length L then:

$$\int_{p_2}^{p_1} \frac{2\rho_L F(p, G)\, dp}{G^2\left[1 + \left(\dfrac{\rho_L}{S\rho_G} - 1\right)x\right]^2} = -\bar{f}\frac{L}{D} \qquad [47]$$

is the quadrature of interest. The optimization method is to choose p_t, find G from [47] and repeat with different values of p_t until G is at a maximum. It may be simpler to pick a value for G and solve for p_t because G^2 appears under the integral. Then either one or two values for p_t will be associated with each value of G^2; G^2 is varied until the two values of p_t are sufficiently close to presume $dG/dp_t \approx 0$.

The upper limit, p_1, on the integral is the value of the pressure after the contraction. An estimate of the pressure drop $p_o - p_1$ may be introduced into the calculation by assuming an isentropic entrance condition

$$s(p_o, H_o) = s_L(p_1) + x_1 s_{LG}(p_1) \quad [48]$$

Equation [48] can be applied to obtain the pressure p_1. Note that p_1 is itself a function of G, which makes the "pick G and solve for p_t" method somewhat more direct. In this case, x_1 (if any) is calculated from [38]. Originally the slip relation defined by [27] was applied in this model.

4.1.6. The Burnell model

Burnell (1947) makes use of an empirical correlation for the critical pressure. The liquid temperature and density at the exit were assumed to be equal to the stagnation (vessel) values. The Bernoulli equation, between the vessel and the critical location, was applied to calculate the mass flux. The critical pressure was estimated using an empirical equation. Thus,

$$G_c = [2\rho_o(p_o - p_t)]^{1/2} \quad [49a]$$

$$p_t = p_s(T_o)[1 - 0.264\sigma(T_o)/49.2] \quad [49b]$$

where σ is surface tension.

This model should have its greatest application for $L/D < 1$.

4.1.7. The extended Henry–Fauske model

The extended Henry–Fauske (H–F) model (Henry & Fauske 1971) is complex to use but quite simple in conception. The derivative is fairly involved but can be simplified by noting that since it is a solution solely of the momentum equation in the absence of friction and head effects, we could start with the simplified form of [5]:

$$\frac{dp}{dz} + \frac{d\overline{GV}}{dz} = 0 \quad [50]$$

from which the critical flow condition is $\partial\overline{GV}/\partial p = -1$ (cf. [8]).

Equation [50] is now integrable leading to

$$\overline{GV} + p = \overline{GV}(0) + (p(0) - \Delta p_{IR}) \quad [51]$$

where Δp_{IR} is the irreversible pressure drop caused by area change (contraction or expansion) at the inlet to the flow channel. If the integration is carried out from the stagnation point to the throat, [51] can be rearranged as:

$$G_c^2 = \frac{p(0) - p_t - \Delta p_{IR}}{f(x_t, p_t) - f(x_o, p_o)} \quad [52a]$$

where

$$f(x, p) = \frac{xS + (1 - x)}{S}[(1 - x)Sv_L + xv_G] \quad [52b]$$

Equation [52a] can be restated in a differential form as

$$\frac{1}{G_c^2} = \left.\frac{df(x, p)}{dp}\right|_t \quad [53]$$

If one could evaluate the derivatives involved, one should be able to close and solve these equations. It is here that the basic structure of the Henry–Fauske model is established. The derivative introduces four terms: dx/dp, $d\rho_G/dp$, $d\rho_L/dp$ and dS/dp. These are readily obtained by introducing the following assumptions:

(1) the amount of mass transferred in the expansion is negligible, $x_t \approx x_o$;
(2) the liquid temperature is constant throughout the process, $T_{Lt} = T_{Lo}$;
(3) the phase velocities are equal, $S = 1$;
(4) the system entropy during the expansion can be assumed constant, $ds_o = 0$;
(5) the liquid at the throat is incompressible, $dv_L/dp\,|_t = 0$;

(6) the vapor can be described by a polytropic process such that $dv_G/dp\,|_t = v_G/np|_t$, where n is a thermal equilibrium polytropic exponent;
(7) the velocity ratio at the throat reaches a minimum, $dS/dp\,|_t = 0$.

Furthermore, it is noticed that at the throat, the local heat and mass transfer *rates* are large. The rate of mass transfer at the throat was correlated by

$$\left.\frac{dx}{dp}\right|_t = -\left[\frac{(1-x_o)\dfrac{ds_L}{dp} + x_o\dfrac{ds_G}{dp}}{s_{Go} - s_{Lo}}\right] = N\left.\frac{dx_E}{dp}\right|_t \qquad [54]$$

where N is a non-equilibrium parameter defined by fitting to experimental data and the equilibrium quality, x_E is given by

$$x_E = \frac{s_o - s_L}{s_G - s_L}$$

where s_G and s_L are the vapor and liquid saturation entropies and s_o is the inlet stagnation mixture entropy. Note that x_o is not a flow quality but equals $\epsilon\rho_G/\bar{\rho}$; this will fit well with the final assumption that $S = 1$ and avoids the contradictions that would arise if $S \neq 1$.

The above approximations for x_t, $dx/dp|_t$ and $dS/dp|_t$ simplify the critical flow rate expression to

$$G_c^2 = \left[\frac{x_o}{np\rho_G} + \left(\frac{1}{\rho_G} - \frac{1}{\rho_{Lo}}\right)\left\{\frac{(1-x_o)N}{s_{GE} - s_{LE}}\frac{ds_{LE}}{dp} - \frac{x_o Cp_G(1/n - 1/\gamma)}{p(s_{Go} - s_{Lo})}\right\}\right]_t^{-1} \qquad [55]$$

Equation [55] requires the throat pressure for calculating G_c. The throat conditions can be calculated by coupling [55] with the momentum equation along the flow path. Starting with the simplified form of [5], Henry & Fauske reduce it under all the assumptions above to

$$d(V^2/2) = -[(1-x_o)v_{Lo} + x_o v_G(p)]\,dp \qquad [56]$$

Considering the isentropic expansion process previously introduced,

$$p_o(v_{Go})^\gamma = p_t(v_{Gt})^\gamma$$

Equation [56] can be integrated between the stagnation and throat locations to yield (noting that $V_o = 0$)†

$$\left\{\frac{1-x_o}{\rho_{Lo}} + \frac{x_o}{\rho_{Gt}}\right\}^2 \frac{G_c^2}{2} = \frac{1-x_o}{\rho_{Lo}}(p_o - p_t) + \frac{x_o\gamma}{\gamma - 1}\left(\frac{p_o}{\rho_{Go}} - \frac{p_t}{\rho_{Gt}}\right) \qquad [57]$$

Equations [55] and [57] can be solved for G_c and the throat pressure. Eliminating G_c between [55] and [57] yields a transcendental expression for the throat pressure. Note, however, that the full momentum equation leads to [52a] which under the H–F assumptions yields the exact and much simpler result

$$G_c^2 = \frac{p_o - p_t - \Delta p_{IR}}{x_o(v_{Gt} - v_{Go})}$$

This formulation would require Δp_{IR} to be evaluated.‡ The boundary condition used is $V_o = 0$ ($\Delta p_{IR} > 0$).

The H–F model in its final form solves [55] and [57]. This formulation requires the solution of a non-linear equation for the throat pressure (i.e. where $dp/dz \to \infty$); and as such there is some difficulty with experimental comparisons and the numerical solution technique is more complex than is desirable for a systems code boundary condition. As a result the De Young (1975) curve fit to this model tends to be used more than the original model is (see ahead to section 4.2.2).

4.2. Fitted Models (The RETRAN Procedures)

The analytic models discussed above (except Burnell's) end with implicit algebraic or numerical forms. The solution for the critical mass flow rate thus involves time-consuming calculations. One

†Presumably this is done to avoid the need to consider Δp_{IR} effects.
‡Presumably [57], the H–F result, is independent of area change effects.

way out of such a situation is to "fit" the solution to a simpler form which yields the critical flow directly in the form:

$$G_c = f_1(p_1, H_o, \bar{f}L/D)$$

or using the area ratio σ'

$$G_c = f_2(p_o, H_o, \bar{f}L/D, \sigma')$$

One can then compare the local mass flow rate with G_c and determine if critical flow has been reached,† after which no further increase in flow is permitted through that location. Clearly, this is a more efficient way to use the models. However, the major problem lies in the adequacy of the fit. Thus, in developing fitted equations such as the above, the original model is used to produce "data" which are then fitted by a least squares or other process to yield a polynomial approximation. This final result must statistically be considered a totally separate model and compared independently with data. If for example, μ is the mean error between the model and experimental data and σ the standard deviation while θ is the mean error between the model and the fit to the model, then the mean error between the fit and the experimental data is $\mu + \theta$. The standard deviation between experiment and fit cannot be expressed directly unless further assumptions are made concerning randomness. The result is that such a fit may be better or worse than the original model when it is compared to data. The fitted models we examined are those used in RETRAN (McFadden *et al.* 1984).

4.2.1. Moody fit

Consider a fit to the Moody model discussed in section 4.1.2. The functional form for this fit is an expansion in pressure and enthalpy.

$$G_c^{\text{Moody}}(p, H) = \begin{cases} \exp\left(\sum_{j=0}^{5}\sum_{i=0}^{5} M_{1i,j} p^j H^i\right) & 15 < p < 200 \text{ psia} \\ \sum_{j=0}^{5}\sum_{i=0}^{5} M_{2i,j} p^j H^i & 200 < p < 3000 \text{ psia} \end{cases} \quad [58]$$

The constant coefficients, $M_{1i,j}$ and $M_{2i,j}$, in these expressions are listed in table 1. The domains of validity in the p–H plane are depicted in figure 3. This fit is meant to be used only inside the saturation envelope, i.e. saturated or two-phase inlet conditions.

4.2.2. Extended Henry–Fauske fit

The original model developed by Henry & Fauske (1971) attempts to determine the critical flow in a converging (De Laval) nozzle, neglecting wall friction. By making use of an extensive set of assumptions, the authors developed a final result which is extremely complicated to use directly. A discharge coefficient is used when applying this model for orifices or tubes.

Within the structure of RETRAN (McFadden *et al.* 1984), this model is used only for subcooled inlet conditions in the regions shown in figure 3. The fitted form is given by:

$$G_c^{\text{EHF}}(p, H) = \begin{cases} \sum_{j=0}^{5}\sum_{i=0}^{5} N_{1i,j} p^j H^i & 15 < p < 300 \text{ psia} \\ \sum_{j=0}^{5}\sum_{i=0}^{5} N_{2i,j} p^j H^i & 300 < p < 3000 \text{ psia} \end{cases} \quad [59]$$

The constant coefficients, $N_{1i,j}$ and $N_{2i,j}$, in these expressions are listed in table 2.

4.2.3. Isenthalpic model fit

Although the isenthalpic model was developed without regard to considerations of entropy in section 3, a somewhat different result can be established by assuming that entropy is constant. Thus

†Remember that this method is the way the system's codes actually use such models.

Table 1. Constant coefficients in expressions for Moody critical flow as a function of stagnation pressure and specific enthalpy

				$M_{1i,j}$		
i/j	0	1	2	3	4	5
0	0.75398883×10^{1}	0.48635447×10^{0}	$-0.14054847 \times 10^{-1}$	$0.18252651 \times 10^{-3}$	$-0.10492510 \times 10^{-5}$	$0.21537617 \times 10^{-8}$
1	$-0.27349762 \times 10^{-1}$	$-0.25172525 \times 10^{-2}$	$-0.90215743 \times 10^{-4}$	$-0.12541056 \times 10^{-5}$	$0.74318133 \times 10^{-8}$	$-0.15500316 \times 10^{-10}$
2	$0.77033614 \times 10^{-4}$	$0.66198222 \times 10^{-5}$	$-0.25893147 \times 10^{-6}$	$0.36860723 \times 10^{-8}$	$-0.22032243 \times 10^{-10}$	$0.46118179 \times 10^{-13}$
3	$-0.11597165 \times 10^{-6}$	$-0.84665377 \times 10^{-8}$	$0.35752133 \times 10^{-9}$	$-0.51915992 \times 10^{-11}$	$0.31249946 \times 10^{-13}$	$-0.65601247 \times 10^{-16}$
4	$0.85314613 \times 10^{-10}$	$0.52492322 \times 10^{-11}$	$-0.23790918 \times 10^{-12}$	$0.35151649 \times 10^{-14}$	$-0.21287482 \times 10^{-16}$	$0.44796907 \times 10^{-19}$
5	$-0.24171538 \times 10^{-13}$	$-0.12636194 \times 10^{-14}$	$0.61256651 \times 10^{-16}$	$-0.91925726 \times 10^{-18}$	$0.55968113 \times 10^{-20}$	$-0.11802990 \times 10^{-22}$
				$M_{2i,j}$		
i/j	0	1	2	3	4	5
0	0.64582892×10^{4}	0.15724915×10^{3}	$-0.16101131 \times 10^{0}$	$-0.14741137 \times 10^{-4}$	$0.61947560 \times 10^{-7}$	$-0.19206668 \times 10^{-10}$
1	$-0.59379818 \times 10^{2}$	$-0.76566784 \times 10^{0}$	$0.11162190 \times 10^{-2}$	$-0.18726780 \times 10^{-6}$	$-0.22806979 \times 10^{-9}$	$0.88455810 \times 10^{-13}$
2	0.19040194×10^{0}	$0.14863253 \times 10^{-2}$	$-0.27575375 \times 10^{-5}$	$0.85169692 \times 10^{-9}$	$0.30284416 \times 10^{-12}$	$-0.16287505 \times 10^{-15}$
3	$-0.27991119 \times 10^{-3}$	$-0.13833255 \times 10^{-5}$	$0.31653794 \times 10^{-8}$	$-0.12626170 \times 10^{-11}$	$-0.16803993 \times 10^{-15}$	$0.15109240 \times 10^{-18}$
4	$0.19327093 \times 10^{-6}$	$0.60309542 \times 10^{-9}$	$-0.17199274 \times 10^{-11}$	$0.79444415 \times 10^{-15}$	$0.29596473 \times 10^{-19}$	$-0.71294533 \times 10^{-22}$
5	$-0.50859277 \times 10^{-10}$	$-0.95031339 \times 10^{-13}$	$0.35699646 \times 10^{-15}$	$-0.18158912 \times 10^{-18}$	$0.17431814 \times 10^{-23}$	$0.13825335 \times 10^{-25}$

Table 2. Constant coefficients in expressions for Henry–Fauske critical flow as a function of stagnation pressure and specific enthalpy

				$H_{1i,j}$		
i/j	0	1	2	3	4	5
0	0.11971131×10^{5}	$-0.25664444 \times 10^{3}$	$-0.11154016 \times 10^{3}$	0.14181940×10^{1}	$-0.57956498 \times 10^{-2}$	$0.77436012 \times 10^{-5}$
1	$-0.29275019 \times 10^{3}$	0.40495998×10^{2}	0.17440962×10^{1}	$-0.25888201 \times 10^{-1}$	$0.11065153 \times 10^{-3}$	$-0.15104216 \times 10^{-6}$
2	0.13088631×10^{1}	$-0.60219912 \times 10^{0}$	$-0.93144283 \times 10^{-2}$	$0.17982760 \times 10^{-3}$	$-0.81656598 \times 10^{-6}$	$0.11454533 \times 10^{-8}$
3	$0.96555931 \times 10^{-2}$	$0.34802345 \times 10^{-2}$	$0.15567712 \times 10^{-4}$	$-0.57489343 \times 10^{-6}$	$0.28585300 \times 10^{-8}$	$-0.41616729 \times 10^{-11}$
4	$-0.85871644 \times 10^{-4}$	$-0.85504973 \times 10^{-5}$	$0.13551325 \times 10^{-7}$	$0.81339877 \times 10^{-9}$	$-0.46830222 \times 10^{-11}$	$0.71809283 \times 10^{-14}$
5	$0.16193695 \times 10^{-6}$	$0.71823710 \times 10^{-8}$	$-0.41240653 \times 10^{-10}$	$-0.38055461 \times 10^{-12}$	$0.28432048 \times 10^{-14}$	$-0.46890691 \times 10^{-17}$
				$H_{2i,j}$		
i/j	0	1	2	3	4	5
0	0.11996419×10^{5}	0.33614071×10^{2}	$-0.34555139 \times 10^{-1}$	$0.27341308 \times 10^{-4}$	$-0.10430915 \times 10^{-7}$	$0.13430502 \times 10^{-11}$
1	$-0.66516773 \times 10^{2}$	$-0.21670146 \times 10^{0}$	$0.48840252 \times 10^{-3}$	$-0.43249560 \times 10^{-6}$	$0.16802644 \times 10^{-9}$	$-0.21923832 \times 10^{-13}$
2	0.25523516×10^{0}	$0.18031256 \times 10^{-2}$	$-0.35661004 \times 10^{-5}$	$0.28854007 \times 10^{-8}$	$-0.10625928 \times 10^{-11}$	$0.13604749 \times 10^{-15}$
3	$-0.44088343 \times 10^{-3}$	$-0.57669789 \times 10^{-5}$	$0.10431626 \times 10^{-7}$	$-0.78849169 \times 10^{-11}$	$0.27918999 \times 10^{-14}$	$-0.35206568 \times 10^{-18}$
4	$-0.53252751 \times 10^{-6}$	$0.98378584 \times 10^{-8}$	$-0.15532591 \times 10^{-10}$	$0.10650136 \times 10^{-13}$	$-0.35327078 \times 10^{-17}$	$0.43073516 \times 10^{-21}$
5	$0.76399011 \times 10^{-9}$	$-0.64276860 \times 10^{-11}$	$0.93866385 \times 10^{-14}$	$-0.59412445 \times 10^{-17}$	$0.18329776 \times 10^{-20}$	$-0.21322858 \times 10^{-24}$

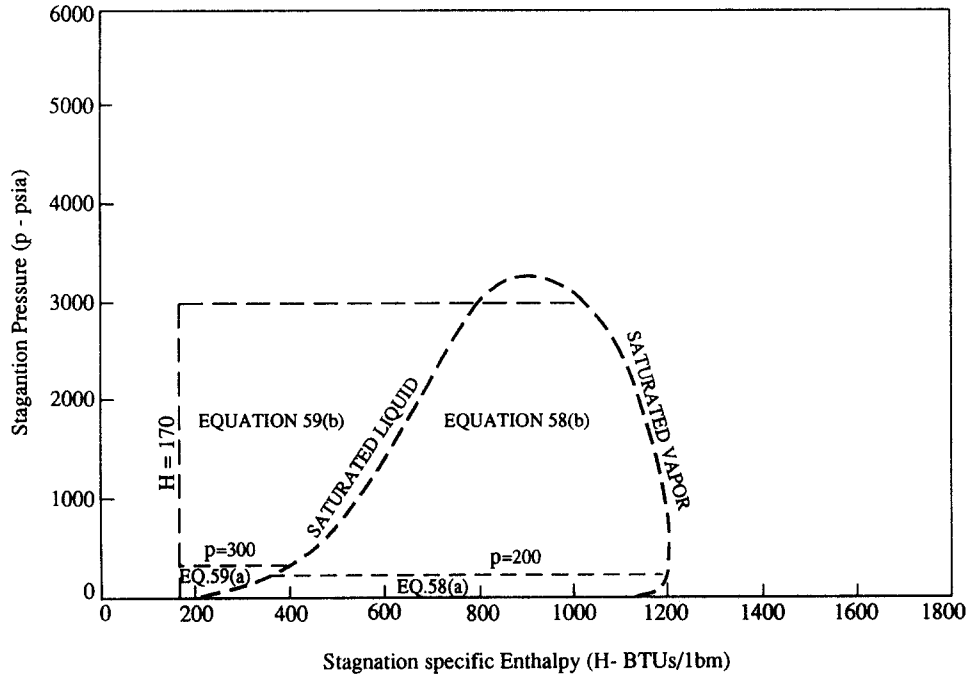

Figure 3. The domains of validity in the p–H plane of the fits to Moody and the extended Henry–Fauske models ([58],[59]).

$1/\bar{\rho} \equiv x/\rho_G + (1-x)/\rho_L$ was assumed, a condition which follows from $V \equiv G/\bar{\rho}$ when the slip, $S = 1$. Under the assumption of a constant entropy expansion, use could have been made of the thermodynamic condition $\mathrm{d}h/\mathrm{d}p|_s \equiv 1/\bar{\rho}$ and a different critical flow condition would have been found.

In the RETRAN manual (McFadden *et al.* 1984), this model is referred to as a fit to the isenthalpic model. In fact, if the constant entropy condition is applied, as it is in RETRAN, this model is the same as the HEM model. It continues to be referred to as a fit to the isenthalpic model because that is how the literature refers to it.

De Young (1975) solved this model for a wide range of inlet conditions, which were used to prepare the following fitting equations:

Low pressure range ($14.7 < p < 100$ psia):

$$G_c^{ISO}(p,H) = \begin{cases} \sum_{j=0}^{5}\sum_{i=0}^{5} I_{1i,j} p_1^j H_1^i & \text{subcooled} \quad 8 \leqslant H \leqslant H_s \\ \sum_{j=0}^{5}\sum_{i=0}^{5} I_{2i,j} p^j H_2^i & \text{2-phase} \quad H_s \leqslant H \leqslant 1750 \end{cases} \qquad [60]$$

where H_s is the saturated liquid enthalpy, $p_1 = 750p^{0.5}$, $H_1 = 5500 - 2.3 \times 10^{-10} \times H^6$ and $H_2 = 5900\exp(-0.0013733H)$ in British units.

In the mid-pressure range ($100 < p < 2800$ psia):

$$G_c^{ISO}(p,H) = \begin{cases} \sum_{j=0}^{5}\sum_{i=0}^{5} I_{3i,j} p_3^j H_3^i & \text{subcooled} \quad 8 \leqslant H \leqslant H_s \\ \sum_{j=0}^{5}\sum_{i=0}^{5} I_{4i,j} p^j H_4^i & \text{2-phase} \quad H_s \leqslant H \leqslant 1750 \end{cases} \qquad [61]$$

where $p_3 = 58.863p^{0.75}$, $H_3 = 20000 - 0.05389H^2$ and $H_4 = 50000\exp(-0.0013733H)$.

In the high pressure range ($2800 < p < 6000$ psia):

$$G_c^{ISO}(p, H) = \begin{cases} \sum_{j=0}^{5}\sum_{i=0}^{5} I_{5i,j} p^j H_5^i & \text{subcooled} \quad 250 \leqslant H \leqslant 800 \\ \sum_{j=0}^{5}\sum_{i=0}^{5} I_{6i,j} p_6^j H_6^i & \text{2-phase} \quad 800 \leqslant H \leqslant 1750 \end{cases} \qquad [62]$$

where $p_6 = 22000 + 7.36842p$, $H_5 = 5900\exp(-0.0013733H)$ and $H_6 = 50000 - 0.06173H^2$.

The constant coefficients, $I_{li,j}$, in the expressions [60] through [62] are listed in table 3(a)–(c). The domains of validity in the p–H plane are depicted in figure 4.

In use, these models may be mixed (Moody to isenthalpic, etc.). In such a situation, a transition region must be introduced to eliminate jump discontinuities at region boundaries. The specific details of how this is accomplished in RETRAN are found in McFadden *et al.* (1984).

4.3. Numerical Solutions

The value of an analytical solution lies in the insight gained about general variations of parameters. Yet, there must be some general validity to the underlying theory that is used if the results are not to be merely exercises in analysis. The plethora of models now extant results from the requirement to produce full-range-capable solution methods before significant experimental data were available to validate the models in any statistical sense. Yet, in examining the models, one can conclude that the results of disparate assumptions (e.g. iso—or non-iso—whatever) without significant relevant data comparison are simply exercises.

The underlying phenomena which apparently control critical flow in two-phase, one-component flow appear to be:

- contraction pressure loss (leading to superheating of the liquid);
- flashing of superheated liquid (leading to vapor mass flow);
- the relation between void fraction and flow quality;
- pressure drop due to increasingly positive momentum flux (and, in many, cases significant wall friction).

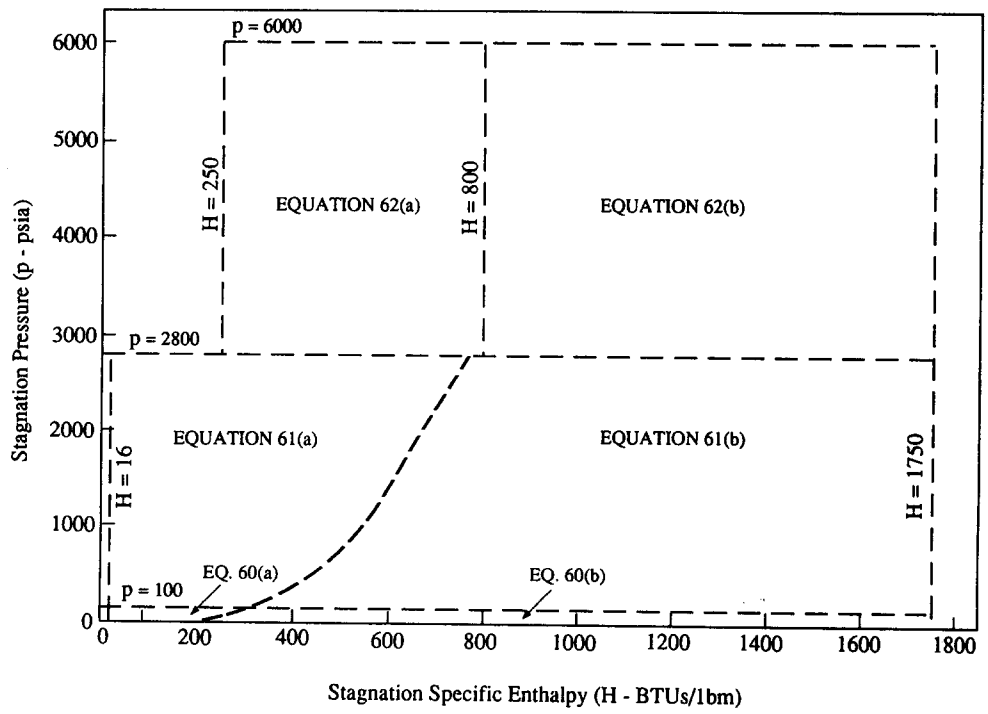

Figure 4. The domains of validity in the p–H plane of the fits to the isenthalpic model ([60],[61]).

Table 3(a). Constant coefficients in expressions for isoenthalpic expansion critical flow as a function of stagnation pressure and specific enthalpy

			$I_{1i,j}$			
i/j	0	1	2	3	4	5
0	$-0.61079017 \times 10^{6}$	0.35835693×10^{3}	$-0.82113001 \times 10^{-1}$	$0.92074993 \times 10^{-5}$	$-0.50256939 \times 10^{-9}$	$0.10656235 \times 10^{-13}$
1	0.17723792×10^{3}	$-0.85173920 \times 10^{-1}$	$0.15133113 \times 10^{-4}$	$-0.12069593 \times 10^{-8}$	$0.40839937 \times 10^{-13}$	$-0.39301326 \times 10^{-18}$
2	$-0.15259033 \times 10^{-1}$	$0.46248520 \times 10^{-5}$	$-0.14319090 \times 10^{-9}$	$-0.77321077 \times 10^{-13}$	$0.87190503 \times 10^{-17}$	$-0.26645196 \times 10^{-21}$
3	$0.59775167 \times 10^{-6}$	$-0.16855193 \times 10^{-9}$	$0.16596792 \times 10^{-13}$	$-0.94175361 \times 10^{-18}$	$0.54924497 \times 10^{-22}$	$-0.18513150 \times 10^{-26}$
4	$-0.33084180 \times 10^{-11}$	$0.49957406 \times 10^{-15}$	$0.10894667 \times 10^{-19}$	$-0.39065314 \times 10^{-23}$	$0.75466939 \times 10^{-28}$	$0.35921080 \times 10^{-32}$
5	$-0.27603377 \times 10^{-16}$	$0.33248852 \times 10^{-20}$	$-0.18476858 \times 10^{-24}$	$0.14786815 \times 10^{-28}$	$0.20499051 \times 10^{-33}$	$-0.53964250 \times 10^{-37}$

			$I_{2i,j}$		
i/j	0	1	2	3	4
0	$-0.21851768 \times 10^{1}$	0.82610264×10^{0}	$-0.39296656 \times 10^{-1}$	$0.24894000 \times 10^{-3}$	$-0.38481513 \times 10^{-6}$
1	$0.77226019 \times 10^{-2}$	$0.45429711 \times 10^{-3}$	$0.15811982 \times 10^{-3}$	$-0.98756816 \times 10^{-6}$	$0.15181668 \times 10^{-8}$
2	$-0.94283873 \times 10^{-5}$	$0.14299562 \times 10^{-5}$	$-0.22417512 \times 10^{-6}$	$0.13771995 \times 10^{-8}$	$-0.21029987 \times 10^{-11}$
3	$0.51095086 \times 10^{-8}$	$-0.10919498 \times 10^{-8}$	$0.14040350 \times 10^{-9}$	$-0.84745729 \times 10^{-12}$	$0.12845429 \times 10^{-14}$
4	$-0.12429312 \times 10^{-11}$	$0.31314774 \times 10^{-12}$	$-0.39756584 \times 10^{-13}$	$0.23478555 \times 10^{-15}$	$-0.35282311 \times 10^{-18}$
5	$0.11033567 \times 10^{-15}$	$-0.30232812 \times 10^{-16}$	$0.41644534 \times 10^{-17}$	$-0.23853748 \times 10^{-19}$	$0.35476040 \times 10^{-22}$

Table 3(b). Constant coefficients in expressions for isoenthalpic expansion critical flow as a function of stagnation pressure and specific enthalpy

			$I_{3i,j}$		
i/j	0	1	2	3	4
0	0.23396109×10^{6}	$-0.52765454 \times 10^{2}$	$0.43211218 \times 10^{-2}$	$-0.14844802 \times 10^{-6}$	$0.18711342 \times 10^{-11}$
1	$-0.10755023 \times 10^{3}$	$0.20440480 \times 10^{-1}$	$-0.14090500 \times 10^{-5}$	$0.42549018 \times 10^{-10}$	$-0.47722081 \times 10^{-15}$
2	$0.14546479 \times 10^{-1}$	$-0.22721603 \times 10^{-5}$	$0.12791578 \times 10^{-9}$	$-0.30319026 \times 10^{-14}$	$0.24694464 \times 10^{-19}$
3	$-0.87942880 \times 10^{-6}$	$0.11159414 \times 10^{-9}$	$-0.48684729 \times 10^{-14}$	$0.78514401 \times 10^{-19}$	$-0.24454354 \times 10^{-24}$
4	$0.25418710 \times 10^{-10}$	$-0.26125639 \times 10^{-14}$	$0.93851532 \times 10^{-19}$	$-0.15480205 \times 10^{-23}$	$0.14229046 \times 10^{-28}$
5	$-0.29079157 \times 10^{-15}$	$0.25300892 \times 10^{-19}$	$-0.10895948 \times 10^{-23}$	$0.41673812 \times 10^{-28}$	$-0.80302624 \times 10^{-33}$

			$I_{4i,j}$	
i/j	0	1	2	3
0	0.94440375×10^{2}	0.68202161×10^{0}	$0.22277618 \times 10^{-3}$	$-0.68481663 \times 10^{-7}$
1	$-0.70532888 \times 10^{-1}$	$0.47739930 \times 10^{-3}$	$-0.16796720 \times 10^{-6}$	$0.53600389 \times 10^{-10}$
2	$0.14151552 \times 10^{-4}$	$-0.49292500 \times 10^{-7}$	$0.36261394 \times 10^{-10}$	$-0.11953664 \times 10^{-13}$
3	$-0.94543999 \times 10^{-9}$	$0.22344108 \times 10^{-11}$	$-0.30279729 \times 10^{-14}$	$0.10518184 \times 10^{-17}$
4	$0.19256386 \times 10^{-13}$	$-0.26353127 \times 10^{-16}$	$0.11323359 \times 10^{-18}$	$-0.33126657 \times 10^{-22}$

Table 3(c). Constant coefficients in expressions for isoenthalpic expansion critical flow as a function of stagnation pressure and specific enthalpy

			$I_{5i,j}$	
i/j	0	1	2	3
0	0.13922324×10^{6}	$-0.85183342 \times 10^{1}$	$0.17344230 \times 10^{-3}$	$-0.10770670 \times 10^{-8}$
1	0.55483258×10^{0}	$-0.67033465 \times 10^{-4}$	$0.19159431 \times 10^{-8}$	$-0.13962161 \times 10^{-13}$
2	$-0.10206096 \times 10^{-3}$	$0.50562629 \times 10^{-8}$	$-0.79809531 \times 10^{-13}$	$0.42688713 \times 10^{-18}$
3	$-0.14516886 \times 10^{-8}$	$0.76341357 \times 10^{-13}$	$-0.12984123 \times 10^{-17}$	$0.73587201 \times 10^{-23}$
4	$-0.52974405 \times 10^{-14}$	$0.28362334 \times 10^{-18}$	$-0.49216747 \times 10^{-23}$	$0.28301033 \times 10^{-28}$

			$I_{6i,j}$	
i/j	0	1	2	3
0	0.67095585×10^{7}	$-0.46985672 \times 10^{4}$	0.10797070×10^{1}	$-0.80901658 \times 10^{-4}$
1	$-0.87672192 \times 10^{3}$	0.61458710×10^{0}	$-0.14215439 \times 10^{-3}$	$0.10722893 \times 10^{-7}$
2	$0.41252890 \times 10^{-1}$	$-0.29071947 \times 10^{-4}$	$0.67976539 \times 10^{-8}$	$-0.51734035 \times 10^{-12}$
3	$-0.83260068 \times 10^{-6}$	$0.59326327 \times 10^{-9}$	$-0.14056658 \times 10^{-12}$	$0.10810246 \times 10^{-16}$
4	$0.61173830 \times 10^{-11}$	$-0.44261205 \times 10^{-14}$	$0.10648646 \times 10^{-17}$	$-0.82851421 \times 10^{-22}$

These phenomena require three constitutive relations (or four if wall friction is accounted for):

- contraction loss model;
- flashing model;
- void/quality model;
- wall friction model.

The question whether the flow is isentropic, isenthalpic, isoenergetic or other can be determined (within reason) by detailed numerical calculations. Detailed fine mesh calculations with six equation models are required to make use of this path. One would start with a model that has already been shown to be statistically valid in both diabatic and adiabatic flow where the additional, if any, requirements needed to extend the constitutive relations into the very high velocity critical flow regime would be examined.

Consider three models which have some of the characteristics that have just been presented:

- Richter's model (Richter 1981);
- Elias–Chambré model (Elias & Chambré 1984);
- a general drift flux model.

These models contain most of the above features and may be presumed to be capable of reasonable prediction of data if:

- the constitutive relations have a basis in fact;
- the assumption that a one dimensional continuous phase model is inherently not wrong for predicting critical flow.

As shall be seen, these models produce reasonable results but not necessarily statistically good results.

4.3.1. The Richter model

Richter (1981) developed a mechanistic non-equilibrium two-fluid model which uses two mass conservation, two momentum conservation and one mixture energy conservation equations. A simple flow regime map is adopted which consists of bubbly flow for void fractions of less than 0.3, annular flow for void fractions larger than 0.8 and a transition regime (called churn turbulent flow) for void fractions between 0.3 and 0.8. The governing equations are:

$$\frac{1}{W_L}\frac{dW_L}{dz} = \frac{1}{\rho_L}\frac{d\rho_L}{dz} + \frac{1}{V_L}\frac{dV_L}{dz} - \frac{1}{1-\epsilon}\frac{d\epsilon}{dz} + \frac{1}{A}\frac{dA}{dz} \quad [63]$$

$$\frac{1}{W_G}\frac{dW_G}{dz} = \frac{1}{\rho_G}\frac{d\rho_G}{dz} + \frac{1}{V_G}\frac{dV_G}{dz} + \frac{1}{\epsilon}\frac{d\epsilon}{dz} + \frac{1}{A}\frac{dA}{dz} \quad [64]$$

$$\rho_L V_L(1-\epsilon)A\frac{dV_L}{dz} = -\frac{dp}{dz}(1-\epsilon)A + \tau_{GL}A - \tau_{wL}A - \tfrac{1}{2}(V_G - V_L)\frac{dW_L}{dz} \quad [65]$$

$$\rho_G V_G \epsilon A\frac{dV_G}{dz} = -\frac{dp}{dz}\epsilon A - \tau_{GL}A - \tau_{wG}A - \tfrac{1}{2}(V_G - V_L)\frac{dW_G}{dz} \quad [66]$$

$$[(H_G - H_L) + \tfrac{1}{2}(V_G^2 - V_L^2)]\frac{dW_G}{dz} + \left(\frac{dH_G}{dz} + V_G\frac{dV_G}{dz}\right)W_G + \left(\frac{dH_L}{dz} + V_L\frac{dV_L}{dz}\right)W_L = 0 \quad [67]$$

$$\frac{6h}{d}(T_L - T_G)\epsilon A = \frac{dW_G}{dz}H_{LG} + W_G\frac{dH_G}{dz} \quad [68]$$

where τ_{GL} is the interfacial friction force, τ_{wL} and τ_{wG} are the wall friction forces on the liquid and vapor phases, respectively; d is the bubble diameter and h is the heat transfer coefficient. The last term in the momentum equations [65] and [66], represents the momentum changes due to evaporation or condensation. The right-hand side of [68] represents the evaporation and change of phase of the bubbles. Dobran (1987), has improved on the above model by replacing the second term on the right-hand side of [68] by the expression $W(V_G^2 - V_L^2)\,dx/dz$ which accounts for the change in kinetic energy during evaporation.

The dependent variables in Richter model are: p, V_G, V_L, W_G, H_L and ϵ (or d). Generally speaking, the model is specialized with respect to its constitutive relations as follows:

(1) The interfacial friction contains a spatial derivative term in the bubbly flow regime of the form

$$\tau_{GL}^{\text{bubbly}} = \frac{3}{4}\frac{C_D}{d}\epsilon(1-\epsilon)^3\rho_L(V_G - V_L)|V_G - V_L| + \frac{1}{2}\rho_L V_G \epsilon \frac{d(V_G - V_L)}{dz} \quad [69]$$

where C_D is given by $C_D = C'_D(1-\epsilon)^{4.7}$ (C'_D is the drag coefficient for solid sphere). In the annular flow region ($\epsilon > 0.8$), the interface friction force defined as

$$\tau_{GL}^{\text{annular}} = \tfrac{1}{2}C_{fi}A_{iA}\rho_G(V_G - V_L)^2 \quad [70]$$

where C_{fi} is evaluated from $C_{fi} = 0.005[1 + 75(1-\epsilon)]$ and the interfacial area, is $A_{iA} = 4\sqrt{\epsilon}/d$.

(2) Interfacial heat transfer requires a surface area and a heat transfer coefficient. In the bubbly flow regime

$$A_{iB} = N\pi d^2$$

$$h = \frac{k_i}{d}(2 + 0.6\,\mathrm{Re}^{0.5}\,\mathrm{Pr}^{0.33})$$

where h is the heat transfer coefficient and Re and Pr are Reynolds and Prandtl numbers, respectively.

In the churn-turbulent regime h is determined from a Colburn type equation

$$h = \frac{C_{fi}}{2}Cp_L\left(\frac{v_G}{v_L} - 1\right)$$

(3) The wall friction for the vapor phase, τ_{wG}, is neglected, and the Martinelli–Nelson two-phase multiplier is used to calculate the wall friction on the liquid phase.

(4) In the churn-turbulent flow regime ($0.3 < \epsilon < 0.8$), the interfacial friction is calculated by a linear interpolation with respect to the void fraction of the friction factors at $\epsilon = 0.3$ and at $\epsilon = 0.8$.

The number density of bubbles, N is chosen as $10^{11}\,\mathrm{m}^{-3}$ and the initial bubble diameter, d, at the start of homogeneous nucleation is taken as 2.5×10^{-5} m. The relation between diameter and void fraction is taken as:

$$\epsilon = N\pi d^3/6$$

According to [68] the vapor generation term may be taken as

$$\dot{\Gamma}_G = \frac{1}{H_{LG}}\left[\frac{6h}{d}\epsilon A(T_L - T_G) - G_G A\left(\frac{dH_G}{dp}\right)_s \frac{dp}{dz}\right] \quad [71]$$

There are a number of difficulties with this definition in a vertical pipe. If we take the origin of our reference frame as the start of the discharge pipe (increasing distance is downwards), then dp/dz is positive over much of the early length. Since $(dH_G/dp)_s < 0$ for $p > 500$ psia we note that it is possible for $\dot{\Gamma}_G$ to be positive and for voids to form while the liquid is subcooled (and in the absence of a wall heat flux). Indeed, in this model, high depressurization rates can suppress void formation for $p > 500$ and high pressurization rates can enhance void formation. The opposite is true for $p < 500$ which is what one would expect to be correct independently of pressure.

In practice the Richter suppresses nucleation until the liquid achieves a certain bulk superheat implied by $\Delta p > 4\sigma/d_o$ with $d_o \approx 2.5 \times 10^{-5}$ m.

This model along with Ardron's (Ardron 1978)† introduces a spatial derivative in the interface friction term. This term is assumed to arise from the apparent mass force. Although such a force does exist, its importance in these calculations is not clear because comparisons (the same calculation with and without the term) were not performed by the authors.

†Not considered here.

4.3.2. The Elias–Chambré model

The Richter model makes use of the phasic momentum equations and introduces a specific form for τ_{GL}. The model we discuss now (Elias & Chambré 1984) introduces the drift flux relation and only makes use of a mixture momentum equation.

Adding the momentum equations of the two phases one obtains in steady state

$$\frac{d(V_G G_G + V_L G_L)}{dz} + \frac{dp}{dz} + \bar{\rho} g + \tau_{wL} + \tau_{wG} = 0 \qquad [72a]$$

If the drift flux equation is explicitly introduced then this is replaced by:

$$\frac{d}{dz}\left(\frac{G^2}{\bar{\rho}}\right) + \frac{d}{dz}\left[\frac{\epsilon \rho_L \rho_G (V'_{gj})^2}{(1-\epsilon)\bar{\rho}}\right] + \frac{dp}{dz} + \bar{\rho} g + \tau_{wL} + \tau_{wG} = 0 \qquad [72b]$$

where

$$\bar{\rho} \equiv (1-\epsilon)\rho_L + \epsilon \rho_G$$

$$V'_{gj} \equiv (1-\epsilon)(V_G - V_L) \equiv \frac{\bar{\rho} V_{gj} + (C_o - 1)G}{\bar{\rho} - (C_o - 1)(\rho_L - \rho_G)\epsilon}$$

C_o is a concentration parameter which quantifies the effect of the radial distribution of the void and V_{gj} is the void weighted vapor drift velocity with respect to the center of the volume of the two-phase mixture. In this particular study it was assumed that $C_o = 1.13$ and

$$V_{gj} = 1.41\left[\frac{\sigma g(\rho_L - \rho_G)}{\rho_L^2}\right]^{1/4} \cos\theta \qquad [73]$$

where the inclination angle, θ, is measured from the vertical axes.

As in the Richter model a special set of assumptions is introduced concerning: friction factors, heat transfer coefficients, state equations, etc. The most important of these assumptions is the treatment of the vapor generation term.

Consider the growth in the superheated liquid of vapor bubbles of radius r to determine the evaporation rate term $\dot{\Gamma}_G$. The determination of r requires the simultaneous solution of the equations for the vapor pressure in the bubble, the time-dependent thermal conduction in the liquid layer surrounding the bubble and the dynamics of the bubble. A number of approximate solutions available in the literature greatly simplify the analysis. As the bubble population is averaged over the flow cross section in the following, the influence of the wall on the bubble radius history is ignored. In addition, convection heat transfer is insignificant for small bubble sizes and low relative velocity. The bubble radius is, therefore, determined by a conduction bubble growth model (Forster & Zuber 1954):

$$r = 2k\frac{\sqrt{(\lambda Cp)_L}}{H_{LG}\rho_G}(T_L - T_s)\sqrt{t}, \quad k = \sqrt{\frac{3}{\pi}} \qquad [74]$$

T_L is the temperature of the liquid surrounding the bubble, T_s is the vapor temperature taken to be at saturation and λ and Cp are the liquid conductivity and specific heat at constant pressure, respectively. In a steady temperature and pressure field [74] can be restated as:

$$\frac{dr}{dt} = \beta^2 \frac{(T_L - T_s)^2}{r}, \quad \beta = k\frac{\sqrt{(\lambda \rho c_p)_L}}{H_{LG}\rho_G} \qquad [75]$$

The principal assumption is now made that the rate law in [75] is valid also in an element of the vapor phase which travels with the speed of the vapor. Equation (75) can be stated in the Lagrangian view as

$$\frac{Dr}{Dt} = \beta^2 \frac{(T_L - T_s)^2}{r} \qquad [76]$$

where Dr/Dt denotes a substantial derivative. A new formulation is incorporated in order to arrive at the bubble species equation which yields the bubble number and their radii distribution $n(z, r)$ along the flow path. The vapor generation term was obtained by integrating the rate of change of n over the range of existing bubble radii in the flow. In this way the model accounts for the variation in both the number density and sizes of the bubbles along the channel.

The model postulates the existence of two separate families of bubbles: those introduced at the inlet and those generated along the flow path. In the end, the model has three parameters† which define the relative importance of the two families. The first, n_1, is the normalized bubble density of the first family; the second, n_o, that of the second family; and the third, ψ, is a heterogeneity coefficient which defines the rate of formation of new bubbles along the flow path. These parameters were adjusted to yield good agreement with data. The following values were used in this study:‡

$$n_1 = \begin{cases} 5 \times 10^{30} & \text{saturated and superheated vessel conditions} \\ 0 & \text{subcooled vessel conditions} \end{cases}$$

$$n_2 = 10^{28}$$

$$\psi = 10^{-8}$$

4.3.3. A general drift flux model

This model, as that of Elias & Chambré (1984), uses a drift flux model in place of the second momentum equation. The specific drift flux parameters are those developed in Chexal & Lellouche (1986), except that the directional component of gravity multiplies V_{gj} (as in [73]). Thus, for horizontal flows:

$$V_G \equiv C_o j \equiv C_o j_L/(1 - \epsilon C_o) \quad [77]$$

and the vapor generation term for superheated liquid with no wall heat flux is:

$$\dot{\Gamma}_G = -\frac{4h_E}{D_e H_{LG}}(T_s - T_L) \quad [78]$$

with

$$h_E = 0.025 \rho_L Cp_L V_G = 0.025 \, \mathrm{Pe} \, k_L S/D_e \quad [79]$$

where Pe is Peclet number, k is conductivity and D_e is the equivalent channel diameter.

The initial irreversible pressure drop (vessel to nozzle, crack, etc.) is taken as

$$\Delta p_e = K_c(G_G^\circ |V_G^\circ| + G_L^\circ |V_L^\circ|)/2\sigma'^2 \quad [80]$$

where σ' is area ratio (A_1/A_o), K_c is irreversible loss coefficient, taken from Idel'chik (1966) and G_G° and G_L° are the mass flow rates of the vapor and liquid phase, respectively.

The vapor enthalpy source term is taken as:

$$Q_G = -4h_{co}(T_G - T_L)/D_e \quad [81]$$

$$h_{co} = 360 Cp_L \rho_L k_L S|T_G - T_L|/\rho_G H_{LG} D_e = 360 JaSk_L/D_e \quad [82]$$

Except for the wall friction term which was based on relatively high velocity flow experiments in developing the phasic coefficients, the constitutive relations were developed and validated for normal flow conditions and uncovery situations. Thus, the use of this model for critical flow is in the form of a "proof test". Rather than refer to this model by the long title of this section, the shorter notation, "the GSL model", is used.

4.3.4. The RELAP5/MOD2 model

This model is described in some detail in its code manual (Ransom *et al.* 1985); it is derived from the model described by Ransom & Trapp (1980) and Trapp & Ransom (1982). The methodology breaks the choking process into one with either a two-phase inlet or a subcooled inlet; different mathematical approaches are used for each process. For two-phase flow the phases are assumed to be in thermal equilibrium. Thermal non-equilibrium is considered for subcooled upstream stagnation conditions.

(1) Two-phase inlet. Although an attempt is made to consider the choking process from the viewpoint of a full set of equations and to determine the critical characteristic applicable to the

†In addition to those in the other constitutive relations.

‡The values used are different from those used in the original publication and were optimized for the data of Sozzi & Sutherland.

onset of choking, in the end this was considered too speculative. A final choking criterion is established as:

$$\frac{\epsilon\rho_L V_G + (1-\epsilon)\rho_G V_L}{\epsilon\rho_L + (1-\epsilon)\rho_G} = \pm a_{HE} \quad [83]$$

where a_{HE} is the HEM speed of sound (see [22d]). It is important to note that the densities in [83] appear in the reverse to normal order, thus in defining $\lambda \equiv \rho_G/\rho_L$ the two-phase choking criterion can be written as:

$$\frac{G_G + \lambda^2 G_L}{F_G + \lambda^2 F_L} \equiv \frac{j_G + \lambda j_L}{\epsilon + (1-\epsilon)\lambda} = a_{HE} \quad [84]$$

At 68 bar (1000 psi), $\lambda^2 \approx 1/400$ [even at 136 bar (2000 psi) $\lambda^2 \approx 0.018$], therefore, for void fractions greater than a very few tenths this criterion is really $V_G \approx a_{HE}$ (where V_G is the code calculated value of the vapor velocity). In practice, the procedure for calculating the terms which enter [84] is not trivial since the staggered grid method used in RELAP5/MOD2 evaluates the densities and void fraction in the center of the grid but the velocities are evaluated at the junctions. As the TRAC manual explicitly states† "the cell centered values have to be upgraded to the junction to account for the steep pressure gradients expected in the neighborhood of the choking location".

(2) Subcooled inlet. For a subcooled inlet, RELAP5/MOD2 assumes that the phases are in mechanical equilibrium (no slip) and may be in thermal non-equilibrium. Thus the phasic velocities are:

$$V_L = V_G = \pm V_c$$

where V_c is a choking velocity defined by:

$$V_c = \max\{a_{HE}, [V_n^2 + 2(p_n - p_t)/\bar{\rho}_t]^{1/2}\} \quad [85]$$

Here V_n is the calculated velocity at the upstream junction, p_n is the calculated pressure at the upstream volume and the throat pressure, p_t, is defined by a modified form of the Alamgir *et al.* (1981) pressure undershoot correlation.

$$p_t = p_s - \max(\Delta p, 0)$$

$$\Delta p = 0.258 \frac{\sigma^{3/2} T_R^{13.76} (1 + 13.25\Sigma^{0.8})^{1/2}}{(1-\lambda)(k_B T_c)^{1/2}} - 0.07(A_t/A)^2(\rho V_c^2/2) \quad [86]$$

where T_R is the reduced liquid temperature, T_c is the critical temperature, Σ is the rate of depressurization and k_B is Boltzmann's constant.

It should be noted that there are a number of discrepancies between the above equations in the RELAP5/MOD2 manual and the original publications.‡

4.3.5. The TRAC-PF1/MOD1 model

The methodology used in the TRAC-PF1 model is almost identical with that in RELAP5/MOD2. The choking criterion for two-phase inlet conditions is based on the critical characteristic velocity. Assuming non-homogeneous equilibrium two-phase flow, the final result for the choking criterion appears as (Trapp & Ransom 1982):

$$\bar{V} + D(V_G - V_L) = \pm a \quad [87]$$

In [87] the coefficient D and the two-phase speed of sound, a, are complex functions of the local variables and an unknown parameter, labeled "C", which is the coefficient entering the virtual mass term. Because C is not known (nor can it be specified from experiment through a correlation), RELAP5/MOD2 discards the final result and uses the equation presented in the previous section ([83]). The TRAC procedure is to utilize the characteristic method ([87]), but the exact value of relation used for the unknown parameter C is not stated.

†The RELAP5/MOD2 manual makes no such statement.

‡None of the constants appear as they were originally published; the term Σ is defined very differently (the RELAP5/MOD2 manual has it as zero for all pipe ruptures since it defines $\Sigma \approx dA/dz|$, while Alamgir defines it as the nearly constant rate of depressurization during the rupture for that portion of the time that the liquid is superheated).

In the subcooled blowdown phase the choking criterion stated in [85] is used with $p_t = p_s$, i.e. thermal non-equilibrium at the throat is not considered. It is recognized, however, that a nucleation delay model is required to analyze fast transients in which the throat pressure may be much lower than the saturation pressure corresponding to the liquid temperature at the junction.

As with the RELAP5/MOD2 model, one cannot directly utilize this model in a stand-alone fashion but should examine it in the context of the rest of the TRAC-PF1/MOD1 model.

5. EXPERIMENTAL DATA SOURCES

Over the last 40 or so years, a large number of critical flow experiments have been performed. An interesting listing of some 50 or so references may be found in the NEA report (Britain *et al.* 1982). Much of these data were examined by Ilic *et al.* (1986) in the preparation of a qualified critical flow database for EPRI. Two major sources of data not considered by Ilic *et al.* (1986) and, of course, those published since, are Marviken (1982) and Lee & Swinerton (1983). The first source provides very large diameter downflow data; the second source provides data in the same geometries from 34 to 170 bar (500 to 4500 psia) (well supecritical). The Lee & Swinerton (1983) data are not considered in the present work.

The Marviken facility was used for full-scale critical flow tests between mid-1977 and December 1979. Twenty-seven tests were conducted by a downward discharge of water and steam mixtures from a full-sized reactor vessel through a large diameter vertical discharge pipe that supplied the flow to a test nozzle. Nine nozzles were tested; all had rounded entrances followed by a nominal 20, 30 or 50 cm constant diameter straight section. Table 4 shows some of the details of the various test nozzles. The discharge pipe that connects the vessel to the nozzle is 6283 mm long and is geometrically complex. It is made up of several pieces: a nozzle, permanently attached to the vessel with a 752 mm dia, a 1980 mm long drift tube of the same diameter, a 1778 mm long globe valve with a 780 mm dia and a 1000 mm 752 mm dia section to which the nozzle is attached. Besides these there were two 120 mm long instrument rings inserted on either end of the 1980 mm drift tube. It is quite clear that, with this degree of geometric complexity, the question of establishing a consistent set of complete inlet conditions is not simple.

The Marviken tests considered in this work are those numbered 04, 06, 09, 13, 14, 18, 19, 23 and 24; they cover five of the nine nozzles and most of the length range as well.

5.1. Qualification of Data

In practice, the word "qualified" means whatever the user chooses it to mean. Thus, in the Ilic *et al.* (1986), the word means that the original data sources can be used directly, i.e. the data were tabular and not in graphical or analog forms. The best that Ilic did was to indicate that certain sets of data might be suspect for one or another reason. Nevertheless, clearly unacceptable data were included. Because of the accessibility of this compilation, it has been made the primary source for this review, that is, the winnowing already completed was accepted but many of the primary sources have been re-examined as well.

Sixty-six data sets were considered in this work and then reduced to 42. This process of elimination may be considered a form of disqualification. The data sources that have utility in this chapter are those which have some relationship to the geometries that might be found in practice

Table 4. Marviken test nozzles

Nozzle No.	Diameter (mm)	Length (mm)	Used in test No.
1	200	590	13, 14
2	300	290	6, 7
3	300	511	25, 26
4	300	895	1, 2, 12
5	300	1116	17, 18, 19
6	500	166	23, 24
7	500	730	20, 21, 22, 27
8	500	1809	15, 16
9	509	1589	3, 4, 5, 8, 9, 10, 11

during normal operation or during an accident in light water reactors. Thus, rectangular, annular and De Laval nozzles and other converging–diverging geometries generally are not of great interest although the Boivin and Sozzi–Sutherland nozzle 1 are kept. In addition to this "geometric" bias, all data were discarded where it was believed that the inlet (i.e. stagnation) conditions are suspect. Thus data where throat conditions rather than inlet conditions are given, are not acceptable; neither are those experiments where mixing of separate steam/water sources takes place just before that inlet, i.e. where "complete" mixing cannot be assumed.

Based on an early reading of Ilic we discarded one of his 19 primary sources (Fauske 1962) because no stagnation (upstream) conditions were published. The resulting data sets (listed in table 5) were put into consistent form by estimating all missing stagnation conditions (p_0 but not H_0 given or vice versa) and the simple models were used to predict all these data sets. The results of this first selection can be seen in figures 5 and 6 where the prediction of these data is shown using the HEM and Moody slip models.

Although "completing" the data sets by estimating the missing stagnation conditions was considered to be possible, further consideration led to the following conclusions:

- many of the data sources cannot be qualified in any sense of the meaning of the word;
- a fair percentage of the data listed in Ilic *et al.* (1986) is miscopied from the original sources [all of the Ardron (1978) and Boivin (1979) enthalpy data are incorrect];
- the data are converted to a consistent set of units, thus altering the number of significant figures (from two to seven in some cases);
- the conversion factors (e.g. psia→kPa) are not listed and use of the ASME 4th Edn conversion factors to recover the original data does not reproduce those data.

Therefore, although the Ilic report was used, the data were reproofed, and many of the sources were discarded as not being usable. Of the 19 original sources (some 60 plus separate geometries), nine sources (some 42 separate geometries) are left (see table 6). The reasons for removal of these sources are related to significant uncertainties in stagnation conditions or because the geometry was not considered appropriate.

A major problem in dealing with secondary (compiled) data sources lies in the compilers' penchant for changing the set of units that the experimenter used in reporting his data into some other set, currently SI. Thus, most experimenters have reported temperature and pressure but the Ilic compilation converted temperature to enthalpy. This conversion can be significant when the temperatures are very near saturation because different researchers use different algebraic formulations for the thermodynamic properties. Indeed, at lower pressures, 0.3°C can be worth 30% in critical flow in the neighborhood of saturation.

It should not be presumed that it is believed that the stagnation conditions of the sources in table 6 are accurately reported; there was no reason to reject them. Neither should it be thought that the removed cases are better or worse when they are compared to prediction. Tables 7–10 show a statistical comparison with the 66 geometries of table 5 using several of the simpler models. The deleted sources (geometries 3, 14, 15–17, 22–30, 33–37, 41 and 42) contain some of the best fits to data as well as some poor fits; and Bryer (1966) data (cases 2, 4–10), which are not discarded, contain some of the worst fits to data.

Because of the time costs of computing these 42 geometries, only three sources and 20 geometries are used with the space-dependent models. These are listed in table 11 and comprise the Ardron & Ackerman (1978), Boivin (1979) and Sozzi & Sutherland (1975) sources. All the 63 cases listed in table 6 are used with the analytic and fitting models.

In using space-dependent models it was preferred to deal with square inlet conditions or smooth inlets with large r/D in order to avoid having to choose a contraction unrecoverable loss coefficient other than 1/2 or 0.0. The reason for this "bias" is that the task is to attempt to qualify critical flow models rather than fit loss coefficients. Most of the space-dependent models can be brought into much better agreement by "adjusting" either the loss coefficient or the wall roughness. A consistent wall roughness of 4×10^{-5} mm (1.3×10^{-6} ft) has been used in all calculations when a roughness is required (only in the "general drift flux model" studies).

Table 5. Selected critical flow data from the Ilic compilation

Case	Reference	L (mm)	D (mm)	$\cos\theta$	N-data	Comments
1	Ardron & Ackerman (1978)	1015	26.3	0.0	31	
2	Bryers & Hsieh (1966)	152	38	0.0	5	rounded entrance 6.35 mm
3	Bryers & Hsieh (1966)	533.4	50.8	1.0	4	rec. duct 76.2 × 38.1 mm
4	Bryers & Hsieh (1966)	305	38	0.0	6	rounded entrance 6.35 mm
5	Bryers & Hsieh (1966)	152	51	0.0	6	rounded entrance 6.35 mm
6	Bryers & Hsieh (1966)	305	51	0.0	5	rounded entrance 6.35 mm
7	Bryers & Hsieh (1966)	406	51	0.0	6	rounded entrance 6.35 mm
8	Bryers & Hsieh (1966)	305	76	0.0	5	rounded entrance 6.35 mm
9	Bryers & Hsieh (1966)	610	76	0.0	6	rounded entrance 6.35 mm
10	Bryers & Hsieh (1966)	406	51	0.0	4	rounded entrance 6.35 mm
11	Bryers & Hsieh (1966)	533	51	0.0	6	rounded entrance 6.35 mm
12	Boivin (1979)	500	12	0.0	10	$D = 50$ $(z < 0)$; $0 < z < 50$ rounded entrance; $D = 12$ $(50 < z < 500)$; $D = 12 + 19$ $(z - 500)$, $(z < 700)$; $D = 50$ $(z > 700$ mm)
13	Boivin (1979)	1600	30	0.0	5	$D = 150$ $(z < 0)$; $0 < z < 130$ rounded entrance; $D = 30$ $(130 < z < 1730)$; $D = 30 + 0.12$ $(z - 1730)$, $(z < 2305)$; $D = 100$ $(z > 2305$ mm)
14	Boivin (1979)	1700	50	0.0	6	$D = 150$ $(z < 0)$; $0 < z < 130$ rounded entrance; $D = 50$ $(130 < z < 1830)$; $D = 50 + 0.12$ $(z - 1830)$, $(z < 2240)$; $D = 100$ $(z > 2240$ mm)
15	Cruver (1963)	660	13	0.0	33	horizontal tube
16	Danforth (1941)	13	32	−1.0	6	rounded entrance 4.76 mm; $D = 19.05$ $(3.175 < z < 9.525$ mm)
17	Danforth (1941)	13	32	−1.0	9	rounded entrance 4.76 mm; $D = 19.05$ $(3.175 < z < 9.525$ mm)
18	Finke & Collins (1981)	13	44	0.0	92	$D = 18.28$ $(54.7 < z < 79.7)$; $D = 18.28 + 0.12$ $(z - 79.7)$, $(z < 215.9)$; $D = 34.9$ $(z > 215.9$ mm)
19	Guizovarn *et al.* (1975)	2674	14	1.0	13	$D = 14$ $(z < 2674)$; $D = 14 + 0.12$ $(z - 2674)$, $(z < 2928)$; $D = 45$ $(z > 3209)$; $D = 45 + (z - 3209)/6$, $(z < 3239)$; $D = 50 + 0.14$ $(z - 3389)/6$, $(z < 3700$ mm)
20	Guizovarn *et al.* (1975)	2674	14	1.0	24	$D = 29.5$ $(z < 2230)$; $D = 29.5 + 0.12$ $(z - 2230)$, $(z < 2360)$; $D = 14$ $(z < 2674)$ $D = 45 + (z - 3209)/6$, $(z < 3239)$; $D = 50 + 0.14$ $(z - 3389)$, $(z < 3700$ mm);
21	Henry (1968)	914	5.8	0.0	35	duct width = 23.6 mm height = 3.3 $(0 < z < 914.4)$; $H = 3.3 + 0.12$ $(z - 914.4)$, $(z < 1066.8)$
22	Henry (1968)	914	8	0.0	26	$D = 7.95$ $(0 < z < 914.4$ mm); $D = 7.95 + 3.46$ $(z - 914.4)$, $(z < 926.77)$
23	Henry (1968)	914	8	0.0	71	$D = 7.95$ $(0 < z < 914.4$ mm); $D = 7.95 + 0.12$ $(z - 914.4)$, $(z < 1160.45)$
24	Henry (1968)	914	8	0.0	80	$D = 7.95$ $(0 < z < 914.4$ mm); $D = 7.95 + 3.46$ $(z - 914.4)$, $(z < 926.77)$
25	Isbin *et al.* (1957)	609	26	0.0	10	1 in. full bore
26	Isbin *et al.* (1957)	609	21	0.0	8	1 in. full bore
27	Isbin *et al.* (1957)	609	16	0.0	31	1 in. full bore
28	Isbin *et al.* (1957)	609	10	0.0	47	1 in. full bore
29	Isbin *et al.* (1957)	609	13	0.0	10	1 in. full bore
30	Isbin *et al.* (1957)	609	7	0.0	11	1 in. full bore
31	Jeandey *et al.* (1981)	463	20	1.0	15	$D = 66.7 - 0.54z$ $(0 < z < 86.9)$; $D = 20.1$ $(z > 86.9$ mm)

continued opposite

Table 5—*continued*

Case	Reference	L (mm)	D (mm)	$\cos\theta$	N-data	Comments
32	Jeandey *et al.* (1981)	463	20	1.0	73	see source for $z < 100$ mm; $D = 20.13$ $(100 < z < 463)$; $D = 20.13 + 0.12$ $(z - 463)$, $(z < 900)$; $D = 737$ $(z > 900$ mm)
33	Morrison (1977)	197	28	0.0	7	round inlet $(0 < z < 63.5)$; $D = 27.94$ $(z < 196.85$ mm)
34	Morrison (1977)	64	28	0.0	5	round inlet $(0 < z < 63.5)$; $D = 27.94 + 0.175$ $(z - 63.5)$ $(z < 228.6$ mm)
35	Neusen (1962)	0	11	0.0	25	$D = 11.12$ mm at throat; $D = 11.12 + 0.425z$ $(0 < z < 35.91$ mm)
36	Neusen (1962)	0	6	0.0	12	$D = 6.4$ mm at throat; $D = 6.4 + 0.425z$ $(0 < z < 59.81$ mm)
37	Ogasawara (1969)	100	11	0.0	12	$D = 125$ mm at throat $(z = 100)$; $D = 10.9$ $(100 < z < 1400$ mm)
38	Reocreux (1974)	2335	20	1.0	28	$D = 20$ $(0 < z < 2335)$; $D = 20 + 0.12$ $(z - 2335)$, $(z < 2662$ mm)
39	Seynhaeve (1980)	306	13	1.0	26	$D = 12.5$ $(0 < z < 306)$; $D = 12.5 + 0.245$ $(z - 306)$, $(z < 541)$ $D = 70$ $(z > 541$ mm)
40	Seynhaeve (1980)	306	13	1.0	31	$D = 12.5$ $(0 < z < 221)$; $D = 12.5 + 0.245$ $(z - 221)$, $(z < 541)$ $D = 70$ $(z > 541$ mm)
41	Schrock *et al.* (1977)	340	6	−1.0	10	$D = 63.5 - 1.68z$ $(0 < z < 34)$; $D = 6.4 + 0.425$ $(z - 34)$, $(z < 93.8$ mm)
42	Schrock *et al.* (1977)	35	4	−1.0	27	$D = 63.5 - 1.68z$ $(0 < z < 35.5)$; $D = 3.96 + 0.425$ $(z - 35.5)$ $(z < 86.3$ mm)
43	Sozzi & Sutherland (1975)	45	12.7	0.0	129	$D = 43.2$ $(z = 0)$; rounded convergent $(0 < z < 44.5)$; $D = 12.7 + 0.105$ $(z - 44.5)$, $(z < 158.5$ mm)
44	Sozzi & Sutherland (1975)	45	12.7	0.0	13	$D = 43.2$ $(z = 0)$; rounded convergent $(0 < z < 44.5$ mm)
45	Sozzi & Sutherland (1975)	57	12.7	0.0	47	$D = 43.2$ $(z = 0)$; rounded convergent $(0 < z < 44.5$ mm)
46	Sozzi & Sutherland (1975)	362	12.7	0.0	19	$D = 43.2$ $(z = 0)$; rounded convergent $(0 < z < 44.5$ mm)
47	Sozzi & Sutherland (1975)	83	12.7	0.0	17	$D = 43.2$ $(z = 0)$; rounded convergent $(0 < z < 44.5$ mm)
48	Sozzi & Sutherland (1975)	553	12.7	0.0	13	$D = 43.2$ $(z = 0)$; rounded convergent $(0 < z < 44.5$ mm)
49	Sozzi & Sutherland (1975)	108	12.7	0.0	23	$D = 43.2$ $(z = 0)$; rounded convergent $(0 < z < 44.5$ mm)
50	Sozzi & Sutherland (1975)	679	12.7	0.0	96	$D = 43.2$ $(z = 0)$; rounded convergent $(0 < z < 44.5$ mm)
51	Sozzi & Sutherland (1975)	159	12.7	0.0	15	$D = 43.2$ $(z = 0)$; rounded convergent $(0 < z < 44.5$ mm)
52	Sozzi & Sutherland (1975)	1823	12.7	0.0	81	$D = 43.2$ $(z = 0)$; rounded convergent $(0 < z < 44.5$ mm)
53	Sozzi & Sutherland (1975)	235	12.7	0.0	12	$D = 43.2$ $(z = 0)$; rounded convergent $(0 < z < 44.5$ mm)
54	Sozzi & Sutherland (1975)	273	12.7	0.0	22	$D = 43.2$ $(z = 0)$; rounded convergent $(0 < z < 44.5$ mm)
55	Sozzi & Sutherland (1975)	5	12.7	0.0	58	Nozzle No. 3
56	Sozzi & Sutherland (1975)	322	12.7	0.0	24	Nozzle No. 3
57	Sozzi & Sutherland (1975)	513	12.7	0.0	24	Nozzle No. 3
58	Sozzi & Sutherland (1975)	640	12.7	0.0	17	Nozzle No. 3
59	Sozzi & Sutherland (1975)	195	12.7	0.0	23	Nozzle No. 3
60	Sozzi & Sutherland (1975)	45	19	0.0	23	$D = 43.2$ $(z = 0)$; rounded elliptical sec. $(0 < z < 44.5$ mm)
61	Sozzi & Sutherland (1975)	732	54	0.0	4	$D = 260 - 0.39$ $(z - 202)$, $(202 < z < 732)$; $D = 54 + 0.263$ $(z - 732)$, $(z < 1112$ mm)
62	Sozzi & Sutherland (1975)	696	76	0.0	3	$D = 260 - 0.39$ $(z - 223)$, $(223 < z < 696)$; $D = 76.5 + 0.263$ $(z - 696)$, $(z < 1076$ mm)
63	Sozzi & Sutherland (1975)	63	28	0.0	5	$D = 72.6$ $(z = 0)$; rounded elliptical sec. $(0 < z < 63.5$ mm); $D = 28 + 0.246$ $(z - 63.5)$, $(z < 228.5$ mm)
64	Zaloudek (1961)	609.5	13	0.0	16	round tube
65	Zaloudek (1961)	914.4	13	0.0	45	round tube
66	Zaloudek (1961)	609.5	13	0.0	13	round tube

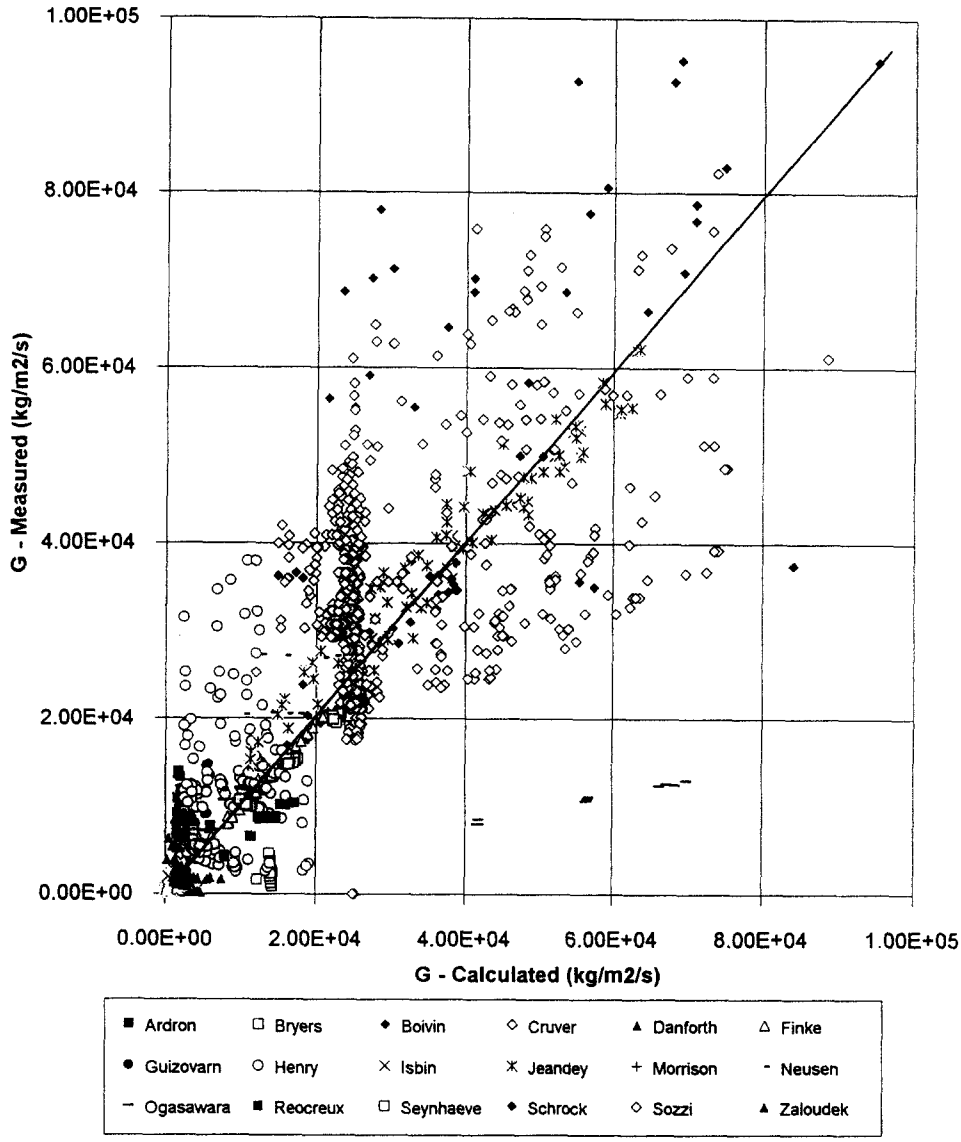

Figure 5. Measured vs predicted critical mass flux using the homogeneous equilibrium model (HEM).

5.2. *Data Uncertainties*

In normal circumstances uncertainties of 0.01 bar ($\approx$0.2 psia) or 0.1°C ($\approx$0.2°F) in inlet conditions would not be considered significant. However, although the uncertainties in the current data are typically small fractions of the absolute values, the dependence of the critical flow magnitude on subcooling is so large near saturation at low pressures that even a few tenths of a degree or hundredths of a bar can be worth 10–30% in flow; these effects become less important farther away from saturation. The criterion for importance is that the temperature uncertainty, whether induced by pressure or enthalpy uncertainties, divided by the nominal subcooling, ΔT, must be significant (>0.1). Only Ardron & Ackerman (1978) presented estimates of inlet uncertainties and these estimates were used to determine the spread in predictions using the GSL model (see below).

These considerations lead to questions about the reported inlet conditions. Unfortunately, it is not possible to determine the accuracy of these reported conditions. The uncertainties, as reported by Ardron & Ackerman (1978), are extremely small and reflect only signal noise effects. Absolute errors may be larger but no firm estimates can be made. A change upwards of 0.1 bar will be more than enough to bring all GSL model calculations into exact agreement for the Ardron & Ackerman

(1978) experiments (all inlet pressures < 3.7 bars); an examination of the reported data indicates absolute reliabilities probably exclude 0.1 bar errors (accomplished by examining paired calculations with equal reported inlet subcooling) but not with high confidence.

Although arguments can be made with respect to the data that absolute errors of $\pm$ 1/2 to 2% are not unreasonable and even likely, such potential "errors" are not considered as a means to quantify and qualify models except for using the Ardron & Ackerman (1978) data as an example. All data points of those sources which are "accepted" are treated equally with the exception of two of the data points measured by Sozzi & Sutherland (1975) which are discarded because the original data source is not readable (Ilic chose to fill in the missing digits but the result is clearly in error).

5.2.1. Uncertainties in Marviken data inlet conditions

As could be expected for a large-scale experiment such as Marviken there was extensive and redundant instrumentation. Even so it is not easy to pick a set of consistent measurements which can be used to define a set of inlet stagnation conditions. This is particularly true during the early single-phase portion of the blowdowns (certainly for $t < 10$ s). At the bottom of the vessel the 20:1 averaged pressures jump up and down instead of going down smoothly (pressure sensor M106),

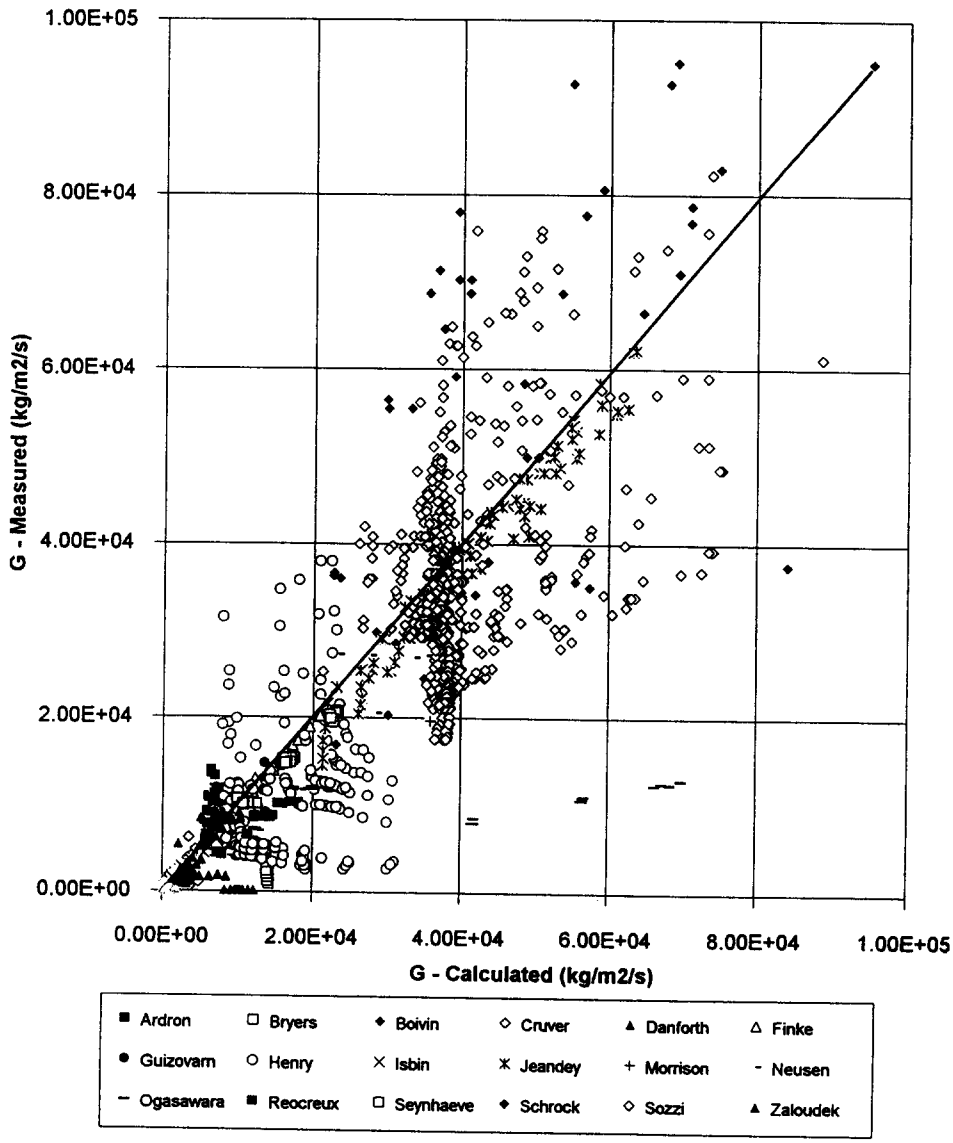

Figure 6. Measured vs predicted critical mass flux using the Moody model with slip.

Table 6. Most qualified critical flow data from the Ilic compilation

Case	Reference	L (mm)	D (mm)	$\cos\theta$	N-data	Comments
1	Ardron & Ackerman (1978)	1015	26.3	0.0	31	
2	Bryers & Hsieh (1966)	152	38	0.0	5	rounded entrance 6.35 mm
4	Bryers & Hsieh (1966)	305	38	0.0	6	rounded entrance 6.35 mm
5	Bryers & Hsieh (1966)	152	51	0.0	6	rounded entrance 6.35 mm
6	Bryers & Hsieh (1966)	305	51	0.0	5	rounded entrance 6.35 mm
7	Bryers & Hsieh (1966)	406	51	0.0	6	rounded entrance 6.35 mm
8	Bryers & Hsieh (1966)	305	76	0.0	5	rounded entrance 6.35 mm
9	Bryers & Hsieh (1966)	610	76	0.0	6	rounded entrance 6.35 mm
10	Bryers & Hsieh (1966)	406	51	0.0	4	rounded entrance 6.35 mm
11	Bryers & Hsieh (1966)	533	51	0.0	6	rounded entrance 6.35 mm
12	Boivin (1979)	500	12	0.0	10	$D = 50$ $(z < 0)$; $0 < z < 50$ rounded entrance; $D = 12$ $(50 < z < 500)$; $D = 12 + 19$ $(z - 500)$, $(z < 700)$; $D = 50$ $(z > 700$ mm)
13	Boivin (1979)	1600	30	0.0	5	$D = 150$ $(z < 0)$; $0 < z < 130$ rounded entrance; $D = 30$ $(130 < z < 1730)$; $D = 30 + 0.12$ $(z - 1730)$, $(z < 2305)$; $D = 100$ $(z > 2305$ mm)
14	Boivin (1979)	1700	50	0.0	6	$D = 150$ $(z < 0)$; $0 < z < 130$ rounded entrance; $D = 50$ $(130 < z < 1830)$; $D = 50 + 0.12$ $(z - 1830)$, $(z < 2240)$; $D = 100$ $(z > 2240$ mm)
18	Finke & Collins (1981)	13	44	0.0	92	$D = 18.28$ $(54.7 < z < 79.7)$; $D = 18.28 + 0.12$ $(z - 79.7)$, $(z < 215.9)$; $D = 34.9$ $(z > 215.9$ mm)
19	Guizovarn *et al.* (1975)	2674	14	1.0	13	$D = 14$ $(z < 2674)$; $D = 14 + 0.12$ $(z - 2674)$, $(z < 2928)$; $D = 45$ $(z > 3209)$ $D = 45 + (z - 3209)/6$, $(z < 3239)$; $D = 50 + 0.14$ $(z - 3389)/6$, $(z < 3700$ mm)
20	Guizovarn *et al.* (1975)	2674	14	1.0	24	$D = 29.5$ $(z < 2230)$; $D = 29.5 + 0.12$ $(z - 2230)$, $(z < 2360)$; $D = 14$ $(z < 2674)$ $D = 45 + (z - 3209)/6$, $(z < 3239)$; $D = 50 + 0.14$ $(z - 3389)$, $(z < 3700$ mm)
31	Jeandey *et al.* (1981)	463	20	1.0	15	$D = 66.7 - 0.54z$ $(0 < z < 86.9)$; $D = 20.1$ $(z > 86.9$ mm)
32	Jeandey *et al.* (1981)	463	20	1.0	73	see source for $z < 100$ mm; $D = 20.13$ $(100 < z < 463)$; $D = 20.13 + 0.12$ $(z - 463)$, $(z < 900)$; $D = 737$ $(z > 900$ mm)
38	Reocreux (1974)	2335	20	1.0	28	$D = 20$ $(0 < z < 2335)$; $D = 20 + 0.12$ $(z - 2335)$, $(z < 2662$ mm)
39	Seynhaeve (1980)	306	13	1.0	26	$D = 12.5$ $(0 < z < 306)$; $D = 12.5 + 0.245$ $(z - 306)$, $(z < 541)$ $D = 70$ $(z > 541$ mm)
40	Seynhaeve (1980)	306	13	1.0	31	$D = 12.5$ $(0 < z < 221)$; $D = 12.5 + 0.245$ $(z - 221)$, $(z < 541)$ $D = 70$ $(z > 541$ mm)
43	Sozzi & Sutherland (1975)	45	12.7	0.0	129	$D = 43.2$ $(z = 0)$; rounded convergent $(0 < z < 44.5)$; $D = 12.7 + 0.105$ $(z - 44.5)$, $(z < 158.5$ mm)
44	Sozzi & Sutherland (1975)	45	12.7	0.0	13	$D = 43.2$ $(z = 0)$; rounded convergent $(0 < z < 44.5$ mm)
45	Sozzi & Sutherland (1975)	57	12.7	0.0	47	$D = 43.2$ $(z = 0)$; rounded convergent $(0 < z < 44.5$ mm)
46	Sozzi & Sutherland (1975)	362	12.7	0.0	19	$D = 43.2$ $(z = 0)$; rounded convergent $(0 < z < 44.5$ mm)
47	Sozzi & Sutherland (1975)	83	12.7	0.0	17	$D = 43.2$ $(z = 0)$; rounded convergent $(0 < z < 44.5$ mm)
48	Sozzi & Sutherland (1975)	553	12.7	0.0	13	$D = 43.2$ $(z = 0)$; rounded convergent $(0 < z < 44.5$ mm)
49	Sozzi & Sutherland (1975)	108	12.7	0.0	23	$D = 43.2$ $(z = 0)$; rounded convergent $(0 < z < 44.5$ mm)

continued opposite

Table 6—*continued*

Case	Reference	L (mm)	D (mm)	$\cos\theta$	N-data	Comments
50	Sozzi & Sutherland (1975)	679	12.7	0.0	96	$D = 43.2$ ($z = 0$); rounded convergent ($0 < z < 44.5$ mm)
51	Sozzi & Sutherland (1975)	159	12.7	0.0	15	$D = 43.2$ ($z = 0$); rounded convergent ($0 < z < 44.5$ mm)
52	Sozzi & Sutherland (1975)	1823	12.7	0.0	81	$D = 43.2$ ($z = 0$); rounded convergent ($0 < z < 44.5$ mm)
53	Sozzi & Sutherland (1975)	235	12.7	0.0	12	$D = 43.2$ ($z = 0$); rounded convergent ($0 < z < 44.5$ mm)
54	Sozzi & Sutherland (1975)	273	12.7	0.0	22	$D = 43.2$ ($z = 0$); rounded convergent ($0 < z < 44.5$ mm)
55	Sozzi & Sutherland (1975)	5	12.7	0.0	58	Nozzle No. 3
56	Sozzi & Sutherland (1975)	322	12.7	0.0	24	Nozzle No. 3
57	Sozzi & Sutherland (1975)	513	12.7	0.0	24	Nozzle No. 3
58	Sozzi & Sutherland (1975)	640	12.7	0.0	17	Nozzle No. 3
59	Sozzi & Sutherland (1975)	195	12.7	0.0	23	Nozzle No. 3
60	Sozzi & Sutherland (1975)	45	19	0.0	23	$D = 43.2$ ($z = 0$); rounded elliptical sec. ($0 < z < 44.5$ mm)
61	Sozzi & Sutherland (1975)	732	54	0.0	4	$D = 260 - 0.39$ ($z - 202$), ($202 < z < 732$); $D = 54 + 0.263$ ($z - 732$), ($z < 1112$ mm)
62	Sozzi & Sutherland (1975)	696	76	0.0	3	$D = 260 - 0.39$ ($z - 223$), ($223 < z < 696$); $D = 76.5 + 0.263$ ($z - 696$), ($z < 1076$ mm)
63	Sozzi & Sutherland (1975)	63	28	0.0	5	$D = 72.6$ ($z = 0$); rounded elliptical sec. ($0 < z < 63.5$ mm); $D = 28 + 0.246$ ($z - 63.5$), ($z < 228.5$ mm)

and the 50:1 averaged temperatures (sensors M521 and M402) do so also. As long as the fluid is substantially subcooled this type of behavior is not a great difficulty; but when the fluid is essentially saturated, small discrepancies can change the inlet condition from subcooled to two-phase and back again. This can give a computer code a bad case of the dithers. Conditions are not particularly better at the entrance to the nozzle. The pressure sensor M109 (0.7 m above the nozzle using 20:1 averaging) shows $\pm 20\%$ jumps in pressure over 0.1 s during the first second and $\pm 5\%$ jumps in 0.5 s during the next 2–3 s. Because of these considerations, none of the data from the first 5 s is used.

It should be pointed out that a great deal of care was taken by the Markiven staff to reasonably establish stagnation conditions at the entrance to the discharge tube and to the nozzle. For some tests the problems we have alluded to are less important than for others but they are never simple. For example, the following quote from volume 1, section 8.1.2, is presented:

> "..., the instrumentation used to evaluate the nozzle inlet conditions was situated between 2.8 and 7.6 m from the nozzle inlet. Consequently, a number of factors must be considered when defining the true nozzle inlet conditions".

Except for the TRAC-PF1/MOD1 calculations, the discharge pipe inlet conditons specified by pressure sensor M106, and temperature sensor M402, are taken. The TRAC-PF1 conditions will be discussed when the TRAC-PF1 results are considered.

5.2.2. Effects of uncertainties

This brief section presents the effects of inlet uncertainties on predicting critical flow. As discussed in section 5.2, only the Ardron & Ackerman (1978) (A&A) data presented estimates of all inlet/outlet uncertainties. The GSL model has been chosen for this investigation.

The A&A experiments (except one which was not used) all have subcooled inlet conditions. Table 12 shows the inlet conditions and the measured and calculated flow conditions. The two subcoolings (runs 24 and 26) which contain two decimal places are as A&A reported them. The reported uncertainties are given in table 13(a); in table 13(b) are shown the repeatability uncertainties for a series of runs during which an attempt was made to keep the critical flow rate at 8000 kg/m^2 s. Table 14 shows the mean and standard deviation for all the cases yet to be

Table 7. Predictions of all the data in table 5 using the fit to the Moody model

Case	L (mm)	D (mm)	$\cos\theta$	N-data	Mean $\left\langle \frac{G_m - G_c}{G_m} \right\rangle$	SD $\left\langle \left(\frac{G_m - G_c}{G_m} \right)^2 \right\rangle$
1	1015	26.3	0.0	31	0.230	0.238
2	152	38	0.0	5	−4.882	3.191
3	533.4	50.8	1.0	4	−5.942	3.222
4	305	38	0.0	6	−4.985	3.626
5	152	51	0.0	6	−4.010	2.396
6	305	51	0.0	5	−6.352	4.723
7	406	51	0.0	6	−5.810	4.383
8	305	76	0.0	5	−6.872	4.517
9	610	76	0.0	6	−6.494	4.970
10	406	51	0.0	4	−4.578	2.285
11	533	51	0.0	6	−8.589	7.374
12	500	12	0.0	10	−0.170	0.161
13	1600	30	0.0	5	−0.389	0.128
14	1700	50	0.0	6	−0.001	0.126
15	660	13	0.0	33	−1.125	1.415
16	13	32	−1.0	6	−63.01	3.725
17	13	32	−1.0	9	−65.15	9.667
18	13	44	0.0	92	−0.280	0.395
19	2674	14	1.0	13	0.265	0.170
20	2674	14	1.0	24	−0.175	0.239
21	914	5.8	0.0	35	−0.028	0.310
22	914	8	0.0	26	−1.318	1.539
23	914	8	0.0	71	−2.593	2.509
24	914	8	0.0	80	−0.585	0.662
25	609	26	0.0	10	−2.860	2.137
26	609	21	0.0	8	−1.131	1.671
27	609	16	0.0	31	−0.716	1.215
28	609	10	0.0	47	−0.259	0.752
29	609	13	0.0	10	−1.132	1.665
30	609	7	0.0	11	−0.469	1.089
31	463	20	1.0	15	−0.014	0.132
32	463	20	1.0	73	−0.014	0.165
33	197	28	0.0	7	−0.376	0.332
34	64	28	0.0	5	−0.174	0.228
35	0	11	0.0	25	−0.646	0.107
36	0	6	0.0	12	−0.311	0.243
37	100	11	0.0	12	−5.155	1.795
38	2335	20	1.0	28	−0.498	0.248
39	306	13	1.0	26	−0.024	0.128
40	306	13	1.0	31	−0.026	0.109
41	340	6	−1.0	10	0.226	0.158
42	35	4	−1.0	27	0.341	0.256
43	45	12.7	0.0	129	0.092	0.189
44	45	12.7	0.0	13	0.246	0.126
45	57	12.7	0.0	47	0.093	0.189
46	362	12.7	0.0	19	−0.383	0.246
47	83	12.7	0.0	17	0.025	0.205
48	553	12.7	0.0	13	−0.449	0.260
49	108	12.7	0.0	23	−0.135	0.198
50	679	12.7	0.0	96	−0.512	0.255
51	159	12.7	0.0	15	−0.190	0.196
52	1823	12.7	0.0	81	−0.761	0.304
53	235	12.7	0.0	12	−0.301	0.206
54	273	12.7	0.0	22	−0.405	0.154
55	5	12.7	0.0	58	0.124	0.092
56	322	12.7	0.0	24	−0.585	0.161
57	513	12.7	0.0	24	−0.615	0.190
58	640	12.7	0.0	17	−0.694	0.203
59	195	12.7	0.0	23	−0.410	0.203
60	45	19	0.0	23	−0.111	0.120
61	732	54	0.0	4	−0.347	0.027
62	696	76	0.0	3	−0.483	0.036
63	63	28	0.0	5	−0.054	0.161
64	609.5	13	0.0	16	−0.012	0.250
65	914.4	13	0.0	45	−0.443	0.955
66	609.5	13	0.0	13	−0.810	0.891

Table 8. Predictions of all the data in table 5 using the fit to the isenthalpic model

Case	L (mm)	D (mm)	$\cos\theta$	N-data	Mean $\left\langle \frac{G_m - G_c}{G_m} \right\rangle$	SD $\left\langle \left(\frac{G_m - G_c}{G_m} \right)^2 \right\rangle$
1	1015	26.3	0.0	31	0.391	0.136
2	152	38	0.0	5	−5.144	1.563
3	533.4	50.8	1.0	4	−7.393	3.305
4	305	38	0.0	6	−5.329	2.180
5	152	51	0.0	6	−4.711	1.917
6	305	51	0.0	5	−6.431	2.263
7	406	51	0.0	6	−6.086	2.459
8	305	76	0.0	5	−7.156	2.064
9	610	76	0.0	6	−6.743	2.610
10	406	51	0.0	4	−5.738	2.255
11	533	51	0.0	6	−8.833	4.625
12	500	12	0.0	10	−0.418	0.634
13	1600	30	0.0	5	−0.167	0.241
14	1700	50	0.0	6	0.088	0.073
15	660	13	0.0	33	200.8	198.0
16	13	32	−1.0	6	6759.0	729.4
17	13	32	−1.0	9	7181.0	542.8
18	13	44	0.0	92	−0.105	0.049
19	2674	14	1.0	13	84.45	72.14
20	2674	14	1.0	24	91.16	69.95
21	914	5.8	0.0	35	103.6	88.75
22	914	8	0.0	26	55.54	79.26
23	914	8	0.0	71	32.99	77.68
24	914	8	0.0	80	0.185	0.359
25	609	26	0.0	10	956.6	280.9
26	609	21	0.0	8	773.2	598.9
27	609	16	0.0	31	694.8	456.9
28	609	10	0.0	47	863.2	769.2
29	609	13	0.0	10	733.2	499.4
30	609	7	0.0	11	651.1	256.8
31	463	20	1.0	15	−0.022	0.079
32	463	20	1.0	73	0.098	0.115
33	197	28	0.0	7	0.112	0.209
34	64	28	0.0	5	0.230	0.150
35	0	11	0.0	25	0.170	0.075
36	0	6	0.0	12	0.263	0.149
37	100	11	0.0	12	−4.300	0.170
38	2335	20	1.0	28	−0.777	0.196
39	306	13	1.0	26	−0.177	0.199
40	306	13	1.0	31	−0.330	0.354
41	340	6	−1.0	10	0.224	0.383
42	35	4	−1.0	27	0.270	0.382
43	45	12.7	0.0	129	0.359	0.128
44	45	12.7	0.0	13	0.461	0.062
45	57	12.7	0.0	47	0.357	0.064
46	362	12.7	0.0	19	−0.577	0.058
47	83	12.7	0.0	17	0.227	0.104
48	553	12.7	0.0	13	−0.117	0.068
49	108	12.7	0.0	23	0.155	0.074
50	679	12.7	0.0	96	−0.245	0.138
51	159	12.7	0.0	15	0.122	0.078
52	1823	12.7	0.0	81	−0.520	0.221
53	235	12.7	0.0	12	0.058	0.054
54	273	12.7	0.0	22	0.034	0.071
55	5	12.7	0.0	58	0.308	0.211
56	322	12.7	0.0	24	−0.164	0.093
57	513	12.7	0.0	24	−0.202	0.108
58	640	12.7	0.0	17	−0.255	0.108
59	195	12.7	0.0	23	−0.014	0.047
60	45	19	0.0	23	0.265	0.073
61	732	54	0.0	4	0.097	0.026
62	696	76	0.0	3	0.014	0.035
63	63	28	0.0	5	0.246	0.071
64	609.5	13	0.0	16	143.9	70.12
65	914.4	13	0.0	45	80.93	88.89
66	609.5	13	0.0	13	103.0	138.4

Table 9. Predictions of all the data in table 5 using the fit to the HEM model

Case	L (mm)	D (mm)	$\cos\theta$	N-data	Mean $\left\langle \frac{G_m - G_c}{G_m} \right\rangle$	SD $\left\langle \left(\frac{G_m - G_c}{G_m} \right)^2 \right\rangle$
1	1015	26.3	0.0	31	0.762	0.124
2	152	38	0.0	5	−4.492	1.527
3	533.4	50.8	1.0	4	−6.515	2.769
4	305	38	0.0	6	−4.702	1.966
5	152	51	0.0	6	−4.132	1.721
6	305	51	0.0	5	−5.663	2.232
7	406	51	0.0	6	−5.401	2.262
8	305	76	0.0	5	−6.300	2.058
9	610	76	0.0	6	−6.005	2.424
10	406	51	0.0	4	−5.050	1.850
11	533	51	0.0	6	−7.864	4.276
12	500	12	0.0	10	−0.053	0.057
13	1600	30	0.0	5	−0.144	0.279
14	1700	50	0.0	6	0.083	0.096
15	660	13	0.0	33	−0.562	1.422
16	13	32	−1.0	6	−21.580	0.992
17	13	32	−1.0	9	−21.820	4.908
18	13	44	0.0	92	−0.029	0.029
19	2674	14	1.0	13	0.789	0.044
20	2674	14	1.0	24	0.597	0.086
21	914	5.8	0.0	35	0.659	0.108
22	914	8	0.0	26	0.029	0.867
23	914	8	0.0	71	−0.633	1.481
24	914	8	0.0	80	0.163	0.387
25	609	26	0.0	10	−2.708	2.276
26	609	21	0.0	8	−0.839	1.761
27	609	16	0.0	31	−0.402	1.271
28	609	10	0.0	47	0.174	0.903
29	609	13	0.0	10	−0.682	1.860
30	609	7	0.0	11	−0.017	1.214
31	463	20	1.0	15	−0.039	0.104
32	463	20	1.0	73	0.076	0.124
33	197	28	0.0	7	0.087	0.207
34	64	28	0.0	5	0.218	0.151
35	0	11	0.0	25	0.181	0.089
36	0	6	0.0	12	0.283	0.145
37	100	11	0.0	12	−4.256	0.143
38	2335	20	1.0	28	−0.680	0.120
39	306	13	1.0	26	−0.112	0.033
40	306	13	1.0	31	−0.089	0.059
41	340	6	−1.0	10	0.206	0.391
42	35	4	−1.0	27	0.274	0.369
43	45	12.7	0.0	129	0.363	0.126
44	45	12.7	0.0	13	0.467	0.068
45	57	12.7	0.0	47	0.362	0.066
46	362	12.7	0.0	19	−0.021	0.151
47	83	12.7	0.0	17	0.227	0.117
48	553	12.7	0.0	13	−0.110	0.088
49	108	12.7	0.0	23	0.160	0.086
50	679	12.7	0.0	96	−0.243	0.154
51	159	12.7	0.0	15	0.125	0.087
52	1823	12.7	0.0	81	−0.524	0.230
53	235	12.7	0.0	12	0.066	0.059
54	273	12.7	0.0	22	0.054	0.081
55	5	12.7	0.0	58	0.313	0.211
56	322	12.7	0.0	24	−0.154	0.101
57	513	12.7	0.0	24	−0.194	0.126
58	640	12.7	0.0	17	−0.239	0.112
59	195	12.7	0.0	23	−894.8	2965.0
60	45	19	0.0	23	0.278	0.072
61	732	54	0.0	4	0.111	0.027
62	696	76	0.0	3	0.031	0.036
63	63	28	0.0	5	0.273	0.083
64	609.5	13	0.0	16	0.639	0.133
65	914.4	13	0.0	45	0.100	0.976
66	609.5	13	0.0	13	−0.421	0.939

Table 10. Predictions of all the data in table 5 using the fit to the Moody model

Case	L (mm)	D (mm)	$\cos\theta$	N-data	Mean $\left\langle \frac{G_m - G_c}{G_m} \right\rangle$	SD $\left\langle \left(\frac{G_m - G_c}{G_m} \right)^2 \right\rangle$
1	1015	26.3	0.0	31	0.214	0.238
2	152	38	0.0	5	−4.489	1.528
3	533.4	50.8	1.0	4	−6.518	2.761
4	305	38	0.0	6	−4.704	1.970
5	152	51	0.0	6	−4.131	1.721
6	305	51	0.0	5	−5.667	2.242
7	406	51	0.0	6	−5.398	2.258
8	305	76	0.0	5	−6.297	2.058
9	610	76	0.0	6	−6.004	2.425
10	406	51	0.0	4	−5.051	1.854
11	533	51	0.0	6	−7.869	4.280
12	500	12	0.0	10	−0.188	0.110
13	1600	30	0.0	5	−0.410	0.170
14	1700	50	0.0	6	−0.035	0.078
15	660	13	0.0	33	−1.132	1.469
16	13	32	−1.0	6	−64.30	3.949
17	13	32	−1.0	9	−65.58	8.951
18	13	44	0.0	92	−0.029	0.029
19	2674	14	1.0	13	0.255	0.180
20	2674	14	1.0	24	−0.185	0.250
21	914	5.8	0.0	35	−0.043	0.307
22	914	8	0.0	26	−1.305	1.515
23	914	8	0.0	71	−2.558	2.473
24	914	8	0.0	80	−0.582	0.641
25	609	26	0.0	10	−2.878	2.152
26	609	21	0.0	8	−1.104	1.646
27	609	16	0.0	31	−0.691	1.185
28	609	10	0.0	47	−0.238	0.799
29	609	13	0.0	10	−1.056	1.673
30	609	7	0.0	11	−0.440	1.055
31	463	20	1.0	15	−0.120	0.018
32	463	20	1.0	73	−0.081	0.093
33	197	28	0.0	7	−0.361	0.316
34	64	28	0.0	5	−0.161	0.223
35	0	11	0.0	25	−0.647	0.088
36	0	6	0.0	12	−0.314	0.244
37	100	11	0.0	12	−4.256	0.142
38	2335	20	1.0	28	−0.657	0.108
39	306	13	1.0	26	−0.128	0.035
40	306	13	1.0	31	−0.094	0.055
41	340	6	−1.0	10	0.092	0.289
42	35	4	−1.0	27	0.207	0.361
43	45	12.7	0.0	129	0.080	0.171
44	45	12.7	0.0	13	0.243	0.116
45	57	12.7	0.0	47	0.089	0.213
46	362	12.7	0.0	19	−0.395	0.213
47	83	12.7	0.0	17	−0.006	0.172
48	553	12.7	0.0	13	−0.465	0.226
49	108	12.7	0.0	23	−0.150	0.170
50	679	12.7	0.0	96	−0.582	0.156
51	159	12.7	0.0	15	−0.192	0.182
52	1823	12.7	0.0	81	−0.874	0.202
53	235	12.7	0.0	12	−0.300	0.193
54	273	12.7	0.0	22	−0.395	0.157
55	5	12.7	0.0	58	0.080	0.132
56	322	12.7	0.0	24	−0.587	0.122
57	513	12.7	0.0	24	−0.636	0.115
58	640	12.7	0.0	17	−0.707	0.132
59	195	12.7	0.0	23	−0.402	0.198
60	45	19	0.0	23	−0.107	0.122
61	732	54	0.0	4	−0.342	0.026
62	696	76	0.0	3	−0.480	0.035
63	63	28	0.0	5	−0.046	0.164
64	609.5	13	0.0	16	0.001	0.242
65	914.4	13	0.0	45	−0.452	0.956
66	609.5	13	0.0	13	−0.827	0.903

Table 11. Selected critical flow data usable with the space-dependent models

Case	Reference	L (mm)	D (mm)	$\cos\theta$	N-data	Comments
1	Ardron & Ackerman (1978)	1015	26.3	0.0	31	
12	Boivin (1979)	500	12	0.0	10	$D = 50$ $(z < 0)$; $0 < z < 50$ rounded entrance; $D = 12$ $(50 < z < 500)$; $D = 12 + 19$ $(z - 500)$, $(z < 700)$; $D = 50$ $(z > 700$ mm)
13	Boivin (1979)	1600	30	0.0	5	$D = 150$ $(z < 0)$; $0 < z < 130$ rounded entrance; $D = 30$ $(130 < z < 1730)$; $D = 30 + 0.12$ $(z - 1730)$, $(z < 2305)$; $D = 100$ $(z > 2305$ mm)
14	Boivin (1979)	1700	50	0.0	6	$D = 150$ $(z < 0)$; $0 < z < 130$ rounded entrance; $D = 50$ $(130 < z < 1830)$; $D = 50 + 0.12$ $(z - 1830)$, $(z < 2240)$; $D = 100$ $(z > 2240$ mm)
43	Sozzi & Sutherland (1975)	45	12.7	0.0	129	$D = 43.2$ $(z = 0)$; rounded convergent $(0 < z < 44.5)$; $D = 12.7 + 0.105$ $(z - 44.5)$, $(z < 158.5$ mm)
44	Sozzi & Sutherland (1975)	45	12.7	0.0	13	$D = 43.2$ $(z = 0)$; rounded convergent $(0 < z < 44.5$ mm)
45	Sozzi & Sutherland (1975)	57	12.7	0.0	47	$D = 43.2$ $(z = 0)$; rounded convergent $(0 < z < 44.5$ mm)
46	Sozzi & Sutherland (1975)	362	12.7	0.0	19	$D = 43.2$ $(z = 0)$; rounded convergent $(0 < z < 44.5$ mm)
47	Sozzi & Sutherland (1975)	83	12.7	0.0	17	$D = 43.2$ $(z = 0)$; rounded convergent $(0 < z < 44.5$ mm)
48	Sozzi & Sutherland (1975)	553	12.7	0.0	13	$D = 43.2$ $(z = 0)$; rounded convergent $(0 < z < 44.5$ mm)
49	Sozzi & Sutherland (1975)	108	12.7	0.0	23	$D = 43.2$ $(z = 0)$; rounded convergent $(0 < z < 44.5$ mm)
50	Sozzi & Sutherland (1975)	679	12.7	0.0	96	$D = 43.2$ $(z = 0)$; rounded convergent $(0 < z < 44.5$ mm)
51	Sozzi & Sutherland (1975)	159	12.7	0.0	15	$D = 43.2$ $(z = 0)$; rounded convergent $(0 < z < 44.5$ mm)
52	Sozzi & Sutherland (1975)	1823	12.7	0.0	81	$D = 43.2$ $(z = 0)$; rounded convergent $(0 < z < 44.5$ mm)
53	Sozzi & Sutherland (1975)	235	12.7	0.0	12	$D = 43.2$ $(z = 0)$; rounded convergent $(0 < z < 44.5$ mm)
54	Sozzi & Sutherland (1975)	273	12.7	0.0	22	$D = 43.2$ $(z = 0)$; rounded convergent $(0 < z < 44.5$ mm)
55	Sozzi & Sutherland (1975)	5	12.7	0.0	58	Nozzle No. 3
56	Sozzi & Sutherland (1975)	322	12.7	0.0	24	Nozzle No. 3
57	Sozzi & Sutherland (1975)	513	12.7	0.0	24	Nozzle No. 3
58	Sozzi & Sutherland (1975)	640	12.7	0.0	17	Nozzle No. 3
59	Sozzi & Sutherland (1975)	195	12.7	0.0	23	Nozzle No. 3
60	Sozzi & Sutherland (1975)	45	19	0.0	23	$D = 43.2$ $(z = 0)$; rounded elliptical sec. $(0 < z < 44.5$ mm)

analysed. The following observations could be made on the effect of data uncertainties on the predictions:

Effect of inlet temperature uncertainty. It was not considered necessary to recalculate all points completely for each type of uncertainty. Thus, reduced set 1 contains 20 experiments, and the inlet temperature is reduced by the uncertainty listed in table 13(a) (0.1°C applied to each value in table 12) and each such case was recalculated; the case by case changes are shown in table 15(a) and the statistics in table 14. The effect of 0.1°C is 2.3% in mass flow, on average, while for individual cases it can be 5–8%.

Effect of pressure uncertainty. After reducing the test data set still further to 14 experiments, the effect of increasing the inlet pressure by 0.01 bar and then the simultaneous effect of both uncertainties were examined. The pressure effect contributes 4% on average, and the combined effects 6%, on average. In all such cases, the standard deviation is reduced as well, indicating that all calculations are closer to the correct values, on average. The individual cases are shown in tables 15(b) and (c).

Effect of 0.1 bar uncertainty. Table 13(b) indicates that a pressure uncertainty of 1.25% can be expected from repeatability considerations. Table 15(d) shows the effect of a 0.1 bar (plus 0.1°C) uncertainty which spans the range of 2.5–4% in inlet pressure uncertainty. This set of conditions (see table 14) carries the statistics from an error of +14 to −15%, indicating that pressure errors of 0–2% would be sufficient to bring all the A&A calculations into exact accord with measurement.

The attempt to validate data sets or to establish bounds on the value of various constitutive relations hinges in many cases on small differences in calculations (the nodalization, for example) or on the ability of the experimenter to measure quantities extremely precisely. Were the full statistical dimensionality of the measured and calculated flow rates to be laid out graphically, a perfect fit would be found (with the model used here for this demonstration).

The GSL model prediction and the A&A data are statistically nearly identical, although the nominal result shows a mean error of +18%. A far closer degree of attention by the experimenter is required to provide a clean differentiation, if any is warranted, between the model and experiment.

6. MODEL EVALUATION

In other analyses, several models have been shown simultaneously and compared against a given data set. Here this process does not appear useful. Consider the data in three steps:

- table 6 (1070 data points)
- table 11 (712 data points)
- Marviken (145 data points).

The data are further divided into subcooled and two-phase inlet so that there are six types of statistical and scatter plot graphs to be considered.

Table 12. Effect of inlet condition uncertainties on calculated critical flow rates; nominal inlet conditions

			Ardron & Ackerman experiments	
Run	Pressure (bar)	Inlet sub. (°C)	$G_{calc.}$ (kg/m²/s)	$G_{meas.}$ (kg/m²/s)
1	2.21	4.6	11584.28	13262.86
2	2.16	3.6	10254.19	10486.29
3	2.08	3.3	9454.17	10885.78
4	2.05	2.3	7877.55	9497.57
5	2.03	2.3	7902.27	9497.57
6	1.99	0.7	4833.52	7070.76
7	1.90	0.1	3108.53	5662.61
8	2.64	2.4	9252.74	11784.58
9	2.55	2.3	8696.29	10686.01
10	2.50	1.6	7534.28	9287.85
11	2.47	0.6	4858.02	6871.04
12	2.99	1.5	7721.81	9966.99
13	3.00	0.5	5505.55	7729.90
14	2.03	2.5	8261.98	9687.35
15	3.55	0.2	4966.70	6751.18
16	2.07	1.7	6619.77	8998.21
17	1.77	4.5	10153.89	10830.69
18	1.73	4.5	10134.53	10885.78
19	1.66	3.6	8969.35	9148.05
20	1.59	1.6	5767.25	7729.90
21	1.55	0.5	3758.68	6501.48
22	1.54	0.6	3787.03	5892.32
23	1.90	7.2	13333.36	13781.96
24	1.91	7.0	13140.13	13582.24
25	2.15	7.9	10453.52	11584.86
26	3.06	1.1	6849.92	9617.42
27	3.65	0.3	5418.02	7719.91
28	3.60	0.2	5196.70	7779.84
29	1.92	6.9	13176.89	13881.87
30	2.20	3.7	10234.78	11784.58
31	3.67	0.4	10031.06	7719.91

Table 13(a). Estimated errors due mainly to signal noise

Quantity	Uncertainty
Absolute pressure	± 700 N/m^2
Differential pressure	± 400 N/m^2
Mass velocity	± 200 kg/m^2/s
Liquid temperature	± 0.1°C
Void fraction	± 0.005

Table 13(b). Uncertainty for repeated runs

Condition	Value	Fraction
Entrance pressure	1.410 ± 0.03 bar	$\pm 1.25\%$
Entrance temperature (subcooling)	0.8 ± 0.25°C	$\pm 31.3\%$
Mass flow rate	7500 ± 370 kg/m^2/s	$\pm 4.93\%$

Except for the scatter plots, no attempt is made to agglomerate the data statistically and global statistics are not produced. If each of the approximately 40 geometries of table 6 is considered separately, only nine have more than 30 data points each and 15 have ten or less data points. Although means and standard deviations have been produced mechanically, for each set, only those with 15 or more data points should be considered as having some significance in the sense that the uncertainty in the mean is not large.

No trends were found in the quality of fit, between the calculated and measured results, with respect to pressure, length, diameter, L/D or any other parameter that holds between experimenters, although some intra-experimenter trends with some models were found. This is most clear with the Sozzi & Sutherland (1975) experiments, where there is a definite tendency for the mean value to change sign as L/D increases (for nozzles 2 and 3). But this trend is different for different models and some models do not show it at all.

The only statistical indicator considered here is the dimensionless indicator.

Mean

$$\mu = \frac{1}{N}\sum_{n=1}^{N} (G^n_{\text{meas}} - G^n_{\text{calc}})/G^n_{\text{meas}}$$

Standard deviation

$$\sigma = \left\{\frac{1}{N-1}\sum_{n=1}^{N}\left[\frac{G^n_{\text{meas}} - G^n_{\text{calc}}}{G^n_{\text{meas}}} - \mu\right]^2\right\}^{1/2}$$

Uncertainty in the mean

$$\Delta\mu = \pm \sigma/\sqrt{N}$$

6.1. The Table 6 Experiments

These experiments comprise nearly 1100 data points with pressures from 1 to 116 bar (15–1700 psia), diameters from 1.25 to 7.5 cm (1/2–3 in.) and lengths from approx. 4 mm–3 m (1/6 in.–9 ft). They are mostly horizontal but 7 sets of data (approx. 200 data points) are vertical upflow.

Table 14. Effect of inlet uncertainties on calculated critical flow statistics for the Ardron & Ackerman (1978) experiments

		Statistics	
Inlet conditions	N-data	Mean	SD
Nominal—all data points	31	0.181	0.148
Nominal—reduced data set I	20	0.180	0.179
Set I: temperature uncertainty	20	0.157	0.171
Nominal—reduced data set II	14	0.200	0.154
Set II: pressure uncertainty	14	0.161	0.132
Set II: combined uncertainty	14	0.142	0.119
Set III: combined uncertainty	13	0.144	0.124
Set III: 0.1 bar + temp. uncert.	13	−0.150	0.065

Table 15(a). Effect of inlet condition uncertainties on calculated critical flow rates; inlet temperatures reduced by temperature uncertainty

		Ardron & Ackerman experiments	
Run	Pressure (bar)	$G_{calc.}$ (kg/m^2/s)	$G_{meas.}$ (kg/m^2/s)
1	2.21	11708.62	13262.86
6	1.99	5091.33	7070.76
7	1.90	3332.67	5662.61
11	2.47	5108.54	6871.04
16	2.07	6830.71	8998.21
17	1.77	10266.28	10830.69
18	1.73	10247.95	10885.78
19	1.66	9088.47	9148.05
20	1.59	5948.39	7729.90
21	1.55	3975.39	6501.48
22	1.54	4027.93	5892.32
23	1.90	13405.14	13781.96
24	1.91	13210.83	13582.24
25	2.15	10659.05	11584.86
26	3.06	7150.43	9617.42
27	3.65	5679.38	7719.91
28	3.60	5460.05	7779.84
29	1.92	13285.38	13881.87
30	2.20	10388.23	11784.58
31	3.67	10262.67	7719.91

Table 15(b). Effect of inlet condition uncertainties on calculated critical flow rates; inlet conditions altered by pressure uncertainty

		Ardron & Ackerman experiments	
Run	Pressure (bar)	$G_{calc.}$ (kg/m^2/s)	$G_{meas.}$ (kg/m^2/s)
1	2.21	11625.72	13262.86
6	2.00	5207.62	7070.76
7	1.91	3497.83	5662.61
11	2.48	5215.91	6871.04
16	2.08	7041.60	8998.21
17	1.78	10378.62	10830.69
18	1.74	10361.31	10885.78
19	1.67	9219.49	9148.05
20	1.60	6149.67	7729.90
21	1.56	4219.20	6501.48
22	1.55	4242.76	5892.32
23	1.91	13512.80	13781.96
24	1.91	13316.98	13582.24
25	2.16	10664.70	11584.86

Table 15(c). Effect of inlet condition uncertainties on calculated critical flow rates; inlet conditions altered by pressure and temperature uncertainties

		Ardron & Ackerman experiments	
Run	Pressure (bar)	$G_{calc.}$ (kg/m^2/s)	$G_{meas.}$ (kg/m^2/s)
1	2.21	11750.06	13262.86
6	2.00	5459.57	7070.76
7	1.91	3757.34	5662.61
11	2.44	5466.39	6871.04
16	2.08	7041.60	8998.21
17	1.78	10462.88	10830.69
18	1.74	10474.73	10885.78
19	1.67	9333.88	9148.05
20	1.60	6310.73	7729.90
21	1.56	4444.38	6501.48
22	1.55	4488.27	5892.32
23	1.91	1358.46	13781.96
24	1.91	13387.68	13582.24
25	2.16	10785.38	11584.86

Table 15(d). Effect of inlet condition uncertainties on calculated critical flow rates; inlet conditions altered by 0.1 bar and temperature uncertainty

		Ardron & Ackerman experiments	
Run	Pressure (bar)	G_{calc} (kg/m^2/s)	G_{meas} (kg/m^2/s)
6	2.09	8120.33	7070.76
7	2.00	6954.37	5662.61
11	2.57	8170.07	6871.04
16	2.17	9377.86	8998.21
17	1.87	12285.79	10830.69
18	1.83	12297.50	10885.78
19	1.76	11303.56	9148.05
20	1.69	8853.15	7729.90

In the previous sections the scatter plots for all models for these data were shown. Table 16(a)–(h) shows the statistical results for the analytic and fitted functions. Table 16(i) shows these indicators for the fitted Moody and Henry–Fauske functions according to the RETRAN02/MOD3 procedures. Tables 17(a)–(h) and 18(a)–(h) show the statistics for the subcooled and two-phase inlet

Table 16(a). Predictions of all the data in table 6 using the fit to the Burnell model

Case	L (mm)	D (mm)	$\cos\theta$	N-data	Mean $\left\langle \frac{G_m - G_c}{G_m} \right\rangle$	SD $\left\langle \left(\frac{G_m - G_c}{G_m} \right)^2 \right\rangle$
1	1015	26.3	0.0	31	−0.268	0.385
2	152	38	0.0	5	−5.085	1.393
4	305	38	0.0	6	−5.416	1.805
5	152	51	0.0	6	−4.784	1.603
6	305	51	0.0	5	−6.363	2.083
7	406	51	0.0	6	−6.185	2.066
8	305	76	0.0	5	−7.088	1.860
9	610	76	0.0	6	−6.873	2.187
10	406	51	0.0	4	−5.952	1.689
11	533	51	0.0	6	−8.895	4.151
12	500	12	0.0	10	−0.647	0.163
13	1600	30	0.0	5	−0.789	0.185
14	1700	50	0.0	6	−0.392	0.112
18	13	44	0.0	92	−0.118	0.058
19	2674	14	1.0	13	−0.087	0.104
20	2674	14	1.0	24	−0.305	0.204
31	463	20	1.0	15	−0.373	0.109
32	463	20	1.0	73	−0.392	0.179
38	2335	20	1.0	28	−1.385	0.504
39	306	13	1.0	26	−0.515	0.220
40	306	13	1.0	31	−0.585	0.198
43	45	12.7	0.0	129	−0.076	0.157
44	45	12.7	0.0	13	0.123	0.086
45	57	12.7	0.0	47	−0.046	0.116
46	362	12.7	0.0	19	−0.640	0.268
47	83	12.7	0.0	17	−0.197	0.138
48	553	12.7	0.0	13	−0.780	0.147
49	108	12.7	0.0	23	−0.343	0.112
50	679	12.7	0.0	96	−0.885	0.142
51	159	12.7	0.0	15	−0.421	0.120
52	1823	12.7	0.0	81	−1.238	0.149
53	235	12.7	0.0	12	−0.514	0.122
54	273	12.7	0.0	22	−0.603	0.110
55	5	12.7	0.0	58	−0.067	0.125
56	322	12.7	0.0	24	−0.895	0.126
57	513	12.7	0.0	24	−0.911	0.114
58	640	12.7	0.0	17	−1.017	0.167
59	195	12.7	0.0	23	−0.657	0.120
60	45	19	0.0	23	−0.220	0.107
61	732	54	0.0	4	−0.477	0.030
62	696	76	0.0	3	−0.593	0.043
63	63	28	0.0	4	−0.227	0.125

Table 16(b). Predictions of all the data in table 6 using the isenthalpic model

Case	L (mm)	D (mm)	$\cos\theta$	N-data	Mean $\left\langle \frac{G_m - G_c}{G_m} \right\rangle$	SD $\left\langle \left(\frac{G_m - G_c}{G_m} \right)^2 \right\rangle$
1	1015	26.3	0.0	31	0.681	0.153
2	152	38	0.0	5	−4.491	1.527
4	305	38	0.0	6	−4.708	1.969
5	152	51	0.0	6	−4.137	1.725
6	305	51	0.0	5	−5.669	2.236
7	406	51	0.0	6	−5.401	2.259
8	305	76	0.0	5	−6.299	2.056
9	610	76	0.0	6	−6.004	2.423
10	406	51	0.0	4	−5.049	1.853
11	533	51	0.0	6	−7.869	4.280
12	500	12	0.0	10	−0.124	0.064
13	1600	30	0.0	5	−0.338	0.210
14	1700	50	0.0	6	0.011	0.069
18	13	44	0.0	92	−0.029	0.029
19	2674	14	1.0	13	0.755	0.036
20	2674	14	1.0	24	0.582	0.101
31	463	20	1.0	15	−0.111	0.038
32	463	20	1.0	73	−0.011	0.058
38	2335	20	1.0	28	−0.682	0.122
39	306	13	1.0	26	−0.114	0.033
40	306	13	1.0	31	−0.090	0.059
43	45	12.7	0.0	129	0.358	0.116
44	45	12.7	0.0	13	0.462	0.062
45	57	12.7	0.0	47	0.366	0.063
46	362	12.7	0.0	19	−0.031	0.166
47	83	12.7	0.0	17	0.221	0.109
48	553	12.7	0.0	13	−0.137	0.086
49	108	12.7	0.0	23	0.155	0.074
50	679	12.7	0.0	96	−0.285	0.184
51	159	12.7	0.0	15	0.114	0.076
52	1823	12.7	0.0	81	−0.558	0.233
53	235	12.7	0.0	12	0.063	0.061
54	273	12.7	0.0	22	0.028	0.059
55	5	12.7	0.0	58	0.307	0.213
56	322	12.7	0.0	24	−0.226	0.190
57	513	12.7	0.0	24	−0.200	0.157
58	640	12.7	0.0	17	−0.266	0.174
59	195	12.7	0.0	23	−0.025	0.059
60	45	19	0.0	23	0.281	0.056
61	732	54	0.0	4	0.124	0.026
62	696	76	0.0	3	0.046	0.035
63	63	28	0.0	4	0.250	0.081

cases separately. Figures 7(a)–(h) and 8(a)–(h) show the scatter plots for each model for subcooled and two-phase inlet conditions, respectively.

None of these models provide a reasonably good fit for two-phase inlet conditions. The isenthalpic model and its fit and the HEM model provide relatively centered fits for subcooled inlet condititons but the spread is at least a factor of two in either way.

6.2. The Table 11 Experiments

These experiments comprise 712 data points in a horizontal channel with pressures from 1.5 to 100 bar (22–1500 psia), diameters from 1.25 to 5 cm (1/2–2 in.) and lengths from approx. 4 mm to 1.8 m (1/6 in.–5.4 ft). All points were calculated with the GSL model; for the Elias–Chambré and Richter models, only the subset comprising geometries 43–54 (Sozzi & Sutherland nozzles 1 and 2) were calculated (480 data points).

Table 19(a)–(c) shows the statistics for all the geometries; tables 20(a)–(c) and 21(a) and (b) show statistics for the subcooled and two-phase inlet portions of these data. Figures 9(a)–(c) and 10(a)–(c) show the scatter plots for subcooled and two-phase inlet conditions for the subset (geometries 43–54) for all three models and figures 9(d) and 10(d) show all of table 11 for the GSL model. All three models show reasonable statistics and centering; the Richter and GSL model are substantially better than the Elias–Chambré model. The Richter model is somewhat better for

two-phase inlet conditions [see figure 10(b)] and the GSL model is somewhat better for subcooled inlet conditions [see figures 9(c) and (d)].

6.3. *The Marviken Experiments*

This subset of data (a subset of the Marviken data) consists of 145 data points. Although it would be most desirable to test the capabilities of the models with respect to the nozzle alone, our inability to locate a consistent set of nozzle inlet conditions which were not compromised by extensive secondary calculations has led us to use inlet conditions at the start of the discharge pipe. (See however the section on use of TRACPF1/MOD1 below).

6.3.1. *The analytic and fitted models*

Figure 11(a)–(g) shows the prediction of these experimental points using all of the simple models (except for the isenthalpic model which was not used here). The results are consistent with those for the earlier sets of horizontal and vertical upflow data sets. These models do not provide the consistent or well-centered predictions required of a viable calculation tool.

6.3.2. *The space-dependent models*

(1) The Elias–Chambré model. Attempts to predict the Marviken experiments using this model have been unsuccessful and no further use of the model was made.

Table 16(c). Predictions of all the data in table 6 using the fit to the isoenthalpic model

Case	L (mm)	D (mm)	$\cos\theta$	N-data	Mean $\left\langle \frac{G_m - G_c}{G_m} \right\rangle$	SD $\left\langle \left(\frac{G_m - G_c}{G_m} \right)^2 \right\rangle$
1	1015	26.3	0.0	31	0.391	0.136
2	152	38	0.0	5	−5.144	1.563
4	305	38	0.0	6	−5.329	2.180
5	152	51	0.0	6	−4.711	1.917
6	305	51	0.0	5	−6.431	2.263
7	406	51	0.0	6	−6.086	2.459
8	305	76	0.0	5	−7.156	2.064
9	610	76	0.0	6	−6.743	2.610
10	406	51	0.0	4	−5.738	2.255
11	533	51	0.0	6	−8.833	4.625
12	500	12	0.0	10	−4.176	0.063
13	1600	30	0.0	5	−0.167	0.241
14	1700	50	0.0	6	0.088	0.073
18	13	44	0.0	92	−0.105	0.049
19	2674	14	1.0	13	84.45	72.14
20	2674	14	1.0	24	91.16	69.95
31	463	20	1.0	15	−0.023	0.079
32	463	20	1.0	73	0.098	0.115
38	2335	20	1.0	28	−0.777	0.196
39	306	13	1.0	26	−0.177	0.199
40	306	13	1.0	31	−0.330	0.354
44	45	12.7	0.0	13	0.461	0.062
45	57	12.7	0.0	47	0.357	0.064
46	362	12.7	0.0	19	−0.058	0.058
47	83	12.7	0.0	17	0.227	0.104
48	553	12.7	0.0	13	−0.117	0.068
49	108	12.7	0.0	23	0.155	0.074
50	679	12.7	0.0	96	−0.249	0.138
51	159	12.7	0.0	15	0.122	0.078
52	1823	12.7	0.0	81	−0.520	0.221
53	235	12.7	0.0	12	0.058	0.054
54	273	12.7	0.0	22	0.034	0.072
55	5	12.7	0.0	58	0.308	0.211
56	322	12.7	0.0	24	−0.164	0.093
57	513	12.7	0.0	24	−0.202	0.108
58	640	12.7	0.0	17	−0.256	0.108
59	195	12.7	0.0	23	−0.014	0.047
60	45	19	0.0	23	0.265	0.073
61	732	54	0.0	4	0.097	0.026
62	696	76	0.0	3	0.014	0.035
63	63	28	0.0	4	0.246	0.072

Table 16(d). Predictions of all the data in table 6 using the Moody model

Case	L (mm)	D (mm)	$\cos\theta$	N-data	Mean $\left\langle \frac{G_m - G_c}{G_m} \right\rangle$	SD $\left\langle \left(\frac{G_m - G_c}{G_m} \right)^2 \right\rangle$
1	1015	26.3	0.0	31	0.215	0.238
2	152	38	0.0	5	−4.489	1.528
4	305	38	0.0	6	−4.704	1.969
5	152	51	0.0	6	−4.131	1.721
6	305	51	0.0	5	−5.666	2.242
7	406	51	0.0	6	−5.398	2.258
8	305	76	0.0	5	−6.297	2.058
9	610	76	0.0	6	−6.004	2.425
10	406	51	0.0	4	−5.051	1.854
11	533	51	0.0	6	−7.869	4.280
12	500	12	0.0	10	−0.188	0.110
13	1600	30	0.0	5	−0.410	0.170
14	1700	50	0.0	6	−0.035	0.078
18	13	44	0.0	92	−0.029	0.029
19	2674	14	1.0	13	0.255	0.180
20	2674	14	1.0	24	−0.185	0.250
31	463	20	1.0	15	−0.120	0.018
32	463	20	1.0	73	−0.081	0.093
38	2335	20	1.0	28	−0.657	0.108
39	306	13	1.0	26	−0.128	0.035
40	306	13	1.0	31	−0.094	0.055
43	45	12.7	0.0	129	0.080	0.171
44	45	12.7	0.0	13	0.243	0.116
45	57	12.7	0.0	47	0.089	0.140
46	362	12.7	0.0	19	−0.395	0.213
47	83	12.7	0.0	17	−0.007	0.172
48	553	12.7	0.0	13	−0.465	0.226
49	108	12.7	0.0	23	−0.150	0.170
50	679	12.7	0.0	96	−0.582	0.156
51	159	12.7	0.0	15	−0.192	0.182
52	1823	12.7	0.0	81	−0.874	0.202
53	235	12.7	0.0	12	−0.300	0.193
54	273	12.7	0.0	22	−0.395	0.157
55	5	12.7	0.0	58	0.805	0.132
56	322	12.7	0.0	24	−0.587	0.122
57	513	12.7	0.0	24	−0.636	0.115
58	640	12.7	0.0	17	−0.707	0.132
59	195	12.7	0.0	23	−0.402	0.198
60	45	19	0.0	23	−0.107	0.122
61	732	54	0.0	4	−0.342	0.027
62	696	76	0.0	3	−0.480	0.035
63	63	28	0.0	4	−0.046	0.164

(2) The complete drift flux model. Attempts to predict the Marviken test data using the GSL model have not been successful. Results were obtained which are not only numerically unacceptable but have demonstrated non-physical behavior as well. This behavior has been traced to two limitations of the Chexal & Lellouche (1986) and the Lellouche & Zolotar (1982) models (CLZ model). These limitations are:

(1) The CLZ model exhibits non-physical behavior in flow quadrants 2 and 3 when $|j_L|$ is large. The critical value for j_L is $-3.45 \times 10^6 \mu / D_h \rho_L$ which is very large for reactor core conditions ($D_h \approx 0.05$ ft) but quite small for Marviken discharge pipe conditions ($D_h \approx 2.5$ ft).

(2) The CLZ model does not admit $\epsilon = 0$ solutions for $j_G \to 0$ in flow quadrant 3. This means that when voids first form with $G_G \approx 10^{-8} G_0$ they form with $V_G \approx 0$ and $\epsilon \approx 0.7$–0.8; this sudden change from a continuous liquid phase with $\epsilon = 0$ to a nearly stagnant continuous vapor phase with large ϵ is clearly non-physical.

The version of the CLZ model used here is that described in Chexal & Lellouche (1986). When these results were communicated to them, alterations in the model were made and the modified model has been reproofed against downflow data (Chexal *et al.* 1989). While both problems noted above have been resolved and the resulting critical flow rates are quite

reasonable at the nozzle, the onset of vaporization with $\epsilon \approx 0$ in downflow still exhibits the non-physical result $V_G \approx 0$. This condition although acceptable for an onset condition due to boiling on a heated wall, is still unacceptable for bulk vaporization due to depressurization during downflow (no problem exists in upflow or countercurrent flow). As such the model is still not really acceptable for predicting the Marviken experiments.

(3) The Richter model. Attempts to predict the Marviken experiments with the Richter model have only been partly successful. This situation is most suprising since an earlier analysis (Abdollahian *et al.* 1982) showed fair to good success using this model with the Marviken data. Extensive efforts by Abdollahian to determine why this dichotomy has occurred have not been successful. No significant errors have been found in the current version of the Richter code but the version of the code used in Abdollahian *et al.* (1982) has not been located. The major problem with the code can be understood by examining figure 12(a) and (b). Figure 12 shows that there is a solution (for this particular case) at the nozzle exit with a mass flow rate of about 100,000 kg/m^2 s which is about a factor of 2 too large. Figure 12(b) shows an enlargement in the neighborhood of the nozzle exit. It is clear that the model exhibits three solutions, the lowest of which is close to the experimental value. The origin of this non-physical result may lie in the use of the vapor mass equation twice, once to determine the total mass then in a truncated form to

Table 16(e). Predictions of all the data in table 6 using the fit to the Moody model

Case	L (mm)	D (mm)	$\cos\theta$	N-data	Mean $\left\langle \frac{G_m - G_c}{G_m} \right\rangle$	SD $\left\langle \left(\frac{G_m - G_c}{G_m} \right)^2 \right\rangle$
1	1015	26.3	0.0	31	0.230	0.238
2	152	38	0.0	5	−4.882	3.191
4	305	38	0.0	6	−4.985	3.626
5	152	51	0.0	6	−4.010	2.396
6	305	51	0.0	5	−6.352	4.723
7	406	51	0.0	6	−5.810	4.383
8	305	76	0.0	5	−6.872	4.517
9	610	76	0.0	6	−6.494	4.940
10	406	51	0.0	4	−4.568	2.285
11	533	51	0.0	6	−8.579	7.374
12	500	12	0.0	10	−0.170	0.161
13	1600	30	0.0	5	−0.389	0.128
14	1700	50	0.0	6	−0.001	0.126
18	13	44	0.0	92	−0.280	0.395
19	2674	14	1.0	13	0.265	0.170
20	2674	14	1.0	24	−0.175	0.239
31	463	20	1.0	15	−0.014	0.132
32	463	20	1.0	73	−0.014	0.165
38	2335	20	1.0	28	−0.498	0.248
39	306	13	1.0	26	−0.024	0.128
40	306	13	1.0	31	−0.026	0.109
43	45	12.7	0.0	129	0.092	0.189
44	45	12.7	0.0	13	0.246	0.126
45	57	12.7	0.0	47	0.093	0.157
46	362	12.7	0.0	19	−0.383	0.246
47	83	12.7	0.0	17	0.025	0.205
48	553	12.7	0.0	13	−0.449	0.260
49	108	12.7	0.0	23	−0.135	0.198
50	679	12.7	0.0	96	−0.512	0.255
51	159	12.7	0.0	15	−0.190	0.196
52	1823	12.7	0.0	81	−0.761	0.304
53	235	12.7	0.0	12	−0.301	0.206
54	273	12.7	0.0	22	−0.405	0.154
55	5	12.7	0.0	58	0.124	0.092
56	322	12.7	0.0	24	−0.585	0.161
57	513	12.7	0.0	24	−0.615	0.190
58	640	12.7	0.0	17	−0.694	0.203
59	195	12.7	0.0	23	−0.410	0.203
60	45	19	0.0	23	−0.111	0.120
61	732	54	0.0	4	−0.347	0.027
62	696	76	0.0	3	−0.483	0.036
63	63	28	0.0	4	−0.054	0.161

Table 16(f). Predictions of all the data in table 6 using the Henry–Fauske model

Case	L (mm)	D (mm)	$\cos\theta$	N-data	Mean $\left\langle \frac{G_m - G_c}{G_m} \right\rangle$	SD $\left\langle \left(\frac{G_m - G_c}{G_m} \right)^2 \right\rangle$
1	1015	26.3	0.0	31	0.065	0.223
2	152	38	0.0	5	−4.453	1.478
4	305	38	0.0	6	−4.691	1.892
5	152	51	0.0	6	−4.125	1.662
6	305	51	0.0	5	−5.618	2.169
7	406	51	0.0	6	−5.384	2.176
8	305	76	0.0	5	−6.251	1.985
9	610	76	0.0	6	−5.986	2.328
10	406	51	0.0	4	−5.058	1.760
11	533	51	0.0	6	−7.837	4.162
12	500	12	0.0	10	−0.500	0.172
13	1600	30	0.0	5	−0.752	0.157
14	1700	50	0.0	6	−0.286	0.121
18	13	44	0.0	92	−0.018	0.025
19	2674	14	1.0	13	0.269	0.084
20	2674	14	1.0	24	0.001	0.182
31	463	20	1.0	15	−0.282	0.131
32	463	20	1.0	73	−0.293	0.163
38	2335	20	1.0	28	−0.840	0.264
39	306	13	1.0	26	−0.240	0.123
40	306	13	1.0	31	−0.251	0.121
43	45	12.7	0.0	129	−0.095	0.189
44	45	12.7	0.0	13	0.097	0.115
45	57	12.7	0.0	47	−0.086	0.151
46	362	12.7	0.0	19	−0.735	0.191
47	83	12.7	0.0	17	−0.207	0.200
48	553	12.7	0.0	13	−0.800	0.261
49	108	12.7	0.0	23	−0.377	0.185
50	679	12.7	0.0	96	−0.888	0.232
51	159	12.7	0.0	15	−0.457	0.192
52	1823	12.7	0.0	81	−1.223	0.271
53	235	12.7	0.0	12	−0.566	0.196
54	273	12.7	0.0	22	−0.685	0.152
55	5	12.7	0.0	58	−0.068	0.094
56	322	12.7	0.0	24	−0.924	0.148
57	513	12.7	0.0	24	−0.973	0.170
58	640	12.7	0.0	17	−1.080	0.204
59	195	12.7	0.0	23	−0.714	0.199
60	45	19	0.0	23	−0.268	0.110
61	732	54	0.0	4	−0.557	0.045
62	696	76	0.0	3	−0.659	0.061
63	63	28	0.0	4	−0.265	0.148

determine the bubble diameter. For some cases the lower two roots move to the right and only the highest value remains. In other cases the structure shifts to the left leaving only the lower root.

In any event we are unable to determine which root has physical meaning when all three are present and choose not to present any results at all.

Commentary. Since all three of these model produces reasonable results for upflow and horizontal flow in small diameter pipes (1/2–2 in.) it is surprising that they all fail in large diameter downflow situations. Perhaps it only shows that a factor of 20 extrapolation in diameter as well as a factor of 30 in mass flow rate is just too large a jump for any data-based set of correlations. It is clear that much further work is needed at these conditions.

6.3.3. RELAP5 MOD2 evaluations

No evaluations are performed using the RELAP5/MOD2 methodology. As with the other similar models, a full numerical solution in the context of the code itself should be considered. This was considered to be outside the scope of the present paper. Therefore, no statements can be made concerning the adequacy of the model.

6.3.4. *TRAC-PF1/MOD1 evaluations*

The considerations raised above concerning RELAP5/MOD2 hold for TRAC as well. However, the TRAC manual contains a number of comparison calculations with experiment and with other choking models. Because of this, additional comments appear in order.

TRAC compares its model against the HEM and Burnell model. Figure 13 reproduces the TRAC comparison. It is seen that the TRAC model lies about one-quarter to one-third the distance between the two models and closer to the Burnell model. In comparing this result against the comparison of the HEM and Burnell models against data (table 22), it is *assumed* that the *statistics* will follow this one-quarter to one-third distance relation. Table 22 shows all the subcooled cases with NDATA > 10. The average mean is about −0.5 for a 50% overprediction of the mass flow rate compared to experiment.

TRAC also presents several comparisons to Marviken and one to the Edwards & O'Brien (1970) experiment. In all cases the upstream vessel pressure predictions are 5–15% off. The mass flow rates are 15–30% off during the early phases of the depressurization, are quite accurate in a middle phase, and are significantly in error late in the blowdown (where the error in the early phase keeps the

Table 16(g). Predictions of all the data in table 6 using the fit to the Henry–Fauske model

Case	L (mm)	D (mm)	$\cos\theta$	N-data	Mean $\left\langle \frac{G_m - G_c}{G_m} \right\rangle$	SD $\left\langle \left(\frac{G_m - G_c}{G_m} \right)^2 \right\rangle$
1	1015	26.3	0.0	31	0.228	0.250
2	152	38	0.0	5	−4.320	1.515
4	305	38	0.0	6	−4.560	1.891
5	152	51	0.0	6	−3.925	1.537
6	305	51	0.0	5	−5.472	2.258
7	406	51	0.0	6	−5.244	2.202
8	305	76	0.0	5	−6.077	2.072
9	610	76	0.0	6	−5.844	2.389
10	406	51	0.0	4	−4.872	1.645
11	533	51	0.0	6	−7.633	4.186
12	500	12	0.0	10	−0.485	0.158
13	1600	30	0.0	5	−0.747	0.170
14	1700	50	0.0	6	−0.277	0.099
18	13	44	0.0	92	0.008	0.067
19	2674	14	1.0	13	0.285	0.151
20	2674	14	1.0	24	−0.091	0.181
31	463	20	1.0	15	−0.308	0.116
32	463	20	1.0	73	−0.284	0.117
38	2335	20	1.0	28	−0.794	0.228
39	306	13	1.0	26	−0.241	0.093
40	306	13	1.0	31	−0.239	0.104
43	45	12.7	0.0	129	−0.064	0.186
44	45	12.7	0.0	13	0.114	0.109
45	57	12.7	0.0	47	−0.063	0.141
46	362	12.7	0.0	19	−0.592	0.473
47	83	12.7	0.0	17	−0.189	0.175
48	553	12.7	0.0	13	−0.763	0.208
49	108	12.7	0.0	23	−0.353	0.160
50	679	12.7	0.0	96	−0.869	0.184
51	159	12.7	0.0	15	−0.424	0.163
52	1823	12.7	0.0	81	−1.206	0.209
53	235	12.7	0.0	12	−0.538	0.171
54	273	12.7	0.0	22	−0.640	0.142
55	5	12.7	0.0	58	−0.057	0.112
56	322	12.7	0.0	24	−0.900	0.130
57	513	12.7	0.0	24	−0.928	0.134
58	640	12.7	0.0	17	−1.028	0.172
59	195	12.7	0.0	23	−0.673	0.167
60	45	19	0.0	23	−0.258	0.120
61	732	54	0.0	4	−0.536	0.038
62	696	76	0.0	3	−0.664	0.052
63	63	28	0.0	4	−0.245	0.154

Table 16(h). Predictions of all the data in table 6 using the HEM model

Case	L (mm)	D (mm)	$\cos\theta$	N-data	Mean $\left\langle \frac{G_m - G_c}{G_m} \right\rangle$	SD $\left\langle \left(\frac{G_m - G_c}{G_m} \right)^2 \right\rangle$
1	1015	26.3	0.0	31	0.762	0.124
2	152	38	0.0	5	−4.492	1.527
4	305	38	0.0	6	−4.702	1.966
5	152	51	0.0	6	−4.132	1.721
6	305	51	0.0	5	−5.663	2.232
7	406	51	0.0	6	−5.401	2.262
8	305	76	0.0	5	−6.300	2.058
9	610	76	0.0	6	−6.005	2.424
10	406	51	0.0	4	−5.050	1.850
11	533	51	0.0	6	−7.864	4.276
12	500	12	0.0	10	−0.053	0.057
13	1600	30	0.0	5	−0.144	0.279
14	1700	50	0.0	6	0.083	0.096
18	13	44	0.0	92	−0.029	0.029
19	2674	14	1.0	13	0.789	0.044
20	2674	14	1.0	24	0.597	0.086
31	463	20	1.0	15	−0.039	0.104
32	463	20	1.0	73	0.076	0.124
38	2335	20	1.0	28	−0.680	0.120
39	306	13	1.0	26	−0.112	0.033
40	306	13	1.0	31	−0.089	0.059
43	45	12.7	0.0	129	0.363	0.126
44	45	12.7	0.0	13	0.467	0.068
45	57	12.7	0.0	47	0.362	0.066
46	362	12.7	0.0	19	−0.021	0.151
47	83	12.7	0.0	17	0.227	0.117
48	553	12.7	0.0	13	−0.110	0.088
49	108	12.7	0.0	23	0.160	0.086
50	679	12.7	0.0	96	−0.243	0.154
51	159	12.7	0.0	15	0.125	0.087
52	1823	12.7	0.0	81	−0.524	0.230
53	235	12.7	0.0	12	0.066	0.059
54	273	12.7	0.0	22	0.054	0.081
55	5	12.7	0.0	58	0.313	0.211
56	322	12.7	0.0	24	−0.154	0.101
57	513	12.7	0.0	24	−0.194	0.126
58	640	12.7	0.0	17	−0.239	0.112
59	195	12.7	0.0	23	−894.8	2965.0
60	45	19	0.0	23	0.278	0.072
61	732	54	0.0	4	0.111	0.027
62	696	76	0.0	3	0.031	0.036
63	63	28	0.0	4	0.273	0.083

calculation going longer than it should). The quite good comparison with the Edwards experiment is expected because Alamgir & Lienhard (1981) used it among others in tuning their model. However, it is doubtful that the model would have been tuned differently if the Edwards experiment had not been used. Hence, one can reasonably accept the Edwards pressure history prediction as valid.

Although we have not performed any TRAC calculations, W. Yu at Brookhaven National Laboratory has made a set of Marviken calculations available to us. These calculations were done on the nozzle itself without accounting for the rest of the discharge pipe. In order to do this the nozzle inlet conditions had to be estimated (see the earlier discussion on nozzle inlet condition uncertainties). Although we restricted our Marviken studies to data taken subsequent to 5 s into each transient, the BNL studies are nearly all for times less than 5 s into the transients. The experimental runs considered were: 12, 13, 15–19, 21, 22, 25 and the statistical comparison to experiment is found in table 23; the mean errors run from 3 to 30% and except for tests 15 and 19 the standard deviations are $<12\%$. However, figure 14 shows that TRAC nearly always underpredicts the data. This conclusion may, however, be more closely related to the specific

Table 16(i). Predictions of all the data in table 6 using the fit to the Moody and Henry–Fauske models according to the RETRAN procedures

Case	L (mm)	D (mm)	$\cos\theta$	N-data	Mean $\left\langle \frac{G_m - G_c}{G_m} \right\rangle$	SD $\left\langle \left(\frac{G_m - G_c}{G_m} \right)^2 \right\rangle$
1	1015	26.3	0.0	31	0.229	0.240
2	152	38	0.0	5	−4.320	1.515
4	305	38	0.0	6	−4.560	1.891
5	152	51	0.0	6	−3.925	1.537
6	305	51	0.0	5	−5.472	2.258
7	406	51	0.0	6	−5.244	2.202
8	305	76	0.0	5	−6.077	2.072
9	610	76	0.0	6	−5.844	2.389
10	406	51	0.0	4	−4.872	1.645
11	533	51	0.0	6	−7.633	4.186
12	500	12	0.0	10	−0.356	0.089
13	1600	30	0.0	5	−0.553	0.216
14	1700	50	0.0	6	−0.176	0.042
18	13	44	0.0	92	0.008	0.067
19	2674	14	1.0	13	0.265	0.170
20	2674	14	1.0	24	−0.175	0.239
31	463	20	1.0	15	−0.238	0.066
32	463	20	1.0	73	−0.192	0.068
38	2335	20	1.0	28	−0.781	0.209
39	306	13	1.0	26	−0.225	0.073
40	306	13	1.0	31	−0.209	0.080
43	45	12.7	0.0	129	0.056	0.155
44	45	12.7	0.0	13	0.218	0.092
45	57	12.7	0.0	47	0.064	0.111
46	362	12.7	0.0	19	−0.464	0.173
47	83	12.7	0.0	17	−0.070	0.133
48	553	12.7	0.0	13	−0.563	0.137
49	108	12.7	0.0	23	−0.200	0.116
50	679	12.7	0.0	96	−0.681	0.103
51	159	12.7	0.0	15	−0.253	0.121
52	1823	12.7	0.0	81	−1.002	0.136
53	235	12.7	0.0	12	−0.351	0.124
54	273	12.7	0.0	22	−0.419	0.128
55	5	12.7	0.0	58	0.045	0.139
56	322	12.7	0.0	24	−0.663	0.073
57	513	12.7	0.0	24	−0.702	0.070
58	640	12.7	0.0	17	−0.780	0.095
59	195	12.7	0.0	23	−0.459	0.125
60	45	19	0.0	23	−0.112	0.117
61	732	54	0.0	4	−0.347	0.027
62	696	76	0.0	3	−0.483	0.036
63	63	28	0.0	4	−0.075	0.136

methods used to establish the inlet conditions than either the model or the measured critical flow rate.

7. RECOMMENDED MODELS

In making recommendations for the use of a critical flow model, it is important to realize how these models are implemented. In practice none of the analytic or fitted models will be used as has been done in this work (i.e. they will not be used to solve the entire geometry at once). Actually, considering the way the system codes work, these models are used as exit boundary conditions, connecting the last volume to the "outside".

In such a situation, the nominal set of equations [3, 4, 5 or 6] are solved through this last volume, and the critical flow model provides the terminal junction information needed to close the system of equations. As an example, consider the HEM model, [20]–[22d], in a space-dependent setting.

Table 17(a). Predictions of all the data in table 6 using the fit to the Burnell model

Case	L (mm)	D (mm)	$\cos\theta$	N-data	Mean $\left\langle \frac{G_m - G_c}{G_m} \right\rangle$	SD $\left\langle \left(\frac{G_m - G_c}{G_m} \right)^2 \right\rangle$
1	1015	26.3	0.0	31	−0.268	0.385
2	152	38	0.0	5	−5.085	1.393
4	305	38	0.0	6	−5.416	1.805
5	152	51	0.0	6	−4.784	1.603
6	305	51	0.0	5	−6.363	2.083
7	406	51	0.0	6	−6.185	2.066
8	305	76	0.0	5	−7.088	1.860
9	610	76	0.0	6	−6.873	2.187
10	406	51	0.0	4	−5.952	1.689
11	533	51	0.0	6	−8.895	4.151
12	500	12	0.0	10	−0.647	0.163
13	1600	30	0.0	5	−0.789	0.185
14	1700	50	0.0	6	−0.392	0.112
18	13	44	0.0	92	−0.118	0.058
19	2674	14	1.0	5	0.016	0.002
20	2674	14	1.0	2	−0.460	0.122
31	463	20	1.0	15	−0.373	0.109
32	463	20	1.0	71	−0.395	0.180
38	2335	20	1.0	28	−1.385	0.504
39	306	13	1.0	26	−0.515	0.220
40	306	13	1.0	31	−0.585	0.198
43	45	12.7	0.0	30	0.074	0.081
44	45	12.7	0.0	3	0.209	0.048
45	57	12.7	0.0	9	0.125	0.055
46	362	12.7	0.0	6	−0.610	0.148
47	83	12.7	0.0	7	−0.100	0.071
48	553	12.7	0.0	6	−0.641	0.082
49	108	12.7	0.0	7	−0.199	0.062
50	679	12.7	0.0	49	−0.865	0.180
51	159	12.7	0.0	5	−0.293	0.050
52	1823	12.7	0.0	45	−1.184	0.163
53	235	12.7	0.0	3	−0.365	0.075
54	273	12.7	0.0	4	−0.438	0.030
55	5	12.7	0.0	17	−0.173	0.151
56	322	12.7	0.0	10	−0.959	0.179
57	513	12.7	0.0	6	−0.928	0.240
58	640	12.7	0.0	5	−1.072	0.316
59	195	12.7	0.0	7	−0.513	0.072
60	45	19	0.0	1	−0.072	—

If the final function is labeled $m + 1$ and all variables are assumed to be calculated at the junctions with no staggered grid, [21] will be written in steady state as:

$$G^2 = \frac{2\rho_{n+1}^2 (H_n - H_{n+1})}{1 - (\rho_{n+1}/\rho_n)^2}$$

where ρ_n and H_n are "known" upstream properties. But, these known values are solutions of the nominal equations and are functions of the constitutive relations imposed on those equations. In practice, the result is that the calculated critical flow may depend more on the other constitutive relations and correlations (CRC) than on the imposed critical flow model because each code that contains a momentum equation automatically contains a critical flow model.

Thus, if one wanted to make recommendations, it would have been necessary to run each system code (RETRAN02, RELAP5, TRAC P/B etc.) for each model. This is clearly economically impossible; therefore, the recommendations are made based on the application of the model as it was developed. Such a recommendation may be good or bad depending on the quality of the other constitutive relations in any particular systems code.

Table 17(b). Predictions of all the data in table 6 using the isenthalpic model

Case	L (mm)	D (mm)	$\cos\theta$	N-data	Mean $\left\langle \frac{G_m - G_c}{G_m} \right\rangle$	SD $\left\langle \left(\frac{G_m - G_c}{G_m}\right)^2 \right\rangle$
1	1015	26.3	0.0	31	0.681	0.153
2	152	38	0.0	5	−4.491	1.527
4	305	38	0.0	6	−4.708	1.969
5	152	51	0.0	6	−4.137	1.725
6	305	51	0.0	5	−5.669	2.236
7	406	51	0.0	6	−5.401	2.259
8	305	76	0.0	5	−6.299	2.056
9	610	76	0.0	6	−6.004	2.423
10	406	51	0.0	4	−5.049	1.853
11	533	51	0.0	6	−7.869	4.280
12	500	12	0.0	10	−0.124	0.064
13	1600	30	0.0	5	−0.338	0.185
14	1700	50	0.0	6	0.011	0.069
18	13	44	0.0	92	−0.029	0.029
19	2674	14	1.0	5	0.738	0.001
20	2674	14	1.0	2	0.409	0.059
31	463	20	1.0	15	−0.111	0.038
32	463	20	1.0	71	−0.016	0.046
38	2335	20	1.0	28	−0.682	0.122
39	306	13	1.0	26	−0.114	0.033
40	306	13	1.0	31	−0.090	0.059
43	45.5	12.7	0.0	30	0.292	0.131
44	45	12.7	0.0	3	0.411	0.074
45	57	12.7	0.0	9	0.356	0.094
46	362	12.7	0.0	6	−0.181	0.046
47	83	12.7	0.0	7	0.149	0.099
48	553	12.7	0.0	6	−0.195	0.093
49	108	12.7	0.0	7	−0.100	0.103
50	679	12.7	0.0	49	−0.443	0.109
51	159	12.7	0.0	5	0.050	0.054
52	1823	12.7	0.0	45	−0.726	0.174
53	235	12.7	0.0	3	0.009	0.018
54	273	12.7	0.0	4	−0.030	0.017
55	5	12.7	0.0	17	0.045	0.222
56	322	12.7	0.0	10	−0.433	0.102
57	513	12.7	0.0	6	−0.455	0.089
58	640	12.7	0.0	5	−0.509	0.119
59	195	12.7	0.0	7	−0.083	0.054
60	45	19	0.0	1	0.320	—
63	64	28	0.0	1	0.199	—

With this disclaimer, all of the analytic and fitted models are discarded. Examination of figures 7(a)–(i) shows that none of these models exhibit a clustering† around the equality line within ±10% that would lead to a recommendation. In fact, none lead to a complete clustering within ±50%. This result is not altered by considering only subcooled or two-phase inlet or longer or shorter length experiments.‡ Examination of figures 9(a) and 10(a) (the Elias–Chambré model) on which is plotted only part of the Sozzi & Sutherland data (table 11 cases 43–54 containing 487 experimental data points) shows a much better clustering around the equality line, and figure 9(b) and (c) for the Richter and GSL models (same Sozzi & Sutherland data base) show very good clustering with an unfortunate bias towards overpredicting critical flow rates. Finally figure 9(d) for the GSL model, contains the entire Table 11 database (712 experimental points); the clustering remains good over the entire range 5×10^3–80×10^3 kg/m^2 s. We have then two candidates for recommendation: the Richter model (or Dobran 1987) and the GSL model. Further validation efforts must be carried out before the Elias–Chambré model can be recommended. These recommendations can be refined: the Richter model is a little better for two-phase inlet conditions, and the GSL model is better for subcooled inlet conditions.

†These figures contain all the data from table 6 (704 data points).

‡The comparison of models strictly within their proposed development ranges (Henry–Fauske for $L/D < 50$ for instance) does *not* alter these perceptions. If the data are accepted as valid the conclusion follows that the models do not generally fit the physics of the real world.

Table 17(c). Predictions of all the data in table 6 using the fit to the isoenthalpic model

Case	L (mm)	D (mm)	$\cos\theta$	N-data	Mean $\left\langle \frac{G_m - G_c}{G_m} \right\rangle$	SD $\left\langle \left(\frac{G_m - G_c}{G_m} \right)^2 \right\rangle$
1	1015	26.3	0.0	31	0.391	0.136
2	152	38	0.0	5	−5.144	1.563
4	305	38	0.0	6	−5.329	2.180
5	152	51	0.0	6	−4.711	1.917
6	305	51	0.0	5	−6.431	2.263
7	406	51	0.0	6	−6.086	2.459
8	305	76	0.0	5	−7.156	2.064
9	610	76	0.0	6	−6.743	2.610
10	406	51	0.0	4	−5.738	2.255
11	533	51	0.0	6	−8.833	4.625
12	500	12	0.0	10	−0.042	0.063
13	1600	30	0.0	5	−0.167	0.241
14	1700	50	0.0	6	0.088	0.073
18	13	44	0.0	92	−0.105	0.049
19	2674	14	1.0	5	0.769	0.009
20	2674	14	1.0	2	0.339	0.033
31	463	20	1.0	15	−0.023	0.079
32	463	20	1.0	71	0.096	0.116
38	2335	20	1.0	28	−0.777	0.196
39	306	13	1.0	26	−0.177	0.199
40	306	13	1.0	31	−0.330	0.354
43	45	12.7	0.0	30	0.350	0.180
44	45	12.7	0.0	3	0.456	0.095
45	57	12.7	0.0	9	0.385	0.087
46	362	12.7	0.0	6	−0.115	0.043
47	83	12.7	0.0	7	0.194	0.119
48	553	12.7	0.0	6	−0.117	0.098
49	108	12.7	0.0	7	0.153	0.124
50	679	12.7	0.0	49	−0.342	0.131
51	159	12.7	0.0	5	0.121	0.104
52	1823	12.7	0.0	45	−0.629	0.242
53	235	12.7	0.0	3	0.069	0.029
54	273	12.7	0.0	4	0.124	0.042
55	5	12.7	0.0	17	0.076	0.258
56	322	12.7	0.0	10	−0.242	0.101
57	513	12.7	0.0	6	−0.367	0.092
58	640	12.7	0.0	5	−0.394	0.099
59	195	12.7	0.0	7	0.016	0.043
60	45	19	0.0	1	0.464	—
63	64	28	0.0	1	0.245	—

Unfortunately the implementation of these models into a systems code will be difficult to nearly impossible. These are five and six equation models and could only be matched to system codes containing the same number of equations. Further, unless the models are somehow converted to fits, they will need to be solved as a function of distance. That is, these models become the fundamental equation set of the code and critical flow prediction is a natural consequence arising from the solution of the equation set. Moreover, the capability of any of these models to predict the Marviken data is severely limited. It is not that the models cannot be modified so as to produce reasonable agreement with the data. It is simply that as they were published none of the models provide a decent prediction of the Marviken experiments.

The above calculations and interpretations leave us in a difficult situation. For upflow and horizontal flow through exit geometries with diameters less than about 0.05 m the experimental data can be consistently predicted by existing models (Richter, GSL), but we have found no evidence that any existing model (certainly none we have examined) can adequately predict the Marviken downflow data (which to our knowledge is the only large diameter critical flow data). This indicates to us that direct best estimate calculations of large break situations are unreliable and can only be interpreted through an analysis which includes an uncertainty in the critical flow model. We also believe that further data need to be taken in downflow at small to medium diameters.

Table 17(d). Predictions of all the data in table 6 using the Moody model

Case	L (mm)	D (mm)	$\cos\theta$	N-data	Mean $\left\langle \frac{G_m - G_c}{G_m} \right\rangle$	SD $\left\langle \left(\frac{G_m - G_c}{G_m} \right)^2 \right\rangle$
1	1015	26.3	0.0	31	0.215	0.238
2	152	38	0.0	5	−4.481	1.528
4	305	38	0.0	6	−4.704	1.969
5	152	51	0.0	6	−4.131	1.721
6	305	51	0.0	5	−5.666	2.242
7	406	51	0.0	6	−5.398	2.258
8	305	76	0.0	5	−6.297	2.058
9	610	76	0.0	6	−6.004	2.425
10	406	51	0.0	4	−5.051	1.854
11	533	51	0.0	6	−7.861	4.280
12	500	12	0.0	10	−0.188	0.110
13	1600	30	0.0	5	−0.409	0.170
14	1700	50	0.0	6	−0.035	0.078
18	13	44	0.0	92	−0.029	0.029
19	2674	14	1.0	5	0.405	0.001
20	2674	14	1.0	2	0.024	0.088
31	463	20	1.0	15	−0.120	0.018
32	463	20	1.0	71	−0.079	0.093
38	2335	20	1.0	28	−0.657	0.108
39	306	13	1.0	26	−0.128	0.035
40	306	13	1.0	31	−0.094	0.055
43	45	12.7	0.0	30	0.262	0.097
44	45	12.7	0.0	3	0.397	0.059
45	57	12.7	0.0	9	0.326	0.033
46	362	12.7	0.0	6	−0.211	0.089
47	83	12.7	0.0	7	0.146	0.079
48	553	12.7	0.0	6	−0.239	0.084
49	108	12.7	0.0	7	0.083	0.069
50	679	12.7	0.0	49	−0.475	0.138
51	159	12.7	0.0	5	0.033	0.033
52	1823	12.7	0.0	45	−0.744	0.167
53	235	12.7	0.0	3	−0.008	0.061
54	273	12.7	0.0	4	−0.114	0.018
55	5	12.7	0.0	17	0.040	0.206
56	322	12.7	0.0	10	−0.517	0.167
57	513	12.7	0.0	6	−0.480	0.139
58	640	12.7	0.0	5	−0.578	0.192
59	195	12.7	0.0	7	−0.131	0.098
60	45	19	0.0	1	0.253	—
63	64	28	0.0	1	0.131	—

Table 17(e). Predictions of all the data in table 6 using the fit to the Moody model

Case	L (mm)	D (mm)	$\cos\theta$	N-data	Mean $\left\langle \frac{G_m - G_c}{G_m} \right\rangle$	SD $\left\langle \left(\frac{G_m - G_c}{G_m} \right)^2 \right\rangle$
1	1015	26.3	0.0	31	0.230	0.238
2	152	38	0.0	5	−4.882	3.191
4	305	38	0.0	6	−4.985	3.626
5	152	51	0.0	6	−4.010	2.396
6	305	51	0.0	5	−6.352	4.723
7	406	51	0.0	6	−5.810	4.383
8	305	76	0.0	5	−6.872	4.517
9	610	76	0.0	6	−6.494	4.940
10	406	51	0.0	4	−4.568	2.285
11	533	51	0.0	6	−8.579	7.374
12	500	12	0.0	10	−0.170	0.161
13	1600	30	0.0	5	−0.389	0.128
14	1700	50	0.0	6	−0.001	0.126
18	13	44	0.0	92	−0.280	0.395
19	2674	14	1.0	5	0.407	0.001
20	2674	14	1.0	2	−0.057	0.094
31	463	20	1.0	15	−0.014	0.132
32	463	20	1.0	71	−0.010	0.165
38	2335	20	1.0	28	−0.498	0.248
39	306	13	1.0	26	−0.024	0.128
40	306	13	1.0	31	−0.026	0.109
43	45	12.7	0.0	30	0.338	0.041
44	45	12.7	0.0	3	0.427	0.028
45	57	12.7	0.0	9	0.370	0.029
46	362	12.7	0.0	6	−0.154	0.166
47	83	12.7	0.0	7	0.233	0.019
48	553	12.7	0.0	6	−0.192	0.110
49	108	12.7	0.0	7	0.148	0.026
50	679	12.7	0.0	49	−0.330	0.232
51	159	12.7	0.0	5	0.056	0.043
52	1823	12.7	0.0	45	−0.531	0.197
53	235	12.7	0.0	3	0.011	0.096
54	273	12.7	0.0	4	−0.131	0.018
55	5	12.7	0.0	17	0.201	0.062
56	322	12.7	0.0	10	−0.500	0.226
57	513	12.7	0.0	6	−0.364	0.252
58	640	12.7	0.0	5	−0.509	0.317
59	195	12.7	0.0	7	−0.134	0.113
60	45	19	0.0	1	0.244	—
63	64	28	0.0	1	0.116	—

Table 17(f). Predictions of all the data in table 6 using the Henry–Fauske model

Case	L (mm)	D (mm)	$\cos\theta$	N-data	Mean $\left\langle \frac{G_m - G_c}{G_m} \right\rangle$	SD $\left\langle \left(\frac{G_m - G_c}{G_m} \right)^2 \right\rangle$
1	1015	26.3	0.0	31	0.065	0.223
2	152	38	0.0	5	−4.453	1.478
4	305	38	0.0	6	−4.691	1.892
5	152	51	0.0	6	−4.125	1.662
6	305	51	0.0	5	−5.618	2.169
7	406	51	0.0	6	−5.384	2.176
8	305	76	0.0	5	−6.251	1.985
9	610	76	0.0	6	−5.986	2.328
10	406	51	0.0	4	−5.058	1.760
11	533	51	0.0	6	−7.837	4.162
12	500	12	0.0	10	−0.500	0.172
13	1600	30	0.0	5	−0.752	0.157
14	1700	50	0.0	6	−0.286	0.121
18	13	44	0.0	92	−0.018	0.025
19	2674	14	1.0	5	0.350	0.002
20	2674	14	1.0	2	−0.154	0.105
31	463	20	1.0	15	−0.282	0.131
32	463	20	1.0	71	−0.289	0.164
38	2335	20	1.0	28	−0.840	0.264
39	306	13	1.0	26	−0.240	0.123
40	306	13	1.0	31	−0.251	0.121
43	45	12.7	0.0	30	0.138	0.052
44	45	12.7	0.0	3	0.258	0.031
45	57	12.7	0.0	9	0.178	0.029
46	362	12.7	0.0	6	−0.500	0.176
47	83	12.7	0.0	7	−0.013	0.040
48	553	12.7	0.0	6	−0.541	0.108
49	108	12.7	0.0	7	−0.114	0.032
50	679	12.7	0.0	49	−0.742	0.233
51	159	12.7	0.0	5	−0.218	0.034
52	1823	12.7	0.0	45	−1.026	0.192
53	235	12.7	0.0	3	−0.280	0.099
54	273	12.7	0.0	4	−0.414	0.021
55	5	12.7	0.0	17	−0.064	0.116
56	322	12.7	0.0	10	−0.839	0.227
57	513	12.7	0.0	6	−0.787	0.273
58	640	12.7	0.0	5	−0.947	0.351
59	195	12.7	0.0	7	−0.446	0.113
60	45	19	0.0	1	0.065	—
63	64	28	0.0	1	−0.152	—

Table 17(g). Predictions of all the data in table 6 using the fit to the Henry–Fauske model

Case	L (mm)	D (mm)	$\cos\theta$	N-data	Mean $\left\langle \frac{G_m - G_c}{G_m} \right\rangle$	SD $\left\langle \left(\frac{G_m - G_c}{G_m} \right)^2 \right\rangle$
1	1015	26.3	0.0	31	0.228	0.250
2	152	38	0.0	5	−4.320	1.515
4	305	38	0.0	6	−4.560	1.891
5	152	51	0.0	6	−3.925	1.537
6	305	51	0.0	5	−5.472	2.258
7	406	51	0.0	6	−5.244	2.202
8	305	76	0.0	5	−6.077	2.072
9	610	76	0.0	6	−5.844	2.389
10	406	51	0.0	4	−4.872	1.645
11	533	51	0.0	6	−7.633	4.186
12	500	12	0.0	10	−0.485	0.158
13	1600	30	0.0	5	−0.747	0.170
14	1700	50	0.0	6	−0.277	0.099
18	13	44	0.0	92	0.008	0.067
19	2674	14	1.0	5	0.412	0.003
20	2674	14	1.0	2	−0.029	0.095
31	463	20	1.0	15	−0.308	0.116
32	463	20	1.0	71	−0.282	0.118
38	2335	20	1.0	28	−0.794	0.228
39	306	13	1.0	26	−0.241	0.093
40	306	13	1.0	31	−0.239	0.104
43	44.5	12.7	0.0	30	0.019	0.229
44	45	12.7	0.0	3	0.248	0.036
45	57	12.7	0.0	9	0.169	0.036
46	362	12.7	0.0	6	−0.522	0.157
47	83	12.7	0.0	7	−0.037	0.053
48	553	12.7	0.0	6	−0.560	0.091
49	108	12.7	0.0	7	−0.133	0.045
50	679	12.7	0.0	49	−0.771	0.199
51	159	12.7	0.0	5	−0.233	0.035
52	1823	12.7	0.0	45	−1.069	0.168
53	235	12.7	0.0	3	−0.298	0.085
54	273	12.7	0.0	4	−0.405	0.025
55	5	12.7	0.0	17	−0.104	0.141
56	322	12.7	0.0	10	−0.894	0.204
57	513	12.7	0.0	6	−0.816	0.246
58	640	12.7	0.0	5	−0.964	0.322
59	195	12.7	0.0	7	−0.454	0.091
60	45	19	0.0	1	0.082	—
63	64	28	0.0	1	−0.112	—

Table 17(h). Predictions of all the data in table 6 using the HEM model

Case	L (mm)	D (mm)	$\cos\theta$	N-data	Mean $\left\langle \frac{G_m - G_c}{G_m} \right\rangle$	SD $\left\langle \left(\frac{G_m - G_c}{G_m} \right)^2 \right\rangle$
1	1015	26.3	0.0	31	0.762	0.124
2	152	38	0.0	5	−4.492	1.527
4	305	38	0.0	6	−4.702	1.966
5	152	51	0.0	6	−4.132	1.721
6	305	51	0.0	5	−5.663	2.232
7	406	51	0.0	6	−5.401	2.262
8	305	76	0.0	5	−6.300	2.058
9	610	76	0.0	6	−6.005	2.424
10	406	51	0.0	4	−5.050	1.850
11	533	51	0.0	6	−7.864	4.276
12	500	12	0.0	10	−0.053	0.057
13	1600	30	0.0	5	−0.144	0.279
14	1700	50	0.0	6	0.083	0.096
18	13	44	0.0	92	−0.029	0.029
19	2674	14	1.0	5	0.825	0.003
20	2674	14	1.0	2	0.594	0.040
31	463	20	1.0	15	−0.039	0.104
32	463	20	1.0	71	−0.074	0.125
38	2335	20	1.0	28	−0.680	0.120
39	306	13	1.0	26	−0.112	0.033
40	306	13	1.0	31	−0.089	0.059
43	45	12.7	0.0	30	0.340	0.176
44	45	12.7	0.0	3	0.455	0.120
45	57	12.7	0.0	9	0.376	0.103
46	362	12.7	0.0	6	−0.120	0.073
47	83	12.7	0.0	7	−0.180	0.140
48	553	12.7	0.0	6	−0.117	0.130
49	108	12.7	0.0	7	0.143	0.149
50	679	12.7	0.0	49	−0.344	0.150
51	159	12.7	0.0	5	0.108	0.126
52	1823	12.7	0.0	45	−0.648	0.239
53	235	12.7	0.0	3	0.065	0.066
54	273	12.7	0.0	4	0.180	0.033
55	5	12.7	0.0	17	0.073	0.250
56	322	12.7	0.0	10	−0.236	0.112
57	513	12.7	0.0	6	−0.382	0.124
58	640	12.7	0.0	5	−0.373	0.124
59	195	12.7	0.0	7	0.026	0.075
60	45	19	0.0	1	0.481	—
63	64	28	0.0	1	0.325	—

Table 18(a). Predictions of all the two-phase inlet data in table 6 using the Burnell model

Case	L (mm)	D (mm)	$\cos\theta$	N-data	Mean $\left\langle \frac{G_m - G_c}{G_m} \right\rangle$	SD $\left\langle \left(\frac{G_m - G_c}{G_m} \right)^2 \right\rangle$
19	2674	14	1.0	8	−0.152	0.078
20	2674	14	1.0	22	−0.291	0.205
32	463	20	1.0	2	−0.267	0.532
43	45	12.7	0.0	99	−0.122	0.145
44	45	12.7	0.0	10	0.098	0.078
45	57	12.7	0.0	38	−0.087	0.084
46	362	12.7	0.0	13	−0.654	0.312
47	83	12.7	0.0	10	−0.265	0.135
48	553	12.7	0.0	7	−0.900	0.040
49	108	12.7	0.0	16	−0.406	0.056
50	679	12.7	0.0	47	−0.906	0.084
51	159	12.7	0.0	10	−0.486	0.086
52	1823	12.7	0.0	36	−1.306	0.095
53	235	12.7	0.0	9	−0.563	0.090
54	273	12.7	0.0	18	−0.640	0.084
55	5	12.7	0.0	41	−0.022	0.080
56	322	12.7	0.0	14	−0.849	0.025
57	513	12.7	0.0	18	−0.905	0.024
58	640	12.7	0.0	12	−0.994	0.048
59	195	12.7	0.0	16	−0.721	0.070
60	45	19	0.0	22	−0.234	0.088
61	732	54	0.0	4	−0.477	0.030
62	696	76	0.0	3	−0.593	0.043
63	63	28	0.0	3	−0.249	0.143

Table 18(b). Predictions of all the two-phase inlet data in table 6 using the isenthalpic model

Case	L (mm)	D (mm)	$\cos\theta$	N-data	Mean $\left\langle \frac{G_m - G_c}{G_m} \right\rangle$	SD $\left\langle \left(\frac{G_m - G_c}{G_m} \right)^2 \right\rangle$
19	2674	14	1.0	8	0.766	0.043
20	2674	14	1.0	22	0.598	0.089
32	463	20	1.0	2	0.188	0.100
43	45	12.7	0.0	99	0.378	0.104
44	45	12.7	0.0	10	0.478	0.053
45	57	12.7	0.0	38	0.368	0.054
46	362	12.7	0.0	13	0.038	0.154
47	83	12.7	0.0	10	0.271	0.088
48	553	12.7	0.0	7	−0.088	0.035
49	108	12.7	0.0	16	0.179	0.042
50	679	12.7	0.0	47	−0.120	0.051
51	159	12.7	0.0	10	0.146	0.066
52	1823	12.7	0.0	36	−1.347	0.062
53	235	12.7	0.0	9	0.081	0.059
54	273	12.7	0.0	18	0.041	0.058
55	5	12.7	0.0	41	0.416	0.060
56	322	12.7	0.0	14	−0.079	0.022
57	513	12.7	0.0	18	−0.115	0.018
58	640	12.7	0.0	12	−0.165	0.031
59	195	12.7	0.0	16	0.521	0.042
60	45	19	0.0	22	0.279	0.057
61	732	54	0.0	4	0.124	0.026
62	696	76	0.0	3	0.045	0.035
63	63	28	0.0	3	0.267	0.090

Table 18(c). Predictions of all the two-phase inlet data in table 6 using the fit to the isenthalpic model

Case	L (mm)	D (mm)	$\cos\theta$	N-data	Mean $\left\langle \frac{G_m - G_c}{G_m} \right\rangle$	SD $\left\langle \left(\frac{G_m - G_c}{G_m} \right)^2 \right\rangle$
19	2674	14	1.0	8	136.8	28.14
20	2674	14	1.0	22	99.42	67.10
32	463	20	1.0	2	0.163	0.107
43	45	12.7	0.0	99	0.361	0.109
44	45	12.7	0.0	10	0.462	0.055
45	57	12.7	0.0	38	0.350	0.056
46	362	12.7	0.0	13	−0.031	0.043
47	83	12.7	0.0	10	0.250	0.092
48	553	12.7	0.0	7	−0.117	0.037
49	108	12.7	0.0	16	0.155	0.044
50	679	12.7	0.0	47	−0.152	0.053
51	159	12.7	0.0	10	0.122	0.068
52	1823	12.7	0.0	36	−0.385	0.065
53	235	12.7	0.0	9	0.054	0.061
54	273	12.7	0.0	18	0.013	0.060
55	5	12.7	0.0	41	0.404	0.065
56	322	12.7	0.0	14	−0.109	0.023
57	513	12.7	0.0	18	−0.146	0.019
58	640	12.7	0.0	12	−0.197	0.031
59	195	12.7	0.0	16	0.028	0.044
60	45	19	0.0	22	0.256	0.060
61	732	54	0.0	4	0.097	0.026
62	696	76	0.0	3	0.014	0.035
63	63	28	0.0	3	0.247	0.094

Table 18(d). Predictions of all the two-phase inlet data in table 6 using the Moody model

Case	L (mm)	D (mm)	$\cos\theta$	N-data	Mean $\left\langle \frac{G_m - G_c}{G_m} \right\rangle$	SD $\left\langle \left(\frac{G_m - G_c}{G_m} \right)^2 \right\rangle$
19	2674	14	1.0	8	0.162	0.171
20	2674	14	1.0	22	−0.204	0.252
32	463	20	1.0	2	−0.162	0.521
43	45	12.7	0.0	99	0.247	0.149
44	45	12.7	0.0	10	0.197	0.083
45	57	12.7	0.0	38	0.327	0.085
46	362	12.7	0.0	13	−0.479	0.200
47	83	12.7	0.0	10	−0.114	0.133
48	553	12.7	0.0	7	−0.658	0.044
49	108	12.7	0.0	16	−0.252	0.061
50	679	12.7	0.0	47	−0.693	0.075
51	159	12.7	0.0	10	−0.305	0.093
52	1823	12.7	0.0	36	−0.104	0.097
53	235	12.7	0.0	9	−0.398	0.088
54	273	12.7	0.0	18	−0.458	0.088
55	5	12.7	0.0	41	0.097	0.084
56	322	12.7	0.0	14	−0.636	0.028
57	513	12.7	0.0	18	−0.689	0.023
58	640	12.7	0.0	12	−0.761	0.036
59	195	12.7	0.0	16	−0.521	0.068
60	45	19	0.0	22	−0.123	0.095
61	732	54	0.0	4	−0.342	0.026
62	696	76	0.0	3	−0.480	0.035
63	63	28	0.0	3	−0.104	0.141

Table 18(e). Predictions of all the two-phase inlet data in table 6 using the fit to the Moody model

Case	L (mm)	D (mm)	$\cos\theta$	N-data	Mean $\left\langle \frac{G_m - G_c}{G_m} \right\rangle$	SD $\left\langle \left(\frac{G_m - G_c}{G_m} \right)^2 \right\rangle$
19	2674	14	1.0	8	0.177	0.162
20	2674	14	1.0	22	−0.186	0.246
32	463	20	1.0	2	−0.169	0.048
43	45	12.7	0.0	99	0.178	0.148
44	45	12.7	0.0	10	0.192	0.082
45	57	12.7	0.0	38	0.027	0.085
46	362	12.7	0.0	13	−0.489	0.201
47	83	12.7	0.0	10	−0.121	0.133
48	553	12.7	0.0	7	−0.670	0.043
49	108	12.7	0.0	16	−0.258	0.061
50	679	12.7	0.0	47	−0.703	0.757
51	159	12.7	0.0	10	−0.314	0.092
52	1823	12.7	0.0	36	−1.048	0.097
53	235	12.7	0.0	9	−0.405	0.087
54	273	12.7	0.0	18	−0.466	0.088
55	5	12.7	0.0	41	0.092	0.083
56	322	12.7	0.0	14	−0.646	0.028
57	513	12.7	0.0	18	−0.699	0.022
58	640	12.7	0.0	12	−0.771	0.037
59	195	12.7	0.0	16	−0.530	0.067
60	45	19	0.0	22	−0.127	0.094
61	732	54	0.0	4	−0.347	0.027
62	696	76	0.0	3	−0.483	0.036
63	63	28	0.0	3	−0.111	0.141

Table 18(f). Predictions of all the two-phase inlet data in table 6 using the Henry–Fauske model

Case	L (mm)	D (mm)	$\cos\theta$	N-data	Mean $\left\langle \frac{G_m - G_c}{G_m} \right\rangle$	SD $\left\langle \left(\frac{G_m - G_c}{G_m} \right)^2 \right\rangle$
19	2674	14	1.0	8	0.218	0.065
20	2674	14	1.0	22	0.015	0.182
32	463	20	1.0	2	−0.422	0.035
43	45	12.7	0.0	99	−0.163	0.158
44	45	12.7	0.0	10	0.049	0.079
45	57	12.7	0.0	38	−0.140	0.099
46	362	12.7	0.0	13	−0.843	0.042
47	83	12.7	0.0	10	−0.342	0.142
48	553	12.7	0.0	7	−1.022	0.045
49	108	12.7	0.0	16	−0.492	0.058
50	679	12.7	0.0	47	−1.039	0.093
51	159	12.7	0.0	10	−0.576	0.096
52	1823	12.7	0.0	36	−1.470	0.094
53	235	12.7	0.0	9	−0.662	0.097
54	273	12.7	0.0	18	−0.745	0.084
55	5	12.7	0.0	41	−0.070	0.083
56	322	12.7	0.0	14	−0.973	0.030
57	513	12.7	0.0	18	−1.035	0.031
58	640	12.7	0.0	12	−1.135	0.063
59	195	12.7	0.0	16	−0.831	0.067
60	45	19	0.0	22	−0.283	0.084
61	732	54	0.0	4	−0.557	0.045
62	696	76	0.0	3	−0.659	0.061
63	63	28	0.0	3	−0.340	0.146

Table 18(g). Predictions of all the two-phase inlet data in table 6 using the fit to the Henry–Fauske model

Case	L (mm)	D (mm)	$\cos\theta$	N-data	Mean $\left\langle \frac{G_m - G_e}{G_m} \right\rangle$	SD $\left\langle \left(\frac{G_m - G_e}{G_m} \right)^2 \right\rangle$
19	2674	14	1.0	8	0.206	0.144
20	2674	14	1.0	22	−0.096	0.187
32	463	20	1.0	2	−0.360	0.051
43	45	12.7	0.0	99	−0.123	0.169
44	45	12.7	0.0	10	0.074	0.088
45	57	12.7	0.0	38	−0.118	0.092
46	362	12.7	0.0	13	−0.625	0.567
47	83	12.7	0.0	10	−0.295	0.148
48	553	12.7	0.0	7	−0.938	0.050
49	108	12.7	0.0	16	−0.450	0.066
50	679	12.7	0.0	47	−0.971	0.088
51	159	12.7	0.0	10	−0.519	0.103
52	1823	12.7	0.0	36	−1.377	0.103
53	235	12.7	0.0	9	−0.618	0.099
54	273	12.7	0.0	18	−0.692	0.094
55	5	12.7	0.0	41	−0.037	0.093
56	322	12.7	0.0	14	−0.905	0.031
57	513	12.7	0.0	18	−0.966	0.027
58	640	12.7	0.0	12	−1.055	0.050
59	195	12.7	0.0	16	−0.769	0.072
60	45	19	0.0	22	−0.274	0.096
61	732	54	0.0	4	−0.536	0.038
62	696	76	0.0	3	−0.664	0.052
63	63	28	0.0	3	−0.290	0.155

Table 18(h). Predictions of all the two-phase inlet data in table 6 using the HEM model

Case	L (mm)	D (mm)	$\cos\theta$	N-data	Mean $\left\langle \frac{G_m - G_e}{G_m} \right\rangle$	SD $\left\langle \left(\frac{G_m - G_e}{G_m} \right)^2 \right\rangle$
19	2674	14	1.0	8	0.766	0.043
20	2674	14	1.0	22	0.597	0.089
32	463	20	1.0	2	0.167	0.113
43	45	12.7	0.0	99	0.370	0.106
44	45	12.7	0.0	10	0.470	0.054
45	57	12.7	0.0	38	0.359	0.055
46	362	12.7	0.0	13	0.024	0.157
47	83	12.7	0.0	10	0.260	0.090
48	553	12.7	0.0	7	−0.104	0.037
49	108	12.7	0.0	16	0.167	0.043
50	679	12.7	0.0	47	−0.137	0.052
51	159	12.7	0.0	10	0.133	0.067
52	1823	12.7	0.0	36	−0.368	0.063
53	235	12.7	0.0	9	0.067	0.060
54	273	12.7	0.0	18	0.026	0.059
55	5	12.7	0.0	41	0.412	0.062
56	322	12.7	0.0	14	−0.095	0.023
57	513	12.7	0.0	18	−0.132	0.019
58	640	12.7	0.0	12	−0.183	0.032
59	195	12.7	0.0	16	−0.129	0.351
60	45	19	0.0	22	0.268	0.058
61	732	54	0.0	4	0.111	0.027
62	696	76	0.0	3	0.031	0.036
63	63	28	0.0	3	0.256	0.092

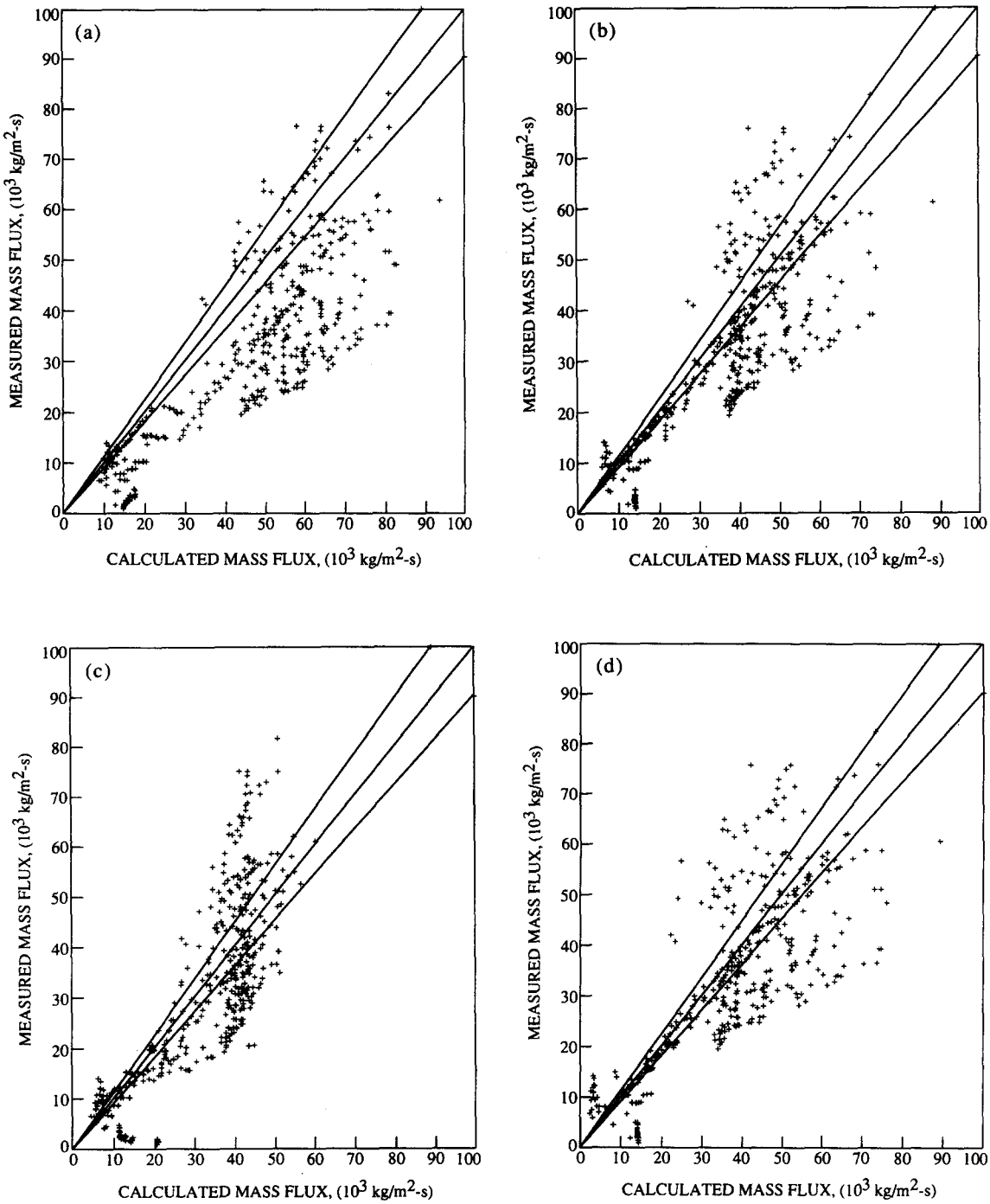

Figure 7 (a)–(d). *Caption overleaf.*

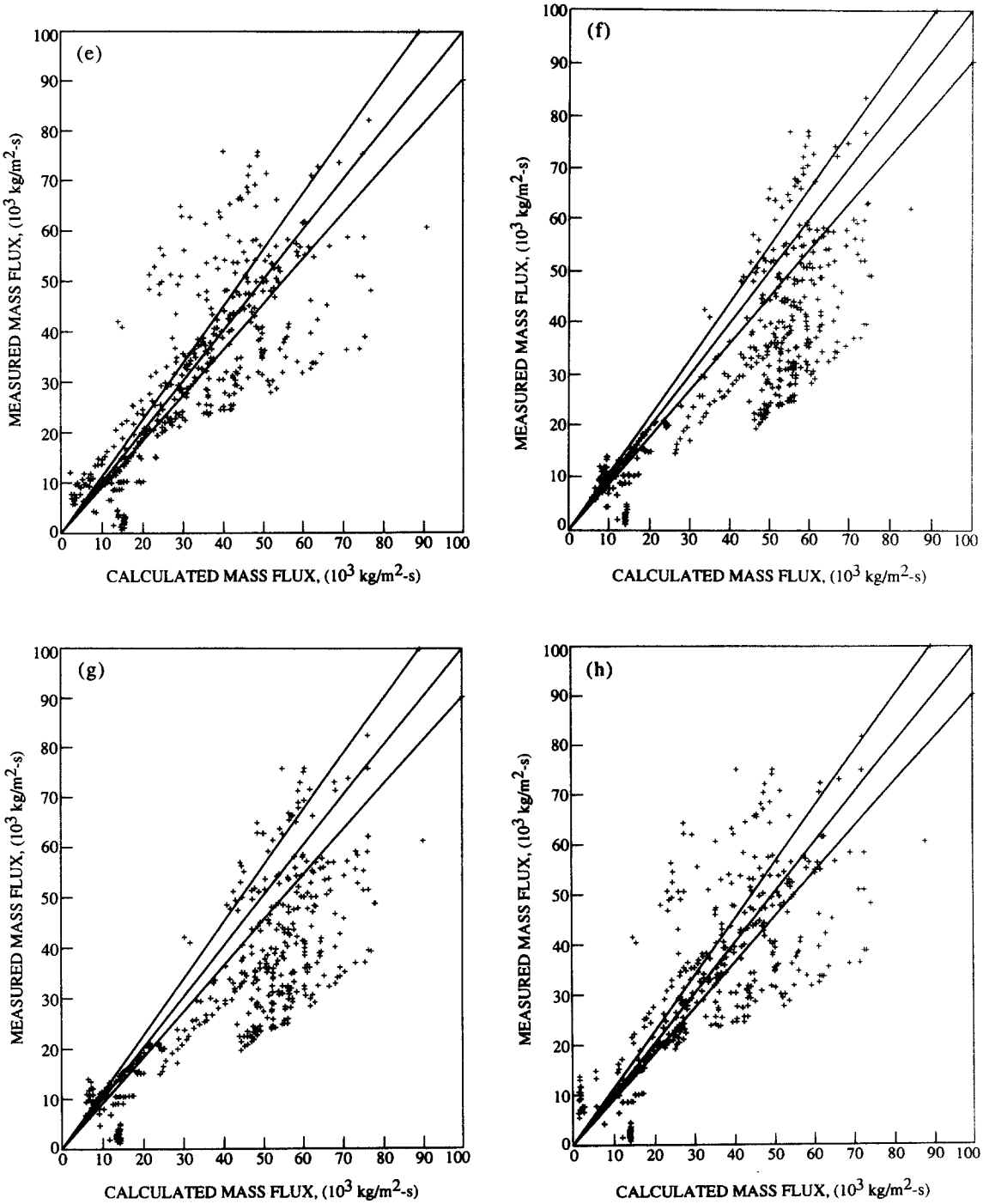

Figure 7 (e)–(h)

Figure 7. Comparison with experiments listed in table 6 for subcooled inlet conditions: (a) Burnell model; (b) Moody model with slip; (c) fit to the Moody model with slip; (d) isenthalpic model; (e) fit to the isenthalpic model; (f) Henry–Fauske model; (g) fit to the Henry–Fauske model; and (h) the HEM model.

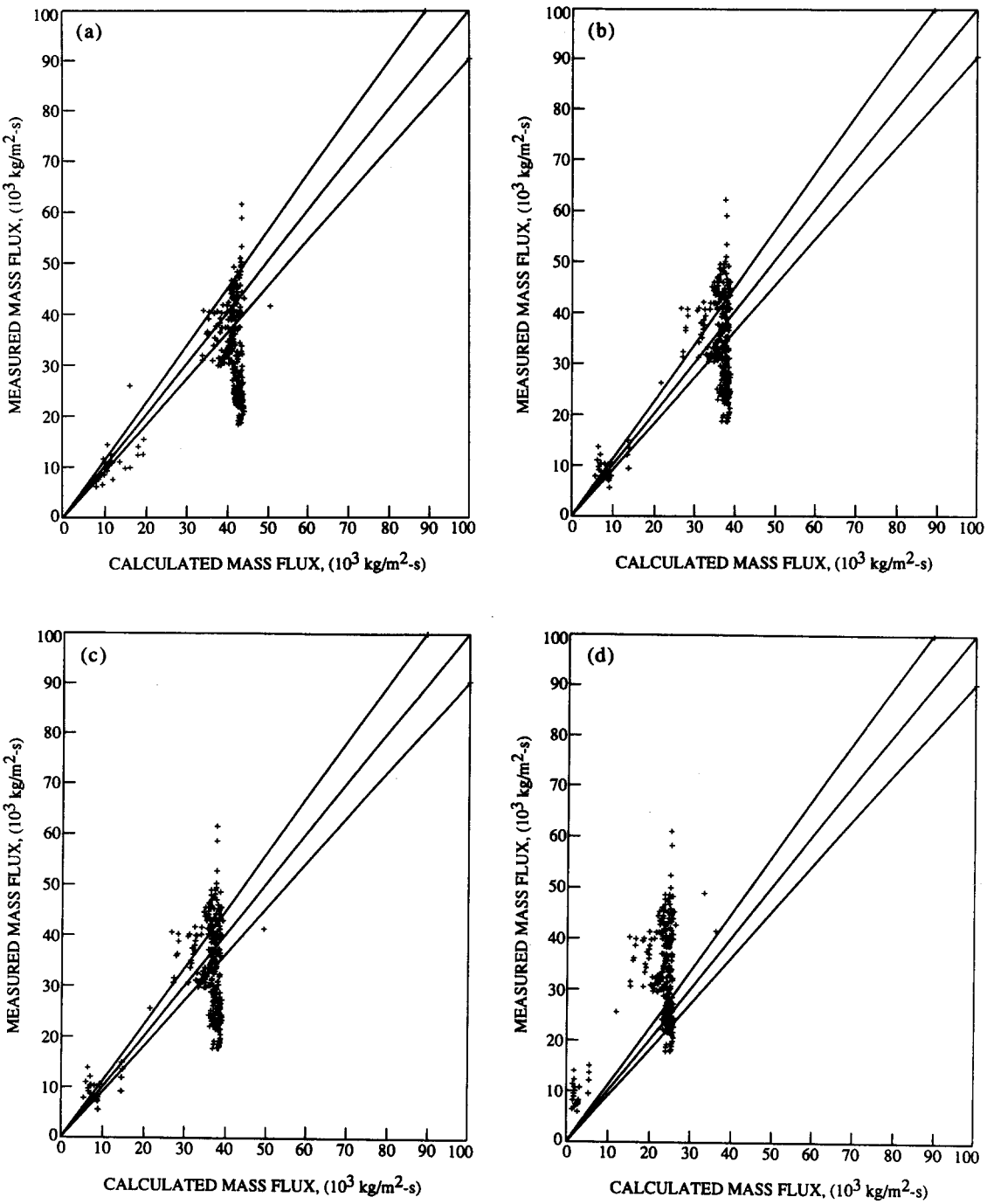

Figure 8 (a)–(d). *Caption overleaf.*

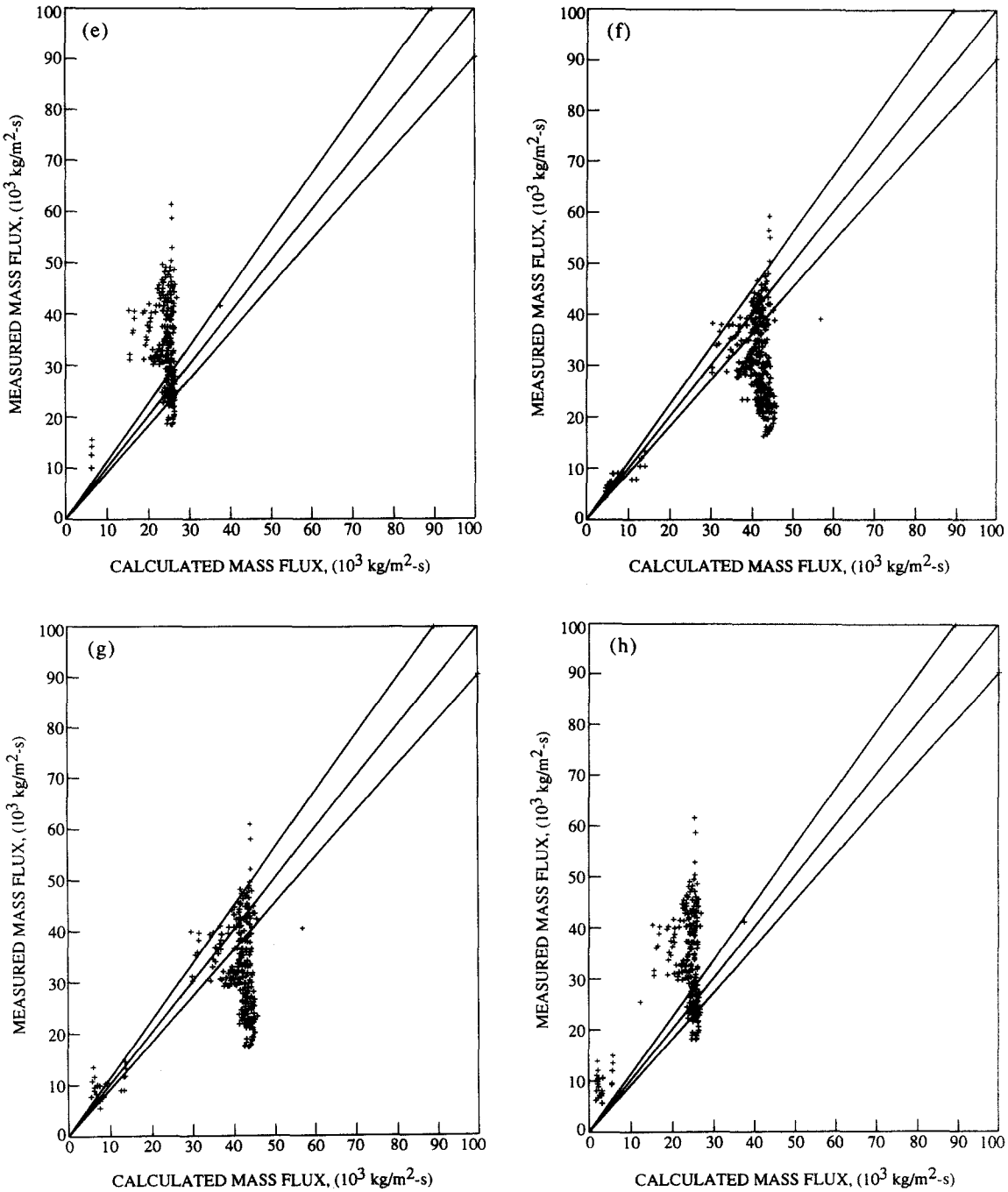

Figure 8(e)–(h)

Figure 8. Comparison with experiments listed in table 6 for two-phase inlet conditions: (a) Burnell model; (b) Moody model with slip; (c) fit to the Moody model with slip; (d) isenthalpic model; (e) fit to the isenthalpic model; (f) Henry–Fauske model; (g) fit to the Henry–Fauske model; and (h) the HEM model.

Table 19(a). Predictions of the Sozzi & Sutherland data using the Elias–Chambré model

Case	L (mm)	D (mm)	$\cos\theta$	N-data	Mean $\left\langle \frac{G_m - G_c}{G_m} \right\rangle$	SD $\left\langle \left(\frac{G_m - G_c}{G_m} \right)^2 \right\rangle$
43	45	12.7	0.0	129	−0.226	0.261
44	45	12.7	0.0	13	0.202	0.102
45	57	12.7	0.0	47	0.141	0.114
46	362	12.7	0.0	19	0.009	0.161
47	83	12.7	0.0	17	0.010	0.163
48	553	12.7	0.0	13	−0.025	0.123
49	108	12.7	0.0	23	−0.075	0.109
50	679	12.7	0.0	96	−0.125	0.068
51	159	12.7	0.0	15	−0.164	0.059
52	1823	12.7	0.0	81	0.023	0.064
53	235	12.7	0.0	12	−0.131	0.064
54	273	12.7	0.0	22	−0.149	0.056

Table 19(b). Predictions of the Sozzi & Sutherland data using the Richter model

Case	L (mm)	D (mm)	$\cos\theta$	N-data	Mean $\left\langle \frac{G_m - G_c}{G_m} \right\rangle$	SD $\left\langle \left(\frac{G_m - G_c}{G_m} \right)^2 \right\rangle$
43	45	12.7	0.0	129	−0.198	0.123
44	45	12.7	0.0	13	0.014	0.040
45	57	12.7	0.0	47	−0.002	0.052
46	362	12.7	0.0	19	−0.128	0.059
47	83	12.7	0.0	17	−0.092	0.069
48	553	12.7	0.0	13	−0.077	0.041
49	108	12.7	0.0	23	−0.128	0.044
50	679	12.7	0.0	96	−0.107	0.073
51	159	12.7	0.0	15	−0.113	0.074
52	1823	12.7	0.0	81	0.026	0.076
53	235	12.7	0.0	12	−0.079	0.066
54	273	12.7	0.0	22	−0.101	0.037

Table 19(c). Predictions of all the data in table 6 using the GSL model

Case	L (mm)	D (mm)	$\cos\theta$	N-data	Mean $\left\langle \frac{G_m - G_c}{G_m} \right\rangle$	SD $\left\langle \left(\frac{G_m - G_c}{G_m} \right)^2 \right\rangle$
1	1015	26.3	0.0	31	0.181	0.148
12	500	12	0.0	10	0.003	0.045
13	1600	30	0.0	5	−0.089	0.179
14	1700	50	0.0	6	0.108	0.041
43	45	12.7	0.0	129	−0.232	0.220
44	45	12.7	0.0	13	−0.126	0.126
45	57	12.7	0.0	47	−0.211	0.162
46	362	12.7	0.0	19	−0.174	0.059
47	83	12.7	0.0	17	−0.193	0.182
48	553	12.7	0.0	13	−0.065	0.062
49	108	12.7	0.0	23	−0.256	0.146
50	679	12.7	0.0	96	−0.107	0.066
51	159	12.7	0.0	15	−0.199	0.125
52	1823	12.7	0.0	81	−0.005	0.067
53	235	12.7	0.0	12	−0.169	0.109
54	273	12.7	0.0	22	−0.193	0.093
55	5	12.7	0.0	58	−0.154	0.076
56	322	12.7	0.0	24	−0.125	0.047
57	513	12.7	0.0	24	−0.069	0.045
58	640	12.7	0.0	17	−0.072	0.059
59	195	12.7	0.0	23	−0.082	0.102
60	45	19	0.0	23	−0.107	0.093

Table 20(a). Predictions of all the subcooled Sozzi & Sutherland data using the Elias–Chambré model

Case	L (mm)	D (mm)	$\cos\theta$	N-data	Mean $\left\langle \frac{G_m - G_c}{G_m} \right\rangle$	SD $\left\langle \left(\frac{G_m - G_c}{G_m} \right)^2 \right\rangle$
43	45	12.7	0.0	30	0.055	0.137
44	45	12.7	0.0	4	0.304	0.099
45	57	12.7	0.0	9	0.297	0.071
46	362	12.7	0.0	7	0.102	0.115
47	83	12.7	0.0	8	0.142	0.102
48	553	12.7	0.0	6	0.084	0.089
49	108	12.7	0.0	7	0.041	0.110
50	679	12.7	0.0	49	−0.152	0.072
51	159	12.7	0.0	5	−0.174	0.043
52	1823	12.7	0.0	45	0.023	0.080
53	235	12.7	0.0	3	−0.113	0.042
54	273	12.7	0.0	4	−0.099	0.032

Table 20(b). Predictions of all the subcooled Sozzi & Sutherland data using the Richter model

Case	L (mm)	D (mm)	$\cos\theta$	N-data	Mean $\left\langle \frac{G_m - G_c}{G_m} \right\rangle$	SD $\left\langle \left(\frac{G_m - G_c}{G_m} \right)^2 \right\rangle$
43	45	12.7	0.0	30	−0.107	0.080
44	45	12.7	0.0	4	0.004	0.031
45	57	12.7	0.0	9	0.027	0.037
46	362	12.7	0.0	7	−0.170	0.080
47	83	12.7	0.0	8	−0.108	0.054
48	553	12.7	0.0	6	−0.061	0.046
49	108	12.7	0.0	7	−0.157	0.061
50	679	12.7	0.0	49	−0.135	0.079
51	159	12.7	0.0	5	−0.164	0.053
52	1823	12.7	0.0	43	0.068	0.068
53	235	12.7	0.0	3	−0.129	0.044
54	273	12.7	0.0	4	−0.116	0.035

Table 20(c). Predictions of all the subcooled data in table 6 using the GSL model

Case	L (mm)	D (mm)	$\cos\theta$	N-data	Mean $\left\langle \frac{G_m - G_c}{G_m} \right\rangle$	SD $\left\langle \left(\frac{G_m - G_c}{G_m} \right)^2 \right\rangle$
1	1015	26.3	0.0	31	0.181	0.148
12	500	12	0.0	10	0.003	0.045
13	1600	30	0.0	5	−0.089	0.179
14	1700	50	0.0	6	0.108	0.041
43	45	12.7	0.0	30	−0.003	0.171
44	45	12.7	0.0	4	0.047	0.042
45	57	12.7	0.0	9	−0.077	0.035
46	362	12.7	0.0	7	−0.123	0.062
47	83	12.7	0.0	8	−0.022	0.036
48	553	12.7	0.0	6	−0.018	0.057
49	108	12.7	0.0	7	−0.052	0.039
50	679	12.7	0.0	49	−0.134	0.069
51	159	12.7	0.0	5	−0.057	0.034
52	1823	12.7	0.0	45	−0.009	0.082
53	235	12.7	0.0	3	−0.019	0.028
54	273	12.7	0.0	4	−0.045	0.024
55	5	12.7	0.0	18	−0.062	0.027
56	322	12.7	0.0	8	−0.126	0.076
57	513	12.7	0.0	6	−0.082	0.089
58	640	12.7	0.0	5	−0.086	0.107
59	195	12.7	0.0	8	0.049	0.046
60	45	19	0.0	1	0.157	0.025

Table 21(a). Predictions of the two-phase inlet Sozzi & Sutherland data using the Elias–Chambré model

Case	L (mm)	D (mm)	$\cos\theta$	N-data	Mean $\left\langle \frac{G_m - G_c}{G_m} \right\rangle$	SD $\left\langle \left(\frac{G_m - G_c}{G_m} \right)^2 \right\rangle$
43	45	12.7	0.0	99	−0.311	0.228
44	45	12.7	0.0	9	0.156	0.066
45	57	12.7	0.0	38	0.104	0.087
46	362	12.7	0.0	12	−0.045	0.164
47	83	12.7	0.0	9	−0.107	0.106
48	553	12.7	0.0	7	−0.119	0.035
49	108	12.7	0.0	16	−0.126	0.058
50	679	12.7	0.0	47	−0.098	0.052
51	159	12.7	0.0	10	−0.158	0.067
52	1823	12.7	0.0	36	0.023	0.036
53	235	12.7	0.0	9	−0.137	0.071
54	273	12.7	0.0	18	−0.160	0.055

Table 21(b). Predictions of the two-phase inlet Sozzi & Sutherland data using the Richter model

Case	L (mm)	D (mm)	$\cos\theta$	N-data	Mean $\left\langle \frac{G_m - G_c}{G_m} \right\rangle$	SD $\left\langle \left(\frac{G_m - G_c}{G_m} \right)^2 \right\rangle$
43	45	12.7	0.0	99	−0.225	0.121
44	45	12.7	0.0	9	0.018	0.044
45	57	12.7	0.0	38	−0.009	0.054
46	362	12.7	0.0	12	−0.103	0.019
47	83	12.7	0.0	9	−0.077	0.080
48	553	12.7	0.0	7	−0.090	0.033
49	108	12.7	0.0	16	−0.115	0.027
50	679	12.7	0.0	47	−0.078	0.052
51	159	12.7	0.0	10	−0.087	0.071
52	1823	12.7	0.0	36	−0.027	0.045
53	235	12.7	0.0	9	−0.062	0.066
54	273	12.7	0.0	18	−0.098	0.037

Table 22. Inferrred TRAC means vis à vis HEM/Burnell results

Case	N-data	Burnell	HEM	TRAC inferred
1	31	−0.2680	+0.7610	−0.01
12	10	−0.6470	−0.0526	−0.5
18	92	−0.1176	−0.0288	−0.09
31	15	−0.3728	−0.0394	−0.3
32	71	−0.3950	+0.0739	−0.3
38	28	−1.385	−0.6800	−1.2
39	26	−0.5154	−0.1125	−0.4
40	31	−0.5854	−0.0892	−0.46
43	30	−0.0741	+0.3401	−0.03
50	49	−0.8696	−0.3445	−0.75
52	45	−1.184	−0.6477	−1.0
55	17	−0.1732	+0.0731	−0.1
56	10	−0.9587	−0.2359	−0.77

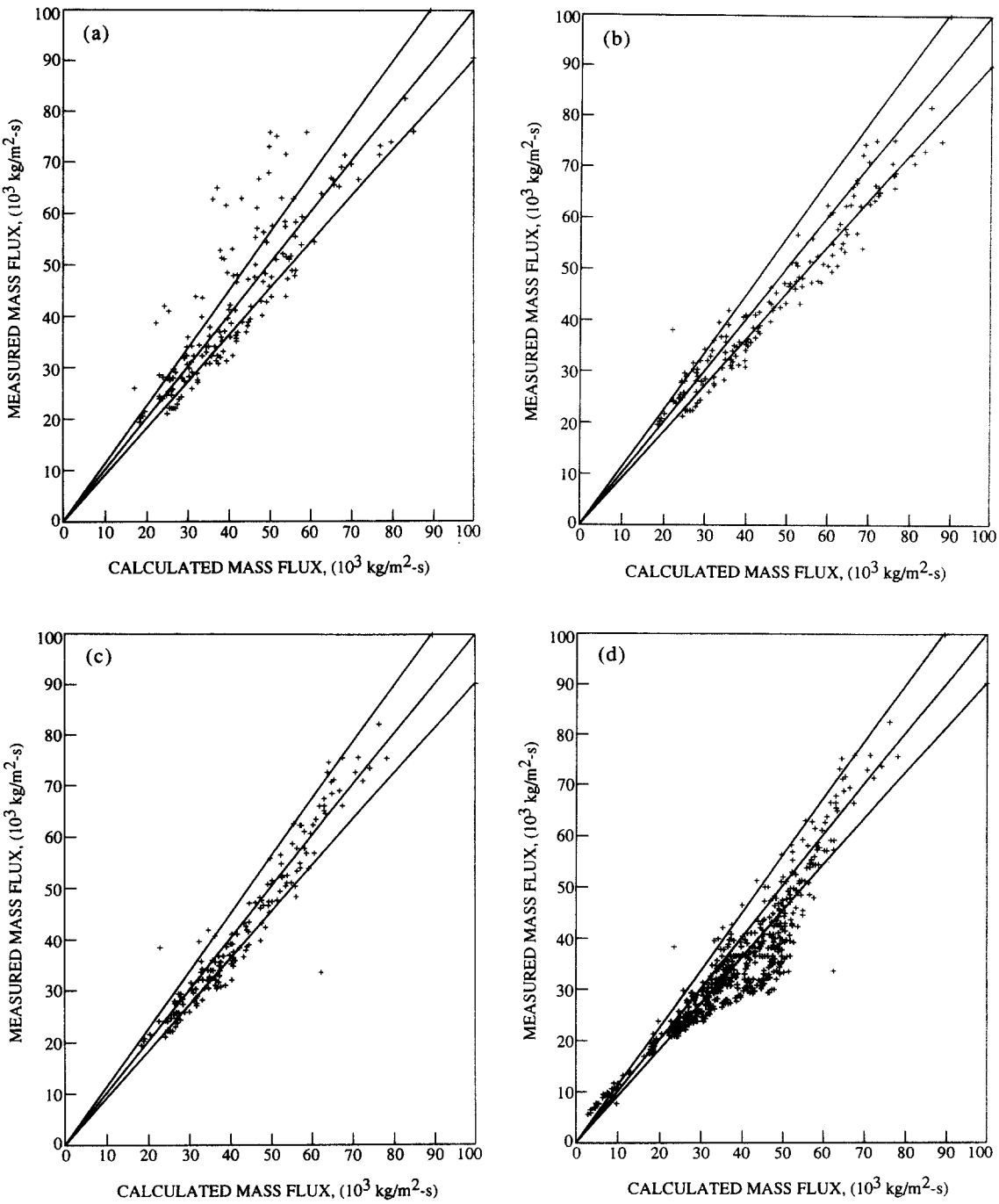

Figure 9. Comparison of space-dependent models with experiments listed in cases 43–54 of table 11 for subcooled inlet conditions: (a) Elias–Chambré model; (b) Richter model; (c) GSL model; and (d) GSL model (all data of table 11).

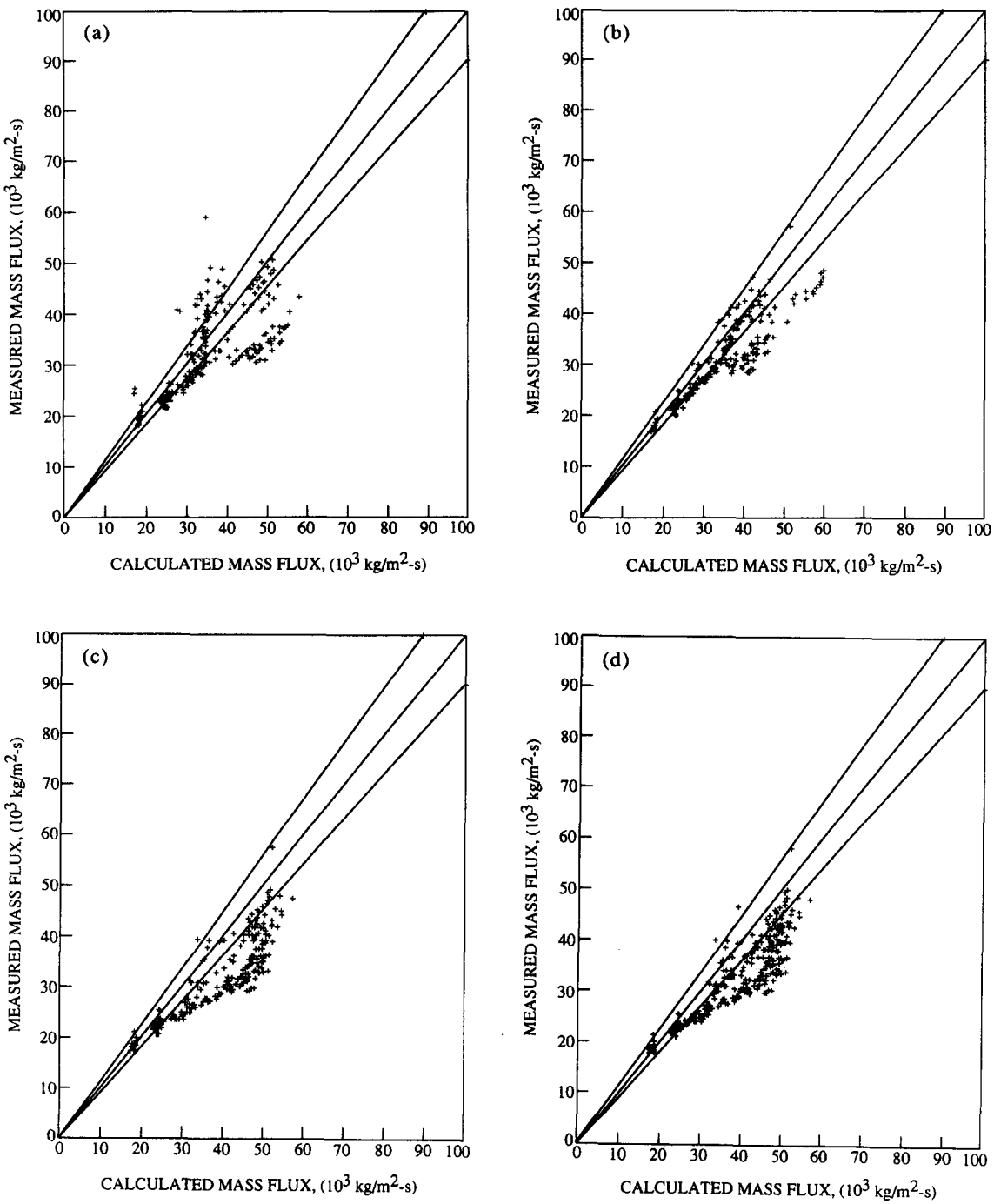

Figure 10. Comparison of space-dependent models with experiments listed in cases 43–54 of table 11 for two-phase inlet conditions: (a) Elias–Chambré model; (b) Richter model; (c) GSL model; and (d) GSL model (all data of table 11).

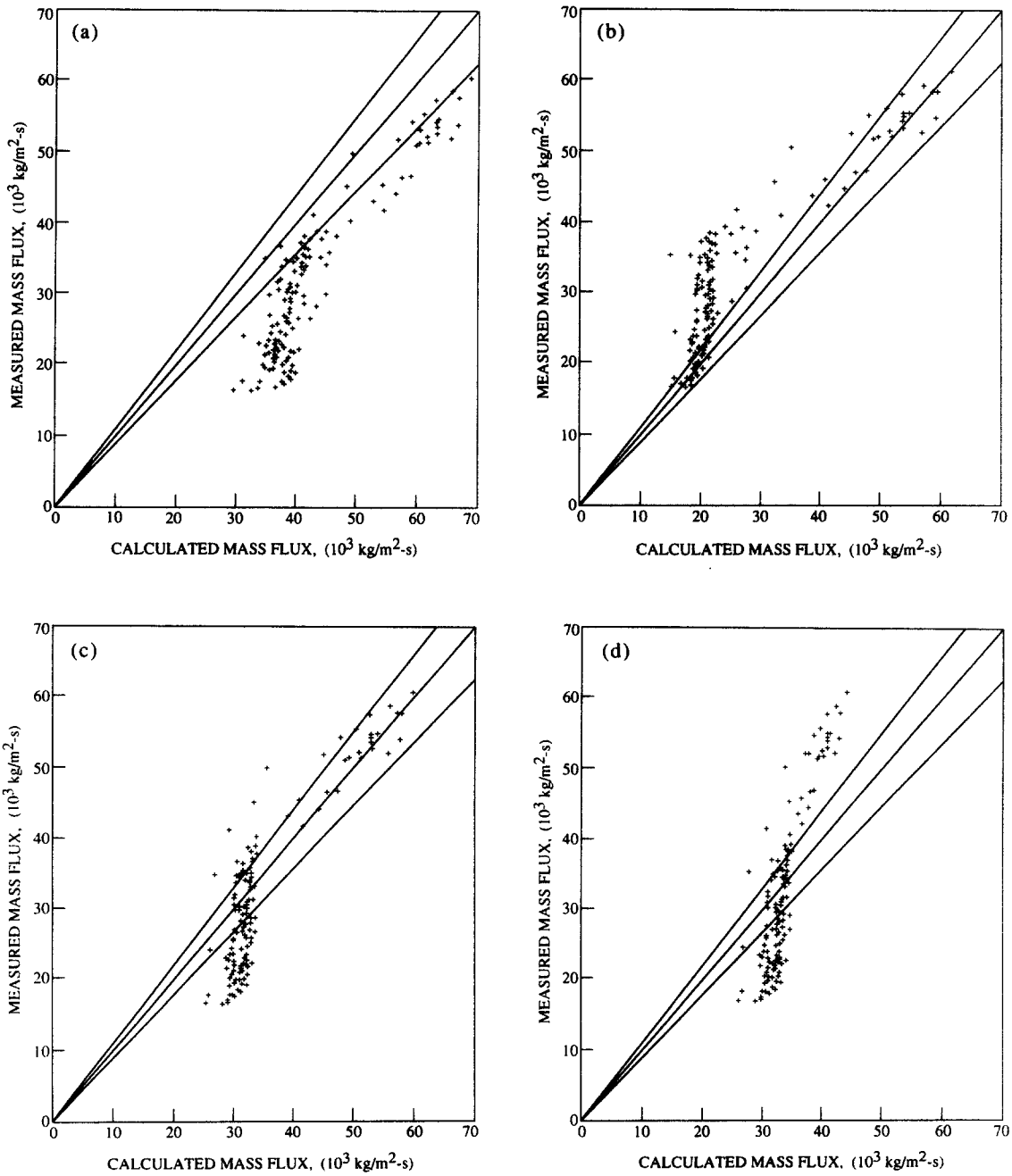

Figure 11 (a)–(d). *Caption opposite.*

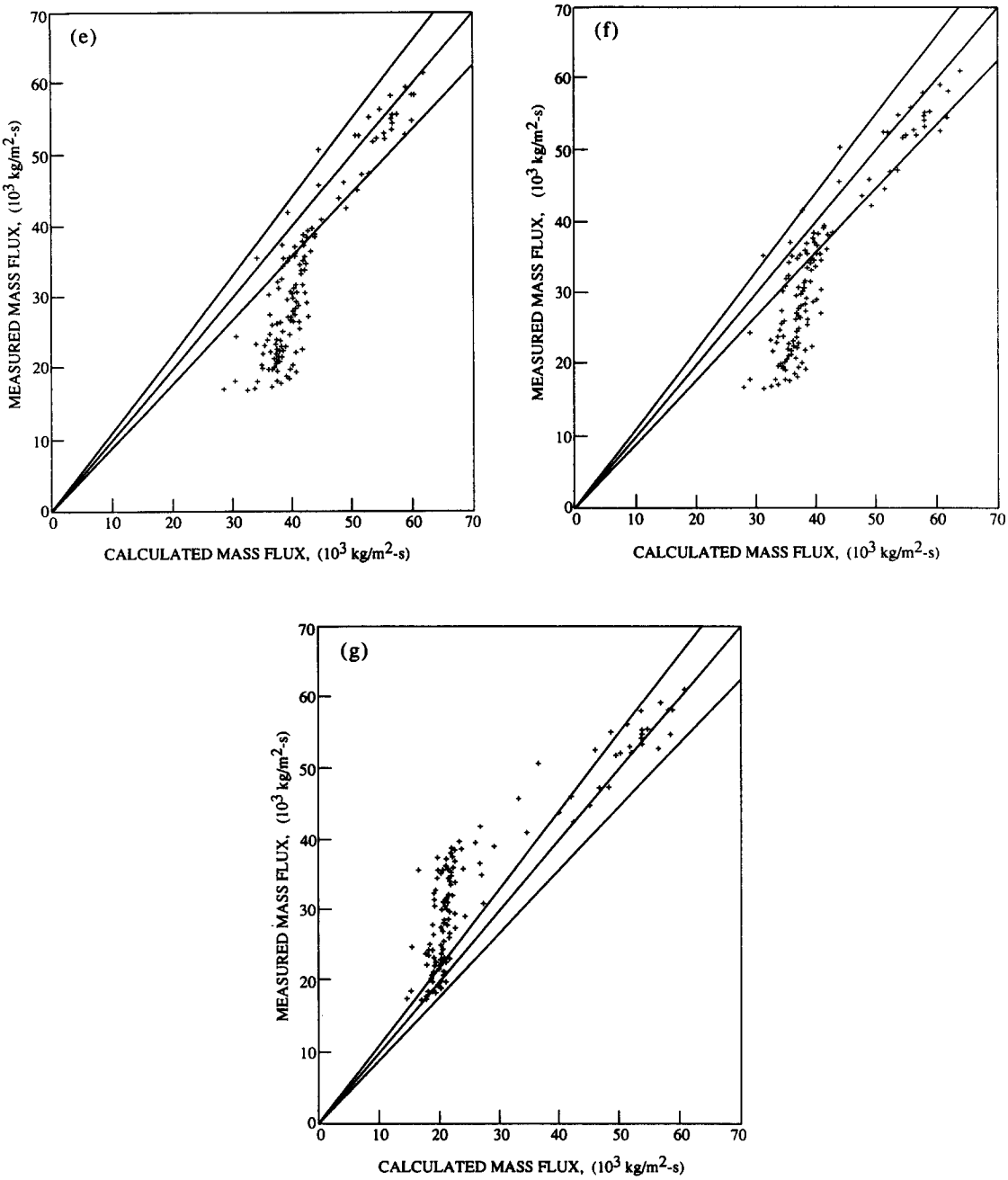

Figure 11 (e)–(g)

Figure 11. Comparison with the Marviken data: (a) Burnell model; (b) isenthalpic model; (c) Moody model with slip; (d) fit to the Moody model; (e) Henry–Fauske model; (f) fit to the Henry–Fauske model; and (g) HEM model.

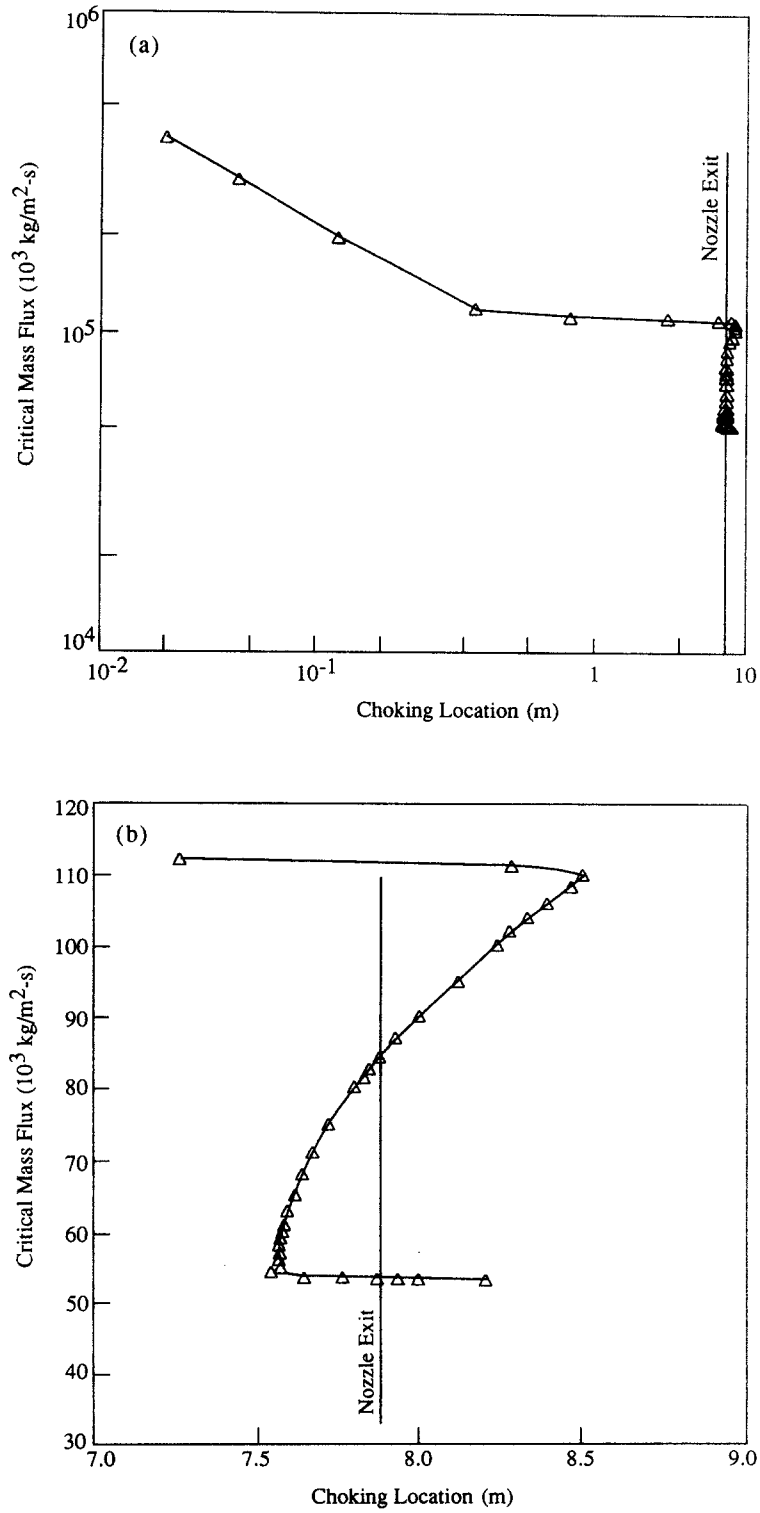

Figure 12. Predicted mass flux vs nozzle length using Richter model for Marviken test 4 at 6 s: (a) choking location; and (b) exit plane.

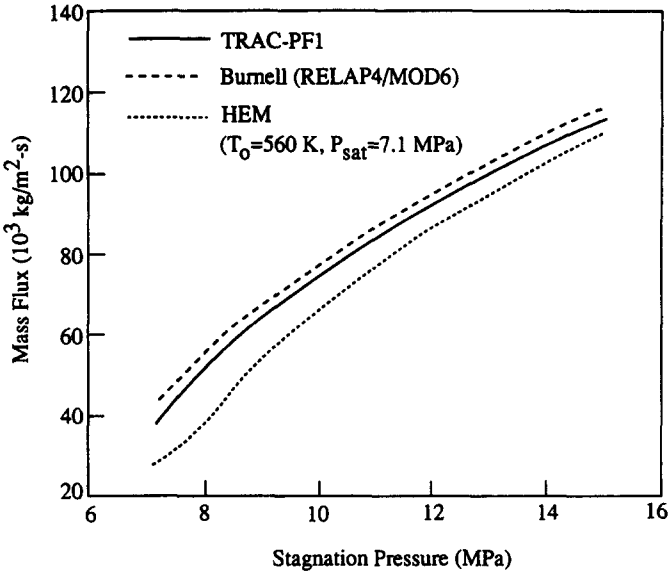

Figure 13. Comparison of subcooled critical mass fluxes using the TRAC–PF1, Burnell and HEM models.

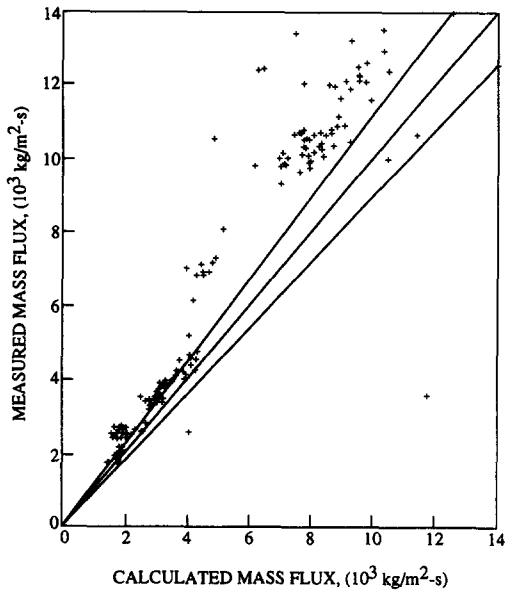

Figure 14. Comparison between the Marviken data and TRACPF1/MOD1 predictions.

Table 23. Predictions of various Marviken tests using TRACPF1/MOD1

Test No.	*N*-data	Mean	SD
12	18	0.142	0.028
13	15	0.113	0.065
15	16	0.029	0.635
16	15	0.218	0.041
17	20	0.133	0.047
18	15	0.135	0.027
19	16	0.120	0.204
20	12	0.313	0.121
21	15	0.288	0.107
22	15	0.260	0.089
25	21	0.242	0.114

Acknowledgement—Partial support to one of the authors (E. Elias) by the Israel Electric Corporation under project number 034-966 is gratefully acknowledged.

REFERENCES

ABDOLLAHIAN, D., HEALZER, J. & JANSSEN, E. 1980 Critical flow data review and analysis. Part I: literature survey. S. Levy Inc., Report SLI-7908-1.

ABDOLLAHIAN, D. *et al.* 1982 Critical flow data review and analysis. EPRI NP 2192.

ALAMGIR, M. D. & LIENHARD, J. H. 1981 Correlation of pressure undershoot during hot water depressurization. *ASME J. Heat Transfer* **103,** 52–73.

ANON 1982 The Marviken full scale critical flow tests. EPRI NP 2370, Vols 1–35.

ANON TRAC-PF1/MOD1: an advanced best estimate computer program for pressurized water reactor thermal-hydraulics. NUREG/CR-3858.

ARDRON, D. H. & ACKERMAN, M. C. 1978 Studies of the critical flow of subcooled water in a pipe. CEGB Report: RD/B/N4299.

ARDRON, K. H. & FURNESS, R. A. 1976 A study of the critical flow models used in reactor blowdown analysis. *Nucl. Engng Design* **39,** 257–266.

ARDRON, K. W. 1978 A two-fluid model for critical vapor-liquid flow. *Int. J. Multiphase Flow* **4,** 3.

BOIVIN, J. Y. 1979 Two-phase critical flow in long nozzles. *Nucl. Technol.* **46,** 540–545.

BOURÉ, J. A. 1977 The critical flow phenomenon with reference to two-phase flow and nuclear reactor systems. *ASME Symp. Thermal Hydraulic Aspects Nuclear Reactor Safety* **1,** 195–216.

BRITTAIN, I. *et al.* 1982 Critical flow modeling in nuclear safety, a state of the art report. NEA-OECD.

BRYERS, R. W., HSIEH, W. W., HUNTER, J. A. & SIEDER, E. N. 1966 Study of two-phase metastable flow. U.S. Department of Interior, Office of Saline Water, R&D Progress Report No. 234, November.

BURNELL, J. A. 1947 Flow of boiling water through nozzles, orifices and pipes. Engineering.

CHEXAL, B. & LELLOUCHE, G. 1986 A full-range drift-flux correlation for vertical flows. Electric Power Research Institute, EPRI NP-3989-SR.

CHEXAL, B., LELLOUCHE, G., HOROWITZ, J. & HEALZER, J. 1989 A full-range drift-flux correlation for generalized applications. NSAC 139, December.

CRUVER, J. E. 1963 Metastable critical flow of steam water mixtures. Ph.D dissertation, Department of Chemical Engineering, University of Washington (available through University Microfilms Inc., Ann Arbor, Mich.).

DANFORTH, J. L. 1941 Flow of hot water through a rounded orifice. M.S. dissertation, Department of Mechanical Engineering, Massachusetts Institute of Technology.

D'AURIA, F. & VIGNI, P. 1980 Two-phase critical flow models. CSNI No. 49.

DEYOUNG, T. L. 1975 Homogeneous equilibrium critical flow model. ANS Internal Report TLD-1-75.

DICKMAN, S., ELIAS, E., KAIZERMAN, S., WACHOLDER, E. & OLEK, S. 1990 A homogeneous non-equilibrium two-phase critical flow model for the analysis of supersonic jet flow. *Trans. 9th International Heat Transfer Conf.*, Jerusalem.

DOBRAN, F. 1987 Non equilibrium modelling of two-phase critical flows in tubes. *ASME J. Heat Transfer* **109,** 731–738.

EDWARDS, A. R. & O'BRIEN, T. P. 1970 Studies of the phenomena connected with the depressurization of water reactors. *J. Br. Nucl. Energy Soc.* **9,** 125–135.

ELIAS, E. & CHAMBRÉ, P. L. 1984 A mechanistic non-equilibrium model for two-phase critical flow. *Int. J. Multiphase Flow* **10,** 1.

FAUSKE, H. K. 1962 Contribution to the theory of two-phase, one component critical flow. Argonne National Laboratory Report ANL-6633.

FINCKE, J. R. & COLLINS, D. R. 1981 The correlation of two-dimension and non-equilibrium effects in subcooled choked nozzle flow. NUREG/CR-1907, EGG-2081.

FORSTER, H. K. & ZUBER, N. 1954 Growth of a vapor bubble in a superheated liquid. *J. Appl. Phys.* **25,** 474–478.

GIOT, M. 1981 Critical flows. In *Thermodynamics of Two-phase Systems for Industrial Design and Nuclear Engineering* (Edited by DELHAYE, J. M., GIOT, M. & RIETHMULLER, M. L.), Chap. 18. McGraw–Hill, New York.

GUIZOVARN, L., PINET, B., BARRIERE, G. & PIETRI, D. 1975 Etude experimentale des debits critiques en ecoulement diphasiques eau vapeur a faible titre dans un canal avec divergent de 7° a des pressions an col de 2 a 7 bars. Department de Transfert et Conversion D'Energie, Service des Transports Thermiques, Note TT No. 501.

HENRY, R. E. 1970 An experimental study of low quality, steam-water critical flow at moderate pressures. Argonne National Laboratory Report ANL-7740.

HENRY, R. E. & FAUSKE, H. F. 1971 The two-phase critical flow of one component mixtures in nozzles, orifices, and short pipes. *ASME J. Heat Transfer.* **93,**

IDEL'CHIK, I. E. 1966 *Handbook of Hydraulic Resistances.* AEC-TR-6630.

ILIC, V. *et al.* 1986 A qualified data base for critical flow of water. EPRI NP 4556.

ISBIN, H. S. 1980 Some observations on the status of two phase critical flow models. *Int. J. Multiphase Flow* **2,** 131–138.

ISBIN, H. S., MOY, J. E. & DUCRUZ, A. J. R. 1957 Two-phase steam water critical flow. *AIChE Jl* **3,** September.

JEANDEY, C., GROS D'AILLON, L., BOURGIN, R. & BARRIERE, G. 1981 Auto vaporisation d'ecoulements eau/vapeur. Departement des Reacteurs a Eau Service des Transferts Thermiques (Centre D'Etudes Nucleaires de Grenoble) Report T. T. No. 163.

JONES, O. C. & SAHA, P. 1977 Non-equilibrium aspects of water reactor safety. BNL-NUREG 23143.

KAIZERMAN, S., WACHOLDER, E. & ELIAS, E. 1983 Characteristics analysis of inhomogeneous, nonequilibrium, two-phase flows using the drift-flux model. *Nucl. Sci. Engng* **84,** 168–173.

KROEGER, P. G. 1978 Application of a non-equilibrium drift flux model to two-phase blowdown experiments. *CSNI Specialists' Meeting on Transient Two-Phase Flow*, Toronto.

LAHEY, R. T. JR. & MOODY, F. J. 1977 The thermal-hydraulics of a boiling water nuclear reactor. ANS Monograph.

LEE, D. H. & SWINNERTON, D. 1983 Evaluation of critical flow for supercritical steam-water. EPRI NP 3086.

LEE, J. F. & SEARS, F. W. 1964 *Thermodynamics.* Addison–Wesley, Reading, Mass.

LEE, SI Y. & SCHROCK, V. E. 1988 Homogeneous non-equilibrium critical flow model for liquid stagnation states. *Trans. ASME Heat Transfer Conf.*

LELLOUCHE, G. S. & ZOLOTAR, A. B. 1982 Mechanistic model for predicting two-phase void fraction for water in vertical tubes, channels, and rod bundles. Electric Power Research Institute, EPRI NP-2246-SR.

MCFADDEN, J. H. *et al.* 1984 RETRAN-02—a program for transient thermal hydraulic analysis of complex fluid flow systems. NP-1850-CCMA, Vol. 1, Rev. 2.

MOODY, F. J. 1965 Maximum flow rate of a single component two-phase mixture. *ASME J. Heat Transfer* 134–142.

MOODY, F. J. 1966 Maximum two-phase vessel blowdown from pipes. *ASME J. Heat Transfer.*

MORRISON, A. F. 1977 Blowdown flow in the BWR BDHT test apparatus. GEAP-21656.

NEUSEN, K. F. 1969 Optimizing of flow parameters for the expansion of very low-quality steam. University of California, Lawrence Radiation Laboratory, UCRL-6152.

OGASAWARA, H. 1969 A theoretical approach to two-phase critical flow (4th Report, experiments on saturated water discharging through long tubes). *Bull. JSME* **12**(52).

OSWATITSCH, K. 1956 *Gas Dynamics.* Academic Press, New York.

RANSOM, V. H. & TRAPP, J. A. 1980 The RELAP5 choked flow model and application to a large scale flow test. *Proc. ANS/ASME/NRC International Topical Meeting on Nuclear Reactor Thermal-Hydraulics*, Saratoga Springs, NUREG/CR-0014, Vol. 2, pp. 799–819.

RANSOM, V. H. *et al.* 1982 *RELAP5/MOD1 Code Manual.* NUREG/CR-1826, EGG-2070.

RANSOM, V. H. & TRAPP, J. A. 1985 *RELAP5/MOD2 Code Manual.* NUREG/CR-4312, EGG-2396.

REOCREUX, M. 1974 Contribution a l'etude des debits critiques en ecoulement diphasique eau-vapeau. Doctural thesis a l'Universite Scientifique et Medicale de Grenoble.

RICHTER, H. J. 1981 Separated two-phase flow model: application to critical flow. EPRI NP-1800.

SCHROCK, V. E., STARKMAN, E. S. & BROWN, R. A. 1977 Flashing flow of initially subcooled water in convergent–divergent nozzles. *J. Heat Transfer* **99**(2).

SEYNHAEVE, J. M. 1980 Etude experimentale des ecoulements diphasiques critiques a faible titre. Doctoral thesis, Department Thermodynamique et Turbomachines, Universite Catholique de Louvain.

SHAPIRO, A. H. 1953 *The Dynamics and Thermodynamics of Compressible Fluid Flow*. The Ronald Press Company, New York.

SOZZI, G. L. & SUTHERLAND, W. A. 1975 Critical flow of saturated and subcooled water at high pressure. NEDO-13418.

TRAPP, J. A. & RANSOM, V. H. 1982 A choked-flow calculation criterion for nonhomogeneous, nonequilibrium, two-phase flows. *Int. J. Multiphase Flow* **8**, 669–681.

WALLIS, G. B. 1980 Critical two-phase flow. *Int. J. Multiphase Flow* **6**, 97–112.

ZALOUDEK, F. R. 1963 The critical flow of hot water through short tubes. HW-77594.

ZUCROW, M. J. & HOFFMAN, J. D. 1976 *Gas Dynamics*. Wiley, New York.